5-2024

El Nino Prediction at 1- and 3- Year Lead Times Driven by the Western North Pacific Precursor and Their Impacts

Krishna Borhara
Utah State University, krishna.borhara@usu.edu

EL NINO PREDICTION AT 1- AND 3- YEAR LEAD TIMES DRIVEN BY THE WESTERN NORTH PACIFIC PRECURSOR AND THEIR IMPACTS

by

Krishna Borhara

A dissertation submitted in partial fulfillment
of the requirements for the degree

of

DOCTOR OF PHILOSOPHY

in

Climate Science

Approved:

Shih-Yu (Simon) Wang, Ph.D. Major Professor	Yoshimitsu Chikamoto, Ph.D. Committee Member
Wei Zhang, Ph.D. Committee Member	Binod Pokharel, Ph.D. Committee Member
Boniface Fosu, Ph.D. Committee Member	D. Richard Cutler, Ph.D. Vice Provost of Graduate Studies

UTAH STATE UNIVERSITY
Logan, Utah

2024

ABSTRACT

El Niño Prediction at 1- and 3- year lead times driven by the western North Pacific precursor and their Impacts

by

Krishna Borhara, Doctor of Philosophy

Utah State University, 2024

Major Professor: Dr. Shih-Yu (Simon) Wang
Department: Plants, Soils and Climate

The El Niño–Southern Oscillation (ENSO) has diverse impacts on weather and climate across the globe through atmospheric teleconnections. Understanding the dynamics that promote the transition to ENSO is critical in producing reliable forecasts and mitigating the adverse impacts of ENSO in various sectors. As climate change progresses, extratropical air–sea interactions become increasingly involved in triggering ENSO development and promote unprecedented changes to its established dynamics, giving rise to new challenges to current prediction efforts and severely altering the impacts of ENSO worldwide. Among these extratropical precursors are sea surface temperature anomalies (SSTAs) in the western North Pacific (WNP) that are linked to ENSO development at 1- and 3- year lead times. Exploring these relationships may provide pathways towards significant advancements in ENSO forecast lead times. The approach applied in this dissertation to decompose each WNP–ENSO relationship has the potential to address questions regarding future changes to ENSO diversity and the amplitude and frequency of ENSO events, as well further understanding of the deterministic mechanisms that promote ENSO at extended lead times.

The first chapter introduces the settings and goals of this research. The second chapter assesses the effects of future warming on the dynamics underlying the 1-year lead WNP–ENSO relationship. The third chapter explores the 3-year lead WNP–ENSO relationship in which warm (cold) SSTAs propagate from the western North Pacific to the central–eastern equatorial Pacific and coincide with El Niño (La Niña) development. This study delves into the mechanisms behind the formation of SSTAs in the western North Pacific, their propagation from the subtropics to tropics in relation to ENSO, and their persistence during propagation. The fourth chapter provides an application of ENSO teleconnection through its role in promoting climate extremes in Tanzania. The fifth chapter concludes and summarizes this dissertation by connecting ENSO prediction efforts to ENSO impacts and provide directions for future studies.

(152 pages)

PUBLIC ABSTRACT

El Niño Prediction at 1- and 3- year lead times driven by the western North Pacific precursor and their Impacts

Krishna Borhara

The El Niño–Southern Oscillation (ENSO) is a climate variability characterized by fluctuations in the atmospheric and upper ocean conditions of the tropical Pacific Ocean that result in either warmer- or colder-than-average sea surface temperatures (SST) in the tropical eastern Pacific. These changes cause variations in weather and climate in distant locations through large-scale atmospheric circulation patterns. These variations often manifest in form of adverse effects or extremes such as heat waves, droughts, or floods, making efforts towards improving ENSO prediction critical in mitigating its impact on various sectors. This dissertation focuses on how interactions between the atmosphere and ocean in the western North Pacific (WNP) can help improve ENSO prediction, as these processes are documented to precede and promote ENSO at two distinct timescales. Chapter 2 examines the effects of future warming on the 1-year lead relationship between WNP and ENSO, including future changes to the amplitude and frequency of ENSO events and the location of the peak SST anomalies of ENSO under the influence of WNP processes 1 year prior. Chapter 3 aims to discern the fundamental dynamics underlying the 3-year lead relationship between SST anomalies that form in the western North Pacific and the processes that drive their shift towards the central–eastern equatorial Pacific prior to ENSO. Chapter 4 concludes this dissertation by providing an application of ENSO teleconnection through its role in promoting climate extremes in Tanzania.

CONTENTS

Page

LIST OF TABLES

LIST OF FIGURES

CHAPTER 1

INTRODUCTION

The El Niño Southern Oscillation (ENSO) is a climate oscillation in the tropical Pacific that affects weather and climate across the globe through atmospheric teleconnection (e.g., Yeh et al. 2018a; Taschetto et al. 2020). Most of the teleconnection patterns promote extreme events that have adverse effects in many interconnected sectors including agriculture (Cao et al. 2023), land use (Vilanova et al. 2021) and economy (Callahan and Mankin 2023), making efforts towards improving ENSO prediction critical in mitigating these impacts. The understanding of ENSO and its prediction has been significantly improved over the years. The Bjerknes Positive Feedback played a crucial role in ENSO prediction by providing a robust physical basis for discerning the mechanisms that drive the development and evolution of ENSO events (Bjerknes 1966, 1969) while the derivations of various negative feedback modes helped explain the oscillatory nature of ENSO (Suarez and Schopf 1988; Graham and White 1988; Battisti and Hirst 1989; Jin 1997a, b; Picaut et al. 1996, 1997; Weisberg and Wang 1997; Wang et al. 1999). Cane et al. (1986) pioneered the introduction of the initial coupled climate model, which enabled a comprehensive assessment of the collective impacts of both the atmosphere and the ocean on the climate system. This groundbreaking approach marked a significant step forward and resulted in the first instance of successfully predicting an El Niño event – specifically, the 1986 occurrence.

Initially, studies that focused on improving ENSO prediction used tropical dynamics to explain ENSO, largely due to the prevailing notion that ENSO was primarily a tropical phenomenon (e.g., Zebiak 1989; McPhaden et al. 1992). However, as model prediction skill declined after 2000, it became evident that the point of reduced predictability lay in the spring period preceding an ENSO event (Webster and Yang 1992; Webster 1995; Torrence and Webster 1998; McPhaden 2004; Luo et al. 2008; Yu et al. 2009; Duan et al. 2009; Duan and Wei 2012). In

addition, ENSO patterns in the 21st century have diversified in amplitude (Trenberth and Hoar 1996; Zhang et al. 2008; Vecchi and Wittenberg 2010), frequency (Trenberth and Hoar 1996; An and Wang 2000; Fedorov and Philander 2000; Kao and Yu 2009), spatial structure (McPhaden 2004; Kao and Yu 2009; Yeh et al. 2009; Timmerman et al. 2018), temporal evolution (McPhaden 1999; Timmerman et al. 2018), and teleconnection (Ashok et al. 2007; Kao and Yu 2009; Wang et al. 2012; Yu et al. 2015; Fosu et al. 2020). Peak SSTAs associated with El Niños and La Niñas prior to the 21s century were in the eastern Pacific but have now shifted to the central Pacific and western Pacific (Yu and Kao 2007; Kao and Yu 2009; Wang et al. 2019), adding more complexities to address in prediction models (Yu and Kim 2010; Ham and Kug 2012). The existence of the spring predictability barrier and the westward migration of peak ENSO sea surface temperature anomalies (SSTAs) are attributed, at least in part, to the increasing influence of extratropical precursors in the North Pacific.

The five major extratropical precursors proposed to date are the Seasonal Footprinting Mechanism (SFM; Vimont et al. 2003a; Alexander et al. 2010), Pacific Meridional Mode (PMM; Zhang et al. 2009; Larson and Birtman 2013, 2014; Stuecker 2018), Trade Wind Charging (TWC; Anderson et al. 2013; Chakravorty et al. 2020; Pivotti et al. 2023), Victoria Mode (VM; Bond et al. 2003; Ding et al. 2015; Shi et al. 2022) and opposite-signed sea surface temperature (SST) variability in western North Pacific (WNP; Wang et al. 2012, 2013; Fosu et al. 2020). These precursors develop either during or prior to the spring prior to an ENSO and incorporating them in prediction models increase the forecast skill (Boschat et al. 2013; Chen et al. 2020; Shi and Ding 2020; Zhao et al. 2022). While these precursors have played a role in ENSO development over time, their impact has escalated in the past decade, mainly due to the influence of climate change (e.g., Wang et al. 2013). The first four precursors initiate ENSO events by linking it to the North Pacific Oscillation (NPO; Walker and Bliss 1932; Rogers 1981; Wang et al. 2007; Linkin and Nigam 2008) but air–sea interactions in the western North Pacific in the boreal winter are reported to directly induce Kelvin waves in the equatorial Pacific by the following summer and hence more

likely to trigger an El Niño the next winter compared to other precursors (Wang et al. 2012), a relationship that is strengthening under the greenhouse effect (Wang et al. 2013). This 1-year lead WNP–ENSO relationship is opposite-signed, for which the cold (warm) WNP phase precedes the warm (cold) ENSO phase. However, Wang et al. (2015) also observed that a same-signed variability relation exists between the two phases, where a warm (cold) WNP phase precedes a warm (cold) ENSO phase 3 years later. This link is established through prolonged propagation of the SSTA from the western North Pacific to the central–eastern equatorial Pacific. The identification of two distinct connections between the WNP mode and ENSO implies that air–sea dynamics in the western North Pacific are strongly tied to ENSO. These findings merit further studies aimed at understanding the dynamics that establish a robust linkage between the two modes of climate variability and assessing the impact of future warming on this relationship.

In the second chapter of this dissertation, we study the effects of future warming on the 1-year lead relationship between WNP and ENSO. We use a conditional probability approach on historical and Shared Socioeconomic Pathway 3–7.0 (SSP370) runs of both Coupled Model Intercomparison Project Phase 6 (CMIP6; Eyring et al. 2016) and Community Earth System Model Version 2 Large Ensembles (CESM2-LE; Danabasoglu et al. 2020; Rodgers et al. 2021) datasets to focus on cold WNP events that are followed by El Niños 1 year later. In the third chapter of the dissertation, we decompose the dynamics underlying the 3-year lead WNP–ENSO relationship using observation and model data. We employ a wide range of atmospheric, ocean surface and subsurface variables to obtain a three-dimensional perspective of the mechanisms involved in the formation, propagation, and persistence of the SSTAs from the subtropics to tropics. We use SST heat budget analyses to connect the propagation of the SSTA to the recharge and discharge of tropical Pacific Ocean heat oscillating at interannual timescales characteristic of ENSO.

The interconnectedness of global climate systems manifests in myriad ways, with phenomena such as ENSO influencing weather patterns across the world. This global reach of climatic interactions allows local weather phenomena, such as rainfall variability in East Africa, to

be influenced by broader climatic drivers. In essence, the fluctuations in SSTs in the Pacific Ocean may resonate in the rainfall patterns of Tanzania, revealing the profound complexity and interconnected nature of our climate. This dissertation embarks on a dual exploration, delving into the behavior of ENSO in the context of climate change and its distant yet significant effects on precipitation patterns in Tanzania.

The second chapter unravels the increasingly complex interactions between extratropical air-sea interactions and ENSO. By examining the western North Pacific (WNP) phase and its effects on El Niño development, we explore intricate relationships, feedback mechanisms, and influences of enhanced global warming on these vital oceanic phenomena. The findings suggest a future where El Niño events could become stronger and more frequent, driven by changes in the WNP. Teleconnections from the tropical Pacific are reported to extend towards climate in Tanzania (Ogallo 1988; Nicholson and Kim 1997; Reason et al. 2000). Furthermore, droughts have become more frequent, longer, and more severe in the last two decades, particularly the 2010–2011 East African drought when famine led to a humanitarian crisis. However, in recent years, East African countries have been plagued by frequent floods and the observed drying trend also contradicts the projected increase in East African rainfall by climate models (Shongwe et al. 2011; Williams and Funk 2011; Rowell et al. 2015). The lack of consensus between past and future precipitation trends calls for re-examination of Tanzania's precipitation patterns.

Our examination of historical and projected precipitation for Tanzania in the fourth chapter offers a window into the localized impacts of global climate phenomena. Analyzing trends from 1961 to 2016, we uncover correlations between sea surface temperatures in the Indian Ocean and rainfall variability in Tanzania, juxtaposing these relationships against the broader backdrop of ENSO. Together, these investigations form a cohesive narrative that connects the broad-scale dynamics of ENSO with localized climatic effects in East Africa. The synthesis of global climate phenomena with region-specific weather patterns demonstrates the multifaceted nature of climate science, underscoring the importance of both macroscopic and microscopic perspectives in

understanding our changing climate. These inquiries contribute to a more nuanced understanding of climatic interactions, with implications for climate prediction, policy-making, and adaptation strategies. As we navigate the challenges and opportunities of a warming world, this dissertation offers insights that transcend geographical boundaries, revealing the delicate balance and profound interconnectivity of Earth's climate systems.

REFERENCES

Alexander, M. A., D. J. Vimont, P. Chang, and J. D. Scott, 2010: The impact of extratropical atmospheric variability on ENSO: Testing the seasonal footprinting mechanism using coupled model experiments. *J. Climate*, **23**, 2885–2901, https://doi.org/10.1175/2010JCLI3205.1

An, S.-I., and B. Wang, 2000: Interdecadal change of the structure of the ENSO mode and its impact on the ENSO frequency. *J. Climate*, **13**, 2044–2055. https://doi.org/10.1175/1520-0442(2000)013<2044:ICOTSO>2.0.CO;2

Anderson, B. T., R. C. Perez, and A. Karspeck, 2013: Triggering of El Niño onset through trade wind–induced charging of the equatorial Pacific. *Geophys. Res. Lett.*, **40**, 1212–1216, https://doi.org/10.1002/grl.50200

Ashok, K., S. K. Behera, S. A. Rao, H. Weng, and T. Yamagata, 2007: El Niño Modoki and its possible teleconnections. *J. Geophys. Res.*, **112**, C11007, https://doi.org/10.1029/2006JC003798

Battisti, D. S., and A. C. Hirst, 1989: Interannual Variability in a Tropical Atmosphere–Ocean Model: Influence of the Basic State, Ocean Geometry and Nonlinearity. *J. Atmos. Sci.*, **46**, 1687–1712, https://doi.org/10.1175/1520-0469(1989)046<1687:IVIATA>2.0.CO;2

Bjerknes, J., 1966: A possible response of the atmospheric Hadley circulation to equatorial anomalies of ocean temperature. *Tellus*, **18**, 820–829, https://doi.org/10.1111/j.2153-3490.1966.tb00303.x

Bjerknes, J., 1969: Atmospheric teleconnections from the equatorial Pacific. *Mon. Wea. Rev.*, **97**, 163–172, https://doi.org/10.1175/1520-0493(1969)097%3c0163:atftep%3e2.3.co;2

Bond, N. A., J. E. Overland, M. Spillane, and P. Stabeno, 2003: Recent shifts in the state of the North Pacific. *Geophys. Res. Lett.*, **30**, 2183, https://doi.org/10.1029/2003GL018597

Boschat, G., P. Terray, and S. Masson, 2013: Extratropical forcing of ENSO. *Geophys. Res. Lett.*, **40**, 1605–1611, https://doi.org/10.1002/grl.50229

Callahan, C. W., and J. S. Mankin, 2023: Persistent effect of El Niño on global economic growth. *Sci*., **380**, 1064–1069. https://doi.org/10.1126/science.adf2983

Cane, M. A., S. E. Zebiak, and S. C. Dolan, 1986: Experimental forecasts of El Niño. *Nat.*, **321**, 827–832, https://doi.org/10.1038/321827a0

Cao, J., Z. Zhang, F. Tao, Y. Chen, X. Luo, and J. Xie, 2023: Forecasting global crop yields based on El Nino Southern Oscillation early signals. *Agricultural Systems*, **205**, 103564, https://doi.org/10.1016/j.agsy.2022.103564

Chakravorty, S., R. C. Perez, B. T. Anderson, B. S. Giese, S. M. Larson, and V. Pivotti, 2020: Testing the Trade Wind Charging Mechanism and Its Influence on ENSO Variability. *J. Climate*, **33**, 7391–7411, https://doi.org/10.1175/JCLI-D-19-0727.1

Chen, D., M. Cane, A. Kaplan, S. E. Zebiak, and D. Huang, 2004: Predictability of El Niño over the past 148 years. *Nat.*, **428**, 733–736, https://doi.org/10.1038/nature02439

Ding, R., J. Li, Y.-H. Tseng, C. Sun, and Y. Guo, 2015: The Victoria mode in the North Pacific linking extratropical sea level pressure variations to ENSO. *J. Geophys. Res. Atmos.*, **120**, 27–45, https://doi.org/10.1002/2014jd022221

Duan, W., and C. Wei, 2012: The 'spring predictability barrier' for ENSO predictions and its possible mechanism: Results from a fully coupled model. *Int. J. Climatol.*, **33**, 1280–1292, https://doi.org/10.1002/joc.3513

Duan, W., X. Liu, K. Zhu, and M. Mu, 2009: Exploring the initial errors that cause a significant "spring predictability barrier" for El Niño events. *J. Geophys. Res.*, **114**, C04022, https://doi.org/10.1029/2008JC004925

Fedorov, A. V., and S. G. Philander, 2000: Is El Niño changing?. *Sci.*, **288**, 1997–2002. https://doi.org/10.1126/science.288.5473.1997

Fosu, B., J. He, and S.-Y. Wang, 2020: The influence of wintertime SST variability in the Western North Pacific on ENSO diversity. *Climate Dyn.*, **54**, 3641–3654, https://doi.org/10.1007/s00382-020-05193-7

Graham, N. E., and W. B. White, 1988: The El Niño cycle: A natural oscillator of the Pacific Ocean-atmosphere system. *Sci.*, **240**, 1293–1302, https://doi.org/10.1126/science.240.4857.1293

Ham, Y.-G., and J.-S. Kug, 2012: How well do current climate models simulate two types of El Niño? *Climate Dyn.*, **39**, 383–398, https://doi.org/10.1007/s00382-011-1157-3

Jin, F.-F., 1997a: An equatorial ocean recharge paradigm for ENSO. Part I: Conceptual model. *J. Atmos. Sci.*, **54**, 811–829, https://doi.org/10.1175/1520-0469(1997)054<0811:AEORPF>2.0.CO;2

Jin, F.-F., 1997b: An equatorial ocean recharge paradigm for ENSO. Part II: A stripped-down coupled model. *J. Atmos. Sci.*, **54**, 830–847, https://doi.org/10.1175/1520-0469(1997)054<0830:AEORPF>2.0.CO;2

Kao, H.-Y., and J.-Y. Yu, 2009: Contrasting eastern-Pacific and central-Pacific types of ENSO. *J. Climate*, **22**, 615–632, https://doi.org/10.1175/2008JCLI2309.1

Larson, S. M., and B. P. Kirtman, 2013: The Pacific Meridional Mode as a trigger for ENSO in a high-resolution coupled model. *Geophys. Res. Lett.*, **40**, 3189–3194, https://doi.org/10.1002/grl.50571

Larson, S. M., and B. P. Kirtman, 2014: The Pacific meridional mode as an ENSO precursor and predictor in the North American multimodel ensemble. *J. Climate*, **27**, 7018–7032, https://doi.org/10.1175/JCLI-D-14-00055.1

Linkin, M. E., and S. Nigam, 2008: The North Pacific Oscillation–west Pacific teleconnection pattern: Mature-phase structure and winter impacts. *J. Climate*, **21**, 1979–1997, https://doi.org/10.1175/2007JCLI2048.1

Luo, J.-J., S. Masson, S. K. Behera, and T. Yamagata, 2008: Extended ENSO predictions using a fully coupled ocean-atmosphere model. *J. Climate*, 21, 84–93, https://doi.org/10.1175/2007JCLI1412.1

Lyon, B., 2014: Seasonal drought in the Greater Horn of Africa and its recent increase during the March-May long rains. *J. Climate*, ***27***, 7953–7975, https://doi.org/10.1175/JCLI-D-13-00459.1

McPhaden, M. J., 1999: Genesis and evolution of the 1997–98 El Niño. *Sci.*, **283**, 950–954, https://doi.org/10.1126/science.283.5404.950

McPhaden, M. J., 2004: Evolution of the 2002/03 El Niño. *Bull. Amer. Meteor. Soc.*, **85**, 677–696, https://doi.org/10.1175/BAMS-85-5-677

McPhaden, M. J., F. Bahr, Y. Du Penhoat, E. Firing, S. P. Hayes, P. P. Niiler, P. L. Richardson, and J. M. Toole, 1992: The response of the western equatorial Pacific Ocean to westerly wind bursts during November 1989 to January 1990. *J. Geophys. Res.*, **97**, 14289–14303, https://doi.org/10.1029/92JC01197

Nicholson, S.E., and J. Kim, 1997: The relationship of the El Niño–Southern Oscillation to African rainfall. *Int. J. Climatol.*, **17**, 117–135, https://doi.org/10.1002/(SICI)1097-0088(199702)17:2<117::AID-JOC84>3.0.CO;2-O

Ogallo, L.J., 1988: Relationships between seasonal rainfall in East Africa and the Southern Oscillation. *J. Climatol.*, **8**, 31–43, https://doi.org/10.1002/joc.3370080104

Picaut, J., F. Masia, and Y. Du Penhoat, 1997: An advective-reflective conceptual model for the oscillatory nature of the ENSO. *Sci.*, **277**, 663–666, https://doi.org/10.1126/science.277.5326.663

Picaut, J., M. Ioualalen, C. Menkes, T. Delcroix, and M. J. McPhaden, 1996: Mechanism of the zonal displacements of the Pacific warm pool: Implications for ENSO. *Sci.*, **274**, 1486–1489, https://doi.org/10.1126/science.274.5292.1486

Pivotti, V., B. T. Anderson, A. Cherchi, and A. Bellucci, 2023: North Pacific trade wind precursors to ENSO in the CMIP6 HighResMIP multimodel ensemble. *Climate Dyn.*, **60**, 2501–2516, https://doi.org/10.1007/s00382-022-06449-0

Reason, C. J. C., R. J. Allan, J. A. Lindesay, and T. J. Ansell, 2000: ENSO and climatic signals across the Indian Ocean basin in the global context: Part I. Interannual composite patterns. *Int. J. Climatol.*, **20**, 1285–1327, https://doi.org/10.1002/1097-0088(200009)20:11<1285::AID-JOC536>3.0.CO;2-R

Rogers, J. C., 1981: The North Pacific Oscillation. *J. Climatol.*, **1**, 39–57, https://doi.org/10.1002/joc.3370010106

Rowell, D.P., B. B. Booth, S. E. Nicholson, and P. Good, 2015: Reconciling Past and Future Rainfall Trends over East Africa. *J. Clim*ate, **28**, 9768–9788, https://doi.org/10.1175/JCLI-D-15-0140.1

Shi, L., and R. Ding, 2020: Contributions of tropical–extratropical oceans to the prediction skill of ENSO after 2000. *Atmos. Oceanic Sci. Lett.*, **13**, 338–345, https://doi.org/10.1080/16742834.2020.1755600

Shi, L., R. Ding, S. Hu, J. Li, Y. Tseng, and X. Li, 2022: Influence of the North Pacific Victoria mode on the spring persistence barrier of ENSO. *J. Geophys. Res. Atmos.*, **127**, e2021JD036206, https://doi.org/10.1029/2021JD036206

Shongwe, M. E., G. J. van Oldenborgh, and B. van den Hurk, 2011: Projected changes in mean and extreme precipitation in Africa under global warming. Part II: East Africa. *J. Climate*, **24**, 3718–3733, https://doi.org/10.1175/2010JCLI2883.1

Stuecker, M. F., 2018: Revisiting the Pacific Meridional Mode. *Sci. Rep.*, **8**, 3216, https://doi.org/10.1038/s41598-018-21537-0

Suarez, M. J., and P. S. Schopf, 1988: A Delayed Action Oscillator for ENSO. *J. Atmos. Sci.*, **45**, 3283–3287, https://doi.org/10.1175/1520-0469(1988)045<3283:ADAOFE>2.0.CO;2

Taschetto**,** A. S., C. C. Ummenhofer, M. F. Stuecker, D. Dommenget, K. Ashok, R. R. Rodrigues, and S.-W. Yeh, 2020: ENSO Atmospheric Teleconnections. *El Niño Southern Oscillation in a Changing Climate, Geophys. Monogr. Ser.*, No. 253, Amer. Geophys. Union, 309–335, https://doi.org/10.1002/9781119548164.ch14

Timmermann, A., and Coauthors, 2018: El Niño–Southern Oscillation complexity. *Nat*., **559**, 535–545. https://doi.org/10.1038/s41586-018-0252-6

Torrence, C., and P. J. Webster, 1998: The annual cycle of persistence in the El Niño/Southern Oscillation. *Quart. J. Roy. Meteor. Soc.*, **124**, 1985–2004, https://doi.org/10.1002/qj.49712455010

Trenberth, K. E., and T. J. Hoar, 1996: The 1990–1995 El Niño–Southern Oscillation event: Longest on record. *Geophys. Res. Lett*., **23**, 57–60. https://doi.org/10.1029/95GL03602

Vecchi, G. A., and A. T. Wittenberg, 2010: El Niño and our future climate: where do we stand?. *WIREs Climate Change*, **1**, 260–270. https://doi.org/10.1002/wcc.33

Vilanova, R. A., and Coauthors, 2021: Vegetation degradation in ENSO events: Drought assessment, soil use and vegetation evapotranspiration in the Western Brazilian Amazon. *Remote Sensing Applications: Society and Environment.,* **23**, 100531, https://doi.org/10.1016/j.rsase.2021.100531

Vimont, D. J., J. M. Wallace, and D. S. Battisti, 2003a: The seasonal footprinting mechanism in the Pacific: Implications for ENSO. *J. Climate*, **16**, 2668–2675, https://doi.org/10.1175/1520-0442(2003)016<2668:TSFMIT>2.0.CO;2

Walker, G. T., and E. W. Bliss, 1932: World Weather V. *Mem. Roy. Meteor. Soc*., **4**, 53–84, https://www.rmets.org/sites/default/files/papers/ww5.pdf

Wang, B., X. Luo, Y.-M. Yang, W. Sun, M. A. Cane, W. Cai, S.-W. Yeh, and J. Liu, 2019: Historical change of El Niño properties sheds light on future changes of extreme El Niño.

Proc. Natl. Acad. Sci. U. S. A., **116**, 22512–22517, https://doi.org/10.1073/pnas.1911130116

Wang, C., R. H. Weisberg, and J. I. Virmani, 1999: Western Pacific interannual variability associated with the El Niño-Southern Oscillation. *J. Geophys. Res.*, **104**, 5131–5149, https://doi.org/10.1029/1998JC900090

Wang, L., W. Chen, and R. Huang, 2007: Changes in the variability of North Pacific Oscillation around 1975/1976 and its relationship with East Asian winter climate. *J. Geophys. Res.*, **112**, D11110, https://doi.org/10.1029/2006JD008054

Wang, S.-Y., M. L'Heureux, and H.-H. Chia, 2012: ENSO prediction one year in advance using western North Pacific sea surface temperatures. *Geophys. Res. Lett.*, **39**, L05702, https://doi.org/10.1029/2012GL050909

Wang, S.-Y., M. L'Heureux, and J.-H. Yoon, 2013: Are greenhouse gases changing ENSO precursors in the western North Pacific?. *J. Climate*, **26**, 6309–6322, https://doi.org/10.1175/JCLI-D-12-00360.1

Wang, S.-Y., X. Jiang, and B. Fosu, 2015: Global eastward propagation signals associated with the 4–5-year ENSO cycle. *Climate Dyn.*, **44**, 2825–2837, https://doi.org/10.1007/s00382-014-2422-z

Webster, P. J., 1995: The annual cycle and the predictability of the tropical coupled ocean-atmosphere system. *Meteor. Atmos. Phys.*, **56**, 33–55, https://doi.org/10.1007/BF01022520

Webster, P. J., and S. Yang, 1992: Monsoon and ENSO: Selectively interactive systems. *Quart. J. Roy. Meteor. Soc.*, **118**, 877–926, https://doi.org/10.1002/qj.49711850705

Weisberg, R. H., and C. Wang, 1997: A western Pacific oscillator paradigm for the El Niño-Southern Oscillation. *Geophys. Res. Lett.*, **24**, 779–782, https://doi.org/10.1029/97GL00689

Williams, A. P., and C. Funk, 2011: A westward extension of the warm pool leads to a westward extension of the Walker circulation, drying eastern Africa. *Climate Dyn.*, **37**, 2417–2435, https://doi.org/10.1007/s00382-010-0984-y

Yeh, S.-W., and Coauthors, 2018a: ENSO atmospheric teleconnections and their response to greenhouse gas forcing. *Rev. Geophys.*, **56**, 185–206, https://doi.org/10.1002/2017RG000568

Yeh, S.-W., J.-S. Kug, B. Dewitte, M.-H. Kwon, B. P. Kirtman, and F.-F, Jin, 2009. El Niño in a changing climate. *Nat.*, **461**, 511–514, https://doi.org/10.1038/nature08316

Yu, J.-Y., and H.-Y. Kao, 2007: Decadal changes of ENSO persistence barrier in SST and ocean heat content indices: 1958–2001. *J. Geophys. Res.*, 112, D13106, https://doi.org/10.1029/2006JD007654

Yu, J.-Y., and S. T. Kim, 2010: Identification of central-Pacific and eastern-Pacific types of ENSO in CMIP3 models. *Geophys. Res. Lett.*, **37**, L15705, https://doi.org/10.1029/2010GL044082

Yu, J.-Y., P. Kao, H. Paek, H.-H. Hsu, C. Hung, M.-M. Lu, and S.-I. An, 2015: Linking emergence of the central Pacific El Niño to the Atlantic multidecadal oscillation. *J. Climate*, **28**, 651–662. https://doi.org/10.1175/JCLI-D-14-00347.1

Yu, Y., W, Duan, H. Xu, and M. Mu, 2009: Dynamics of nonlinear error growth and season-dependent predictability of El Niño events in the Zebiak–Cane model. *Quart. J. Roy. Meteor. Soc.*, **135**, 2146–2160, https://doi.org/10.1002/qj.526

Zebiak, S. E., 1989: On the 30–60 Day Oscillation and the Prediction of El Niño. *J. Climate*, **2**, 1381–1387, http://www.jstor.org/stable/26196384

Zhang, L., P. Chang, and L. Ji, 2009: Linking the Pacific Meridional Mode to ENSO: Coupled Model Analysis. *J. Climate*, **22**, 3488–3505, https://doi.org/10.1175/2008JCLI2473.1

Zhang, Q., Y. Guan, and H. Yang, 2008: ENSO amplitude change in observation and coupled models. *Adv. Atmos. Sci.*, **25**, 361–366. https://doi.org/10.1007/s00376-008-0361-5

Zhao, Y., Y. Jin, J. Li, and A. Capotondi, 2022: The role of extratropical Pacific in crossing ENSO spring predictability barrier. *Geophys. Res. Lett*., **49**, e2022GL099488, https://doi.org/10.1029/2022GL099488

CHAPTER 2

THE ROLE OF THE WESTERN NORTH PACIFIC PRECURSOR (WNP) AS AN EL NINO–SOUTHERN OSCILLATION (ENSO) PRECURSOR IN A WARMER FUTURE CLIMATE

2.1 Abstract

Extratropical air–sea interactions have become increasingly involved in promoting the transition to the El Niño–Southern Oscillation (ENSO) with climate change. In this study, we break down the effects of future warming on the 1-year lead relationship between a cold western North Pacific (WNP) phase and El Niño development the following winter. We apply a conditional probability approach and sea surface temperature (SST) budget analysis on historical and Shared Socioeconomic Pathway 3–7.0 (SSP370) model runs. With enhanced warming, cold WNP SST anomalies in the boreal winter further strengthen summer westerly anomalies in the western equatorial Pacific, which promote the intensification of surface convergence and anomalous Ekman and geostrophic advection, and positive SST anomalies in the central equatorial Pacific in the seasons prior to the El Niño. Downwelling equatorial Kelvin waves induced by the westerly wind stress facilitate entrainment of subsurface water into the mixed layer during the transition period to trigger stronger thermocline feedback in the central–eastern equatorial Pacific. As a result, the amplitude and frequency of El Niño and its tropical precursors are projected to increase with warming under the WNP influence. ENSO diversity modulated by this relationship depends on the relative strength of advective and thermocline feedbacks, as well as the background state at the time of the event. The intensification of positive Pacific Meridional Mode (PMM) southwesterlies during the WNP–ENSO transition suggests a strengthened three-way link between WNP, PMM and ENSO under enhanced warming that may promote stronger and/or more frequent El Niños.

2.2 Introduction

The El Niño–Southern Oscillation (ENSO) is the most dominant mode of interannual climate variability. Many efforts have been made to improve ENSO prediction over the past several decades. The Bjerknes feedback associated with persistent long-term climate anomalies of the Walker Circulation (i.e., Southern Oscillation; Walker and Bliss 1932) provided a sound physical basis for ENSO prediction. Bjerknes proposed an interplay between sea surface temperature (SST), surface wind, and thermocline depth changes that result in an infinitely warming ENSO state (Bjerknes 1966, 1969). Two decades later, oscillator mechanisms were proposed to account for the negative feedback required to reverse ENSO, including the delayed oscillator (Suarez and Schopf 1988; Graham and White 1988; Battisti and Hirst 1989), the recharge-discharge oscillator (Jin 1997a, b), the western Pacific oscillator (Weisberg and Wang 1997; Wang et al. 1999), and the advective-reflective oscillator (Picaut et al. 1996, 1997; Delcriox and Picaut 1998). Cane et al. (1986) introduced the first coupled climate model that allowed the combined effects of the atmosphere and the ocean to be tested on the climate system, leading to the first successful prediction of an ENSO event – the 1986 El Niño. Since then, a growing observational network and the development of reanalysis datasets (e.g., Kalnay 1996; Compo et al. 2011; Schneider et al. 2011; Slivinski et al. 2021) greatly improved spatial and temporal resolution of the data, expanded the range of variables that can be measured, and homogenized the available data from various sources. With an evolving physical explanation for ENSO dynamics, the growth of robust observational datasets led to more refined data assimilation methods to approach ENSO prediction as an initial value problem by using SST data to extract ocean memory of ENSO (Zhang et al. 2005; Karspeck and Anderson 2007; Wu et al. 2016; O'Kane et al. 2019).

Despite advances in improving ENSO prediction, model forecast skill decreased significantly after 2000, especially when prediction was made through the boreal spring preceding the ENSO event, known as the spring predictability barrier (Webster and Yang 1992; Latif et al. 1994; Webster 1995; Torrence and Webster 1998; McPhaden 2004; Luo et al. 2008; Yu et al. 2009;

Duan et al. 2009; Duan and Wei 2012; Yu and Fang 2018). Models predicted strong El Niño events that turned out to be weak or neutral events and they failed to forecast the strong El Niño events that did occur. The sharp decrease in forecast skill associated with the spring predictability barrier is widely attributed to initial error growth (Chen et al. 2004; Mu et al. 2007a; Yu et al. 2009; Duan and Wei 2012), in which case ENSO forecast may be improved if data assimilation methods could either filter or reduce initial value errors (Snyder 1996; Mu et al. 2007b; Mu et al. 2014), or if the sources of these errors can be identified and addressed accordingly (Chen et al. 2015; Tian and Ren 2022). In response to rising greenhouse gases (GHG), the growth, development, and decay patterns of ENSO have diversified in terms of amplitude (Trenberth and Hoar 1996; Zhang et al. 2008; Vecchi and Wittenberg 2010), frequency (Trenberth and Hoar 1996; An and Wang 2000; Fedorov and Philander 2000; Kao and Yu 2009), spatial structure (McPhaden 2004; Kao and Yu 2009; Yeh et al. 2009; Timmerman et al. 2018), temporal evolution (McPhaden 1999; Timmerman et al. 2018), and teleconnection (Ashok et al. 2007; Kao and Yu 2009; Wang et al. 2012; Yu et al. 2015; Fosu et al. 2020). Compared to the 1982/83 and 1997/98 extreme El Niño events, the 2015/16 event exhibited a distinct positive SST anomaly center in the central Pacific (CP) and upwelling anomalies under a slightly weaker warm pool in the eastern Pacific (EP; Fig. 1a–c). Studies show that the westward expansion of the warm pool was caused by downwelling equatorial Kelvin waves excited by westerly wind bursts (WWBs; Levine and McPhaden 2016; Lian et al. 2017; Hu and Fedorov 2019). In fact, most El Niños in the past 30 years are classified as CP type events (Wang et al. 2019) preceded by WWBs (McPhaden 2004; Lian et al. 2017; Ineson et al. 2018).

Until the recent decade, ENSO was believed to be a primarily tropical phenomenon as most of its signals (anomalies of SST, surface winds etc.) are observed along the equator. WWBs have been linked to extratropical air–sea interactions (Yu and Rienecker 1998) influenced by the North Pacific Oscillation (NPO), the second leading mode of atmospheric variability in the boreal winter (Walker and Bliss 1932; Rogers 1981; Linkin and Nigam 2008). SST anomalies associated with CP El Niño events can drive changes in NPO circulations by forcing low-frequency variability in

the subtropical lobe of the sea level pressure (SLP) dipole (Di Lorenzo et al. 2010). Conversely, SLP variability of NPO in the boreal winter can trigger a CP El Niño the following winter by weakening the central equatorial Pacific trade winds (Anderson et al. 2013). Subsequent charging of the subsurface heat content can sustain El Niño conditions for up to 12 months from onset (Anderson et al. 2013) via the wind–evaporation–SST (WES) feedback (Xie and Philander 1994). This two-way feedback mechanism between the tropics and the extratropics is expected to generate frequent multi-year El Niño events under anthropogenic warming (Ding et al. 2022), and the occurrence ratio of CP El Niño to EP El Niño is projected to rise by up to five times (Yeh et al. 2009). Studies also found that, when extratropical influence is included with tropical dynamics in regression models for ENSO prediction, correlation scores between predictors and ENSO increase by ~ 0.1 (Boschat et al. 2013; Chen et al. 2020) and root mean square errors (RMSE) are significantly lower (Shi and Ding 2020; Chen et al. 2020). Pegion and Selman (2017) summarized the five major extratropical precursors to ENSO as the Pacific Meridional Mode (PMM; Zhang et al. 2009; Larson and Birtman 2013, 2014; Stuecker 2018; Jia et al. 2021; Fan et al. 2022), Seasonal Footprinting Mechanism (SFM; Vimont et al. 2003; Alexander et al. 2010; Pegion and Alexander 2013; Chen and Yu 2020), Victoria Mode (VM; Bond et al. 2003; Ding et al. 2015; Shi et al. 2022), Trade Wind Charging (TWC; Anderson et al. 2013; Chakravorty et al. 2020; Pivotti et al. 2022), and the western North Pacific SST (WNP; Wang et al. 2012; 2013, 2015; Fosu et al. 2020). While the first four precursors initiate ENSO mainly by linking the equatorial Pacific to NPO, Wang et al. (2012) show that anomalous westerlies related to WNP SST variability can also directly induce Kelvin waves in the western Pacific and are more likely to trigger ENSO compared to other precursors.

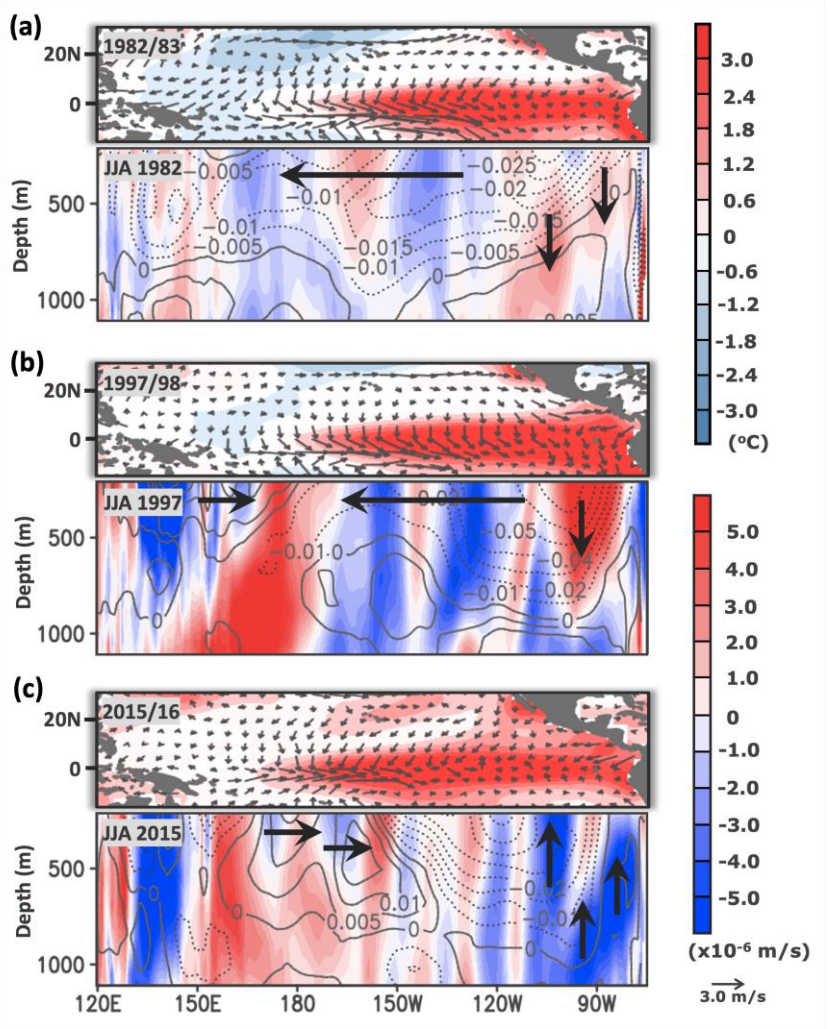

Fig. 1 Maps and vertical cross-sections depicting atmospheric and oceanic conditions in the equatorial Pacific related to the (a) 1982/83, (b) 1997/98, and (c) 2015/16 extreme El Niños. Maps show anomalies of (DJF+1) surface winds (m/s; vectors) and sea surface temperature (°C; shading – top color bar). Cross-sections (zonally averaged between 7°N and 7°S) show anomalies of JJA surface zonal currents (m/s; contours) and vertical velocity (m/s; shading – bottom color bar). Positive SST anomalies along the equator stretch further west during the 2015/16 El Niño compared to the two earlier events. Westerly wind anomalies in the western Pacific during the El Niño terminate over the central Pacific SST anomaly center in 2015/16 but travel further east in 1982/83 and 1997/98. Westerly surface currents develop in the western Pacific in JJA 1997 and JJA 2015, extending further east into the central Pacific in 2015. Downwelling anomalies in the eastern Pacific are stronger in JJA 1997 than JJA 1982. Upwelling anomalies occur in the eastern Pacific in JJA 2015.

The WNP mode is characterized by an SST anomaly dipole in the boreal winter (DJF) from the western North Pacific along the Kuroshio extension to the central–eastern equatorial Pacific (Wang et al. 2012, 2013; Pegion and Selman 2017). A cold WNP phase is defined by cold SST

anomalies in the western North Pacific and warm SST anomalies towards the equatorial Pacific. This temperature gradient induces a pressure gradient that generates northerly to northwesterly surface winds (Wang et al. 2012). Kelvin waves resulting from the wind stress anomalies in the western equatorial Pacific propagate towards the central–eastern equatorial Pacific in the following seasons, transporting energy to produce a warm pool of water by the next winter (DJF+1), and leading to an El Niño (Wang et al. 2012). This chapter uses the abbreviation WNP and the expanded form western North Pacific to distinguish between the *dynamics associated with a WNP phase* and the *geographic location*, respectively. For 1-year lead time, a cold WNP phase precedes a warm ENSO phase, and a warm WNP phase precedes a cold ENSO phase with wind direction reversed (Wang et al. 2012). CP type ENSO is less related to thermocline variation and more a response to atmospheric forcing (Kao and Yu 2009) enhanced by climate warming (Yeh et al. 2009; Shi et al. 2022), yet initial thermocline state is an optimal precursor in determining whether a CP or EP El Niño will develop (Capotondi and Sardeshmukh 2015). By using partially coupled experiments, Fosu et al. (2020) show that WNP-induced Kelvin waves affect the mean thermocline state by more effectively advecting warm water towards the eastern Pacific, causing SST variability in the western North Pacific to favor EP ENSO over CP ENSO due to stronger thermocline feedback. The growing association between WNP and ENSO with anthropogenic warming in recent decades (Wang et al. 2013) merits further studies on how future warming will affect this relationship. Furthermore, the conflicting impacts of climate change and WNP SST variability on ENSO diversity raise the question as to how the WNP–ENSO relationship will affect ENSO diversity as warming progresses.

In this study, we focus on the extended ENSO prediction and its associated change by examining the impact of future warming on the dynamics underlying the 1-year lead relationship between a cold WNP phase and an El Niño. We use a conditional probability approach and SST budget analysis to assess how warming-induced changes to this relationship will likely affect future ENSO diversity. The WNP may sometimes be interconnected with PMM and other ENSO

precursors, which collectively increase the likelihood of triggering an ENSO (Wang et al. 2015). The recent amplification of PMM and its strengthening impact on ENSO (Yu et al. 2015; Jia et al. 2021; Fan et al. 2022) extend the broader implications of this work towards how interactions between multiple evolving extratropical influences will shape ENSO in a warming world.

2.3 Methodology

2.3.1 Data

All observational and model data used in this study are monthly data. SST reanalysis data of 2° resolution are from the National Ocean and Atmospheric Administration (NOAA) Extended Reconstructed Sea Surface Temperature (ERSST) Version 5 dataset (Huang et al. 2017). Surface winds of 2.5° resolution are from the National Centers for Environmental Prediction/National Center for Atmospheric Research (NCEP/NCAR) Reanalysis 1 (R1; Kalnay et al. 1996). Ocean data for vertical velocity and zonal currents of 1/3° resolution were obtained from NCEP Global Ocean Data Assimilation System (GODAS; Behringer at al. 1998; Behringer and Xue 2004). Both GODAS variables have data for 40 vertical levels with 10 m resolution in the upper 200 m (Behringer and Xue 2004). The model outputs used in this study are historical (1850–2014) and Shared Socioeconomic Pathway 3–7.0 (SSP370; 2015–2100) runs composed of 50 ensembles of 1° resolution Community Earth System Model Version 2 Large Ensembles (CESM2-LE; Danabasoglu et al. 2020; Rodgers et al. 2021) data and 86 ensembles of varying resolutions of Coupled Model Intercomparison Project Phase 6 (CMIP6; Eyring et al. 2016) data (Table 2.1). All CMIP6 models were regridded to 1° resolution for averaging. SST and zonal and meridional surface winds were obtained for historical and SSP370 runs of both CMIP6 and CESM2-LE datasets. Additional CESM2-LE variables were acquired for SST budget analysis, including mixed layer depth, sea surface height, zonal and meridional wind stress, solar shortwave heat flux, and total surface heat flux including shortwave flux. The base WNP index is the SST anomaly averaged across coordinates 18°N–28°N and 122°E–132°E (Wang et al. 2012). The Niño 3.4 index is the

SST anomaly averaged across coordinates 5°S–5°N and 170°W–120°W (Kaplan et al. 1998). All model data were detrended prior to analysis to focus on the dynamics associated with interannual variability.

Table 2.1. List of CMIP6 models used in this study; horizontal resolution (latitude × longitude) and ensemble size.

ACRONYM	MODEL NAME	ORGANIZATION, COUNTRY (REFERENCE)	RESOLUTION	ENSEMBLES
CanESM5	Fifth Generation Canadian Earth System Model	Canadian Centre for Climate Modelling and Analysis, Canada (Swart et al. 2019)	2.8°×2.8°	50
CNRM-ESM2-1	Centre National de Recherches Météorologiques Earth System Model, version 2	Centre National de Recherches Météorologiques/Centre Européen de Recherche et de Formation Avancée en Calcul Scientifique, France (Séférian et al. 2019)	1.4°×1.4°	5
GISS-E2-1-G	Goddard Institute for Space Studies Model E2	National Aeronautics and Space Administration Goddard Institute for Space Studies, USA (Kelley et al. 2020)	2.5°×2°	5
IPSL-CM6A-LR	Institut Pierre-Simon Laplace climate model, Low Resolution, for Phase 6 of CMIP	Institut Pierre-Simon Laplace Climate Modelling Centre, France (Boucher et al. 2020)	2.5°×1.26°	4
MIROC-ES2L	Model for Interdisciplinary Research on Climate, Earth System version 2 for Long-term simulations (MIROC-ES2L) Earth system model (ESM)	Japan Agency for Marine-Earth Science and Technology, Atmosphere and Ocean Research Institute (The University of Tokyo), and National Institute for Environmental Studies, Japan (Hajima et al. 2020)	2.8°×2.8°	10
MIROC6	Model for Interdisciplinary Research on Climate, version 6	Japan Agency for Marine-Earth Science and Technology, Atmosphere and Ocean Research Institute (The University of Tokyo), and National Institute for	1.4°×1.4°	3

		Environmental Studies, Japan (Tatebe et al. 2019)		
MRI-ESM2-0	Meteorological Research Institute Earth System Model Version 2.0	Meteorological Research Institute of the Japan Meteorological Agency, Japan (Yukimoto et al. 2019)	1.125°×1.125°	5
UKESM1-0-LL	U.K. Earth System Model, version 1, Low Resolutions for Land and Ocean	Met Office Hadley Centre, U.K. (Sellar et al. 2019)	1.875°×1.25°	4

2.3.2 Definitions of "warm events" and "cold events"

A conditional probability approach was used to construct all anomaly composite maps and histograms from model data. All anomalies were calculated from 30-year moving averages. Criteria were specified to focus on the impact of WNP air–sea interactions on ENSO dynamics. SST and surface wind anomaly composite maps of CMIP6 (Fig. 2) and CESM2-LE (Fig. 3) were produced for strong El Niño years that were preceded by cold WNP years the previous winter i.e., > 0.5°C cooling in the western North Pacific in DJF and > 1.0°C warming in the Niño 3.4 region in DJF+1. Events that meet this criterion were categorized into either "warm events" or "cold events". "Warm events" for all anomaly composite maps in this study are defined as events that were derived from ensembles for which the difference between the spatially averaged $(DJF+1)$SST anomaly composites of SSP370 and historical runs (equation 1) produce a warmer central–eastern equatorial Pacific (i.e., stronger future El Niño). We define the central–eastern equatorial Pacific region as the area bound by 5°S–5°N and 170°W–80°W (boxed area along the equator in Figs. 2 and 3). For each ensemble e = 1, 2, … 86 of CMIP6, or e = 1, 2, … 50 of CESM2-LE, the expression used to classify the events is:

$$(DJF+1)SST_{\mathrm{SSP}_e} - (DJF+1)SST_{\mathrm{HIST}_e} = \left[\frac{1}{n_e}\sum_{j=1}^{n_e}(DJF+1)\mathrm{SST}_j\right] - \left[\frac{1}{m_e}\sum_{i=1}^{m_e}(DJF+1)\mathrm{SST}_i\right] \quad \ldots (1)$$

where an event is defined as a year with > 0.5°C cooling in the western North Pacific in DJF followed by > 1.0°C warming in Niño 3.4 in DJF+1. Equation (1) can be decomposed as follows:

$(DJF+1)\mathrm{SST}_i$ is the $(DJF+1)$SST of the i^{th} event of the e^{th} ensemble of historical runs,

$(DJF+1)\mathrm{SST}_j$ is the $(DJF+1)$SST of the j^{th} event of the e^{th} ensemble of SSP370 runs,

m_e is the frequency of historical events of the e^{th} ensemble,

n_e is the frequency of SSP370 events of the e^{th} ensemble,

$(DJF+1)SST_{\mathrm{HIST}_e}$ is the average $(DJF+1)$SST of the m_e historical events, and

$(DJF+1)SST_{\mathrm{SSP}_e}$ is the average $(DJF+1)$SST of the n_e SSP370 events.

To avoid skewing the CMIP6 results towards the Canadian model (CanESM5) that has a significantly large number of ensembles compared to other models, we produced another CMIP6 SST and surface wind anomaly composite using "warm events" from 3–5 ensembles per model (Fig. S1). Events for both CMIP6 composites were collected from 31-year periods at the end of each run, i.e., 1980–2010 for historical runs, and 2070–2100 for SSP370 runs. As no CESM2 ensemble is able to simulate the observed slowdown of warming in recent decades (Danabasoglu et al. 2020), events for the CESM2-LE composites were compiled from an earlier 31-year range with relatively lower warming rates within historical runs i.e., 1890–1920, and paired with 2070–2100 for SSP370 runs.

If the e^{th} ensemble satisfies the criterion $(DJF+1)SST_{\mathrm{SSP}_e} - (DJF+1)SST_{\mathrm{HIST}_e} > 0$ for $m_e, n_e \neq 0$, the events were categorized under "warm events". Similarly, if the e^{th} ensemble satisfies the criterion $(DJF+1)SST_{\mathrm{SSP}_e} - (DJF+1)SST_{\mathrm{HIST}_e} < 0$ for $m_e, n_e \neq 0$, a colder DJF+1 anomaly is produced in the central–eastern equatorial Pacific and the events were categorized as "cold events" (i.e., weaker future El Niño). If $m_e = 0$ and $n_e \neq 0$, the events of SSP370 runs were categorized into "warm events", as no historical events match the criterion. Alternately, if $n_e = 0$ and $m_e \neq 0$, the events of historical runs were categorized into "cold

events", with no SSP370 events to match the criterion. If $m_e, n_e = 0$, or $(DJF+1)SST_{\mathrm{SSP}_e} - (DJF+1)SST_{\mathrm{HIST}_e} \sim 0$ for $m_e, n_e \neq 0$, the ensemble was excluded from classification into either category.

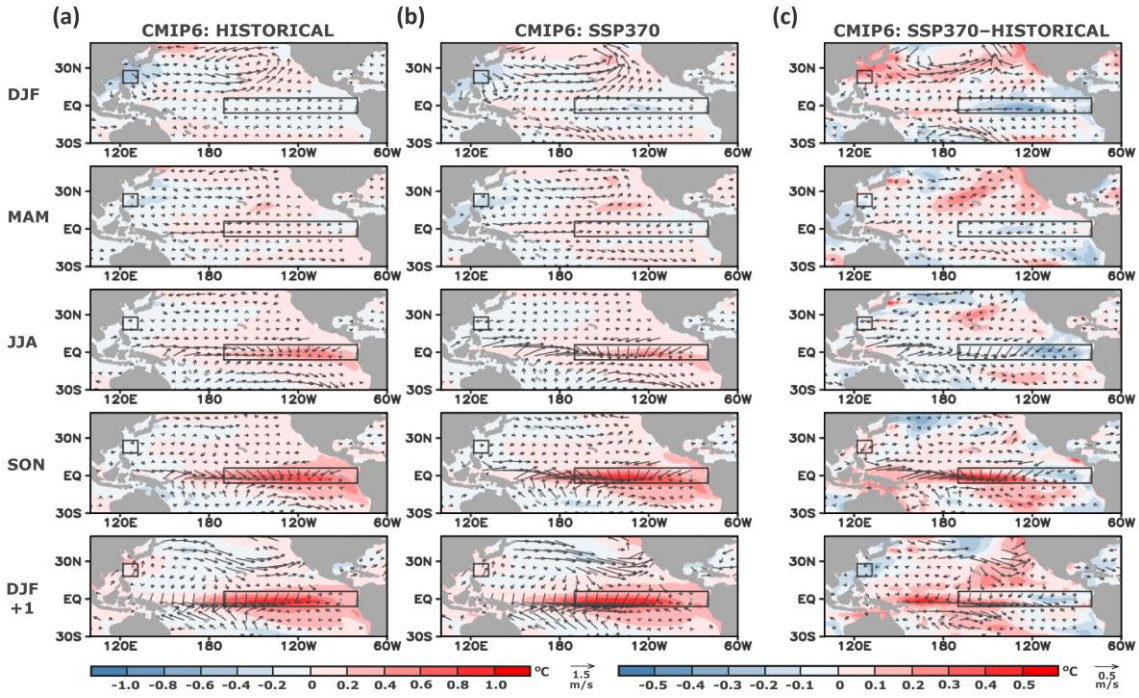

Fig. 2 CMIP6 SST and surface wind anomaly composites of "warm events". Columns represent (a) historical runs, (b) SSP370 runs, and (c) SSP370–historical difference. Rows represent seasonal evolution from the cold WNP (DJF) to the El Niño (DJF+1). Left scale bar and arrow legend are for (a) and (b). Right scale bar and arrow legend are for (c).

The definitions of "warm events" and "cold events" in the frequency comparisons (Fig. 4a, b) vary slightly from those used to construct the anomaly composite maps. Instead of comparing $(DJF+1)$SST between historical and SSP370 scenarios as expressed in equation (1), the comparisons were made between earlier and later 31-year periods within each scenario of both models to further breakdown the effect of warming on the 1-year lead relationship between WNP and ENSO (Fig. 4a, b). The 31-year periods used are 1890–1920 for earlier historical runs, 1980–2010 for later historical runs, 2047–2077 for earlier SSP370 runs, and 2070–2100 for later SSP370 runs. As all anomalies were calculated from 30-year moving averages and the SSP370 runs span

only 86 years, an 8-year overlap exists between the selected SSP370 periods. For each ensemble e of the historical scenario, we calculated $(DJF+1)SST_{\text{HIST\_late}_e} - (DJF+1)SST_{\text{HIST\_early}_e}$, where $(DJF+1)SST_{\text{HIST\_early}_e}$ is the average $(DJF+1)$SST of the earlier historical events of the e^{th} ensemble, and $(DJF+1)SST_{\text{HIST\_late}_e}$ is the average $(DJF+1)$SST of the later historical events of the e^{th} ensemble. The process was repeated with SSP370 runs. We reapplied the same classification approach as the anomaly composite maps by using the differences in the central–eastern equatorial Pacific SST anomalies between periods to categorize the events into "warm events" and "cold events" within each scenario for the histograms (Fig. 4a, b). We also plotted a time series histogram to compile the annual frequencies of all CMIP6 historical (DJF+1) El Niños preceded by summer (JJA) westerly wind anomalies in the western equatorial Pacific (Fig. 5). As no WNP anomalies were specified for Figure 5, these westerly anomalies may be associated with extratropical precursors as demonstrated in this study or other dynamics not included in this study. The purpose of Figure 5 is to examine how the association between El Niños and WWBs changes in a warming climate regardless of how the westerly anomalies may be triggered.

To identify years where a cold WNP phase was followed by ENSO initiation or development mechanisms, we defined additional criteria by specifying anomalies of DJF western North Pacific surface northerlies > 0.5 m/s (5°N–25°N and 122°E–142°E), JJA western equatorial Pacific surface westerlies > 0.5 m/s (5°S–10°N and 130°E–180°E), DJF+1 eastern equatorial Pacific mixed layer deepening (7°S–5°N and 110°W–80°W) and DJF+1 eastern equatorial Pacific sea surface height increase > 2.0 m (7°S–5°N and 120°W–80°W) for both historical and SSP370 scenarios (Fig. 6a, b). We included cold DJF SST anomalies (SSTA < –0.5°C) in the western North Pacific in each set of the new criteria but excluded DJF+1 Niño 3.4 SST warming to ensure that the patterns produced from these composites were mostly associated with a cold DJF WNP regardless of whether an El Niño occurred the next winter. We plotted the frequencies of historical

and SSP370 events that satisfy the criteria of cold WNP phase being followed by ENSO initiation in each scenario (Fig. 6c, d).

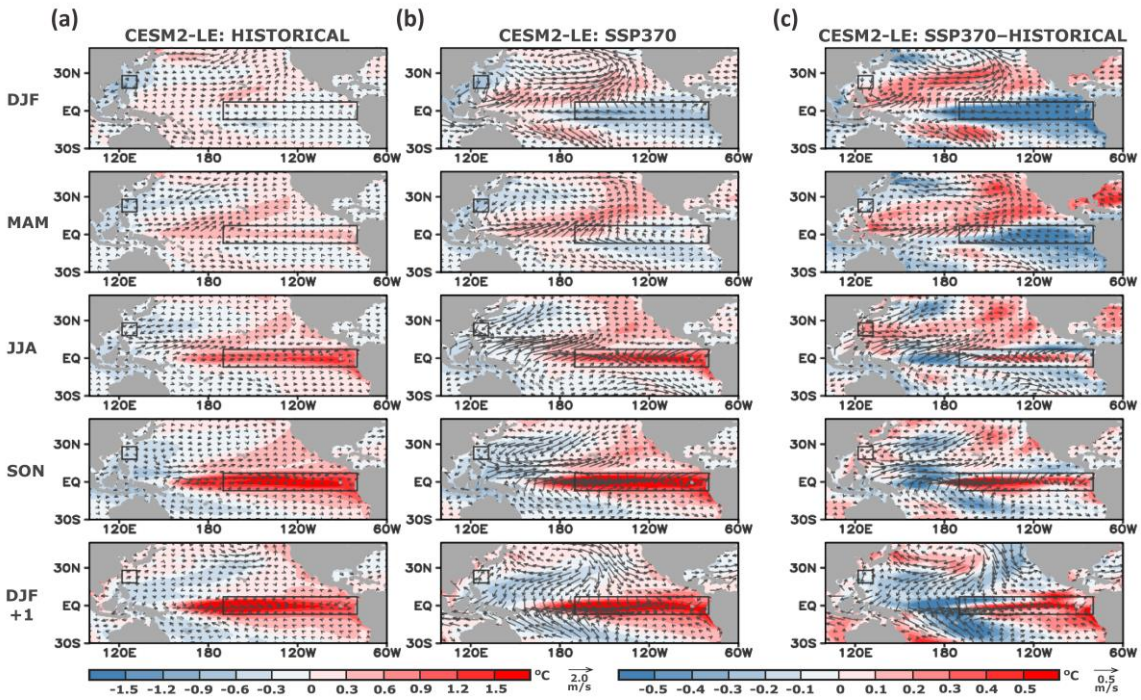

Fig. 3 CESM2-LE SST and surface wind anomaly composites of "warm events". Columns represent (a) historical runs, (b) SSP370 runs, and (c) SSP370–historical difference. Rows represent seasonal evolution from the cold WNP (DJF) to the El Niño (DJF+1). Left scale bar and arrow legend are for (a) and (b). Right scale bar and arrow legend are for (c).

2.3.3 SST budget analysis

To study thermal evolution of ocean surface mixed layer under enhanced warming, SST budget analysis was performed on historical and SSP370 runs of CESM2-LE data. The top of the mixed layer is in contact with sunlight; the base of the layer is in contact with colder water below. The strong vertical temperature gradient combined with surface winds that advect mass and energy make the mixed layer a very dynamic zone of heat exchange between the atmosphere and the ocean. The mixed layer temperature tendency equation is given by (Dong et al. 2007):

$$\underbrace{\frac{\partial T_m}{\partial t}}_{\text{Temperature tendency}} = \underbrace{\frac{Q_{net}-q(-d_m)}{\rho_o c_p d_m}}_{\text{Air–sea heat flux}} \underbrace{-\left(\frac{\tau}{\rho_o f d_m}+\frac{-g\nabla\eta}{f}\right).\nabla T_m}_{\text{Advection (Ekman + geostrophic)}} \underbrace{+\kappa\nabla^2 T_m}_{\text{Diffusion}} \underbrace{-\frac{w_e \Delta T}{d_m}}_{\text{Entrainment}} \quad \ldots (2)$$

where T_m is the mixed layer temperature, Q_{net} is the net surface heat flux, d_m is the mixed layer depth, $q(-d_m)$ is the downward radiative heat flux at the bottom of the mixed layer, ρ_o is the density of seawater, c_p is the specific heat of sea water at constant pressure, u_m is the horizontal velocity of mixed layer, κ is the horizontal eddy diffusivity coefficient, w_e is the entrainment velocity, and ΔT is the temperature difference between the mixed layer and the layer just below.

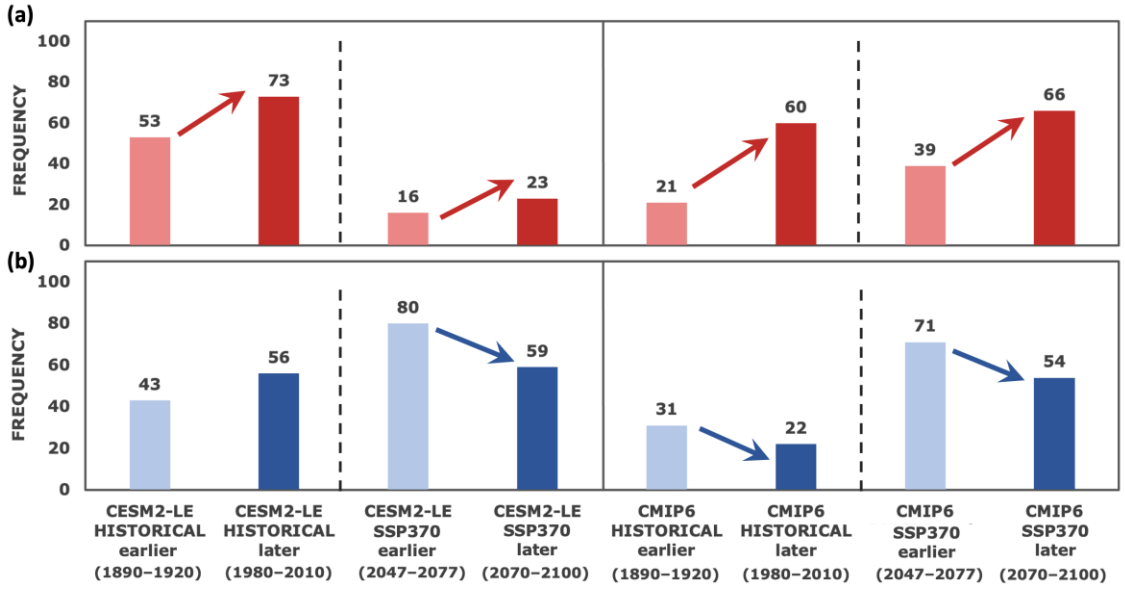

Fig. 4 (a) Histograms showing frequencies of "warm events" of earlier and later periods within each model scenario. (b) same as (a) except for "cold events". The frequencies of "warm events" increase with enhanced warming. With the exception of CESM2-LE historical early runs, the frequencies of "cold events" decrease with enhanced warming.

The temperature tendency term on the left-hand side (LHS) of equation (2) is the sum of 4 modes and/or directions of heat transfer on the right-hand side (RHS): air–sea heat flux, entrainment, diffusion, and advection which is subdivided into the Ekman and geostrophic

components. We produced anomaly composites (Figs. 7, 8 and 10, Figs. S2, 3) of all terms on the RHS of equation (2) for the "warm years" determined from equation (1). The equatorial data are missing in Figs. 7–9 because the Ekman vertical velocity (w_e) is inversely proportional to the Coriolis parameter f (i.e., $w_e \propto f^{-1}$). Since f is approximately zero near the equator, w_e is undefined near the equator.

2.3.4 Closed system of the SST budget equation

To verify closed system between the SST budget terms, we plotted (i) point-to-point correlation of the LHS of the equation with the RHS (Fig. S4) and (ii) temporal evolution of the LHS with each term on the RHS and their sum within two regions of interest (Fig. S5a, b). The point-to-point correlation and time series were calculated for each of the 50 CESM2 large ensembles and averaged. Fisher's Z transformation (Fisher 1915) was used to calculate the average correlation coefficient and is expressed as:

$$Z_{\text{ave}} = \frac{1}{2n}\sum_{i=1}^{n} \ln\left[\frac{1+r_i}{1-r_i}\right] \dots (3)$$

$$r_{\text{ave}} = \tanh(Z_{\text{ave}}) = \left[\frac{e^{Z_{\text{ave}}} - e^{-Z_{\text{ave}}}}{e^{Z_{\text{ave}}} + e^{-Z_{\text{ave}}}}\right] \quad \dots (4)$$

where n is the total number of ensembles (i.e., 50 ensembles for CESM2), r_i is the correlation coefficient of i^{th} ensemble, Z_{ave} is the average Z score and r_{ave} is the average correlation coefficient. Each ensemble has a Pearson correlation coefficient of > 0.8 over vast areas of the oceans (not shown) and the global ensemble mean using Fisher's Z transformation is > 0.6 (equations 3 and 4; Fig. S4). The temporal evolution of the RHS is also in close agreement with that of the LHS (Fig. S5a, b).

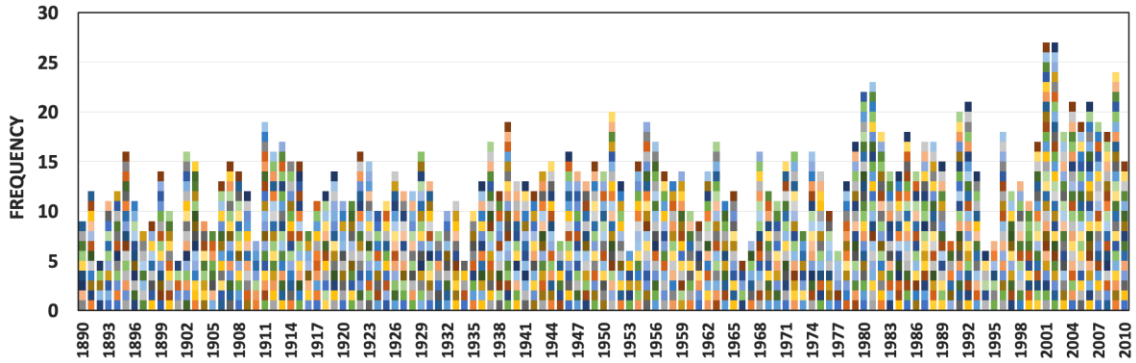

Fig. 5 Histogram showing frequencies of all (DJF+1) El Niños (>0.6) preceded by JJA westerly anomalies in the western equatorial Pacific. These westerly anomalies may be associated with extratropical precursors as demonstrated in this study or other dynamics not included in this study. The different colored bars represent contributions from each ensemble of the CMIP6 historical scenario that produces a match for a JJA westerly preceded El Niño event.

2.4 Results

Seasonal evolution of SST and surface wind anomaly composite maps of CMIP6 (Fig. 2) and CESM2-LE (Fig. 3) historical and SSP370 runs depict the dynamics of the 1-year lead relationship between WNP (DJF) and ENSO (DJF+1). A cold WNP phase is marked by cold SST anomalies in the western North Pacific region in the boreal winter and low-level northerlies to northwesterlies flowing towards the western equatorial Pacific (Figs. 2 and 3), where springtime (MAM) westerly anomalies emerge and strengthen in the following seasons. Off-equatorial MAM southwesterlies of a positive PMM phase are also generated in the western Pacific of CESM2-LE (Fig. 3). In JJA, the westerlies start to converge in the central equatorial Pacific and a central–eastern equatorial Pacific warm pool begins to develop (Figs. 2 and 3). As surface convergence intensifies in fall, the warm pool amplifies, and an El Niño occurs by the following winter. Although these defining features are evident in both historical and SSP370 composites, the magnitude and/or location of the peak anomalies vary between the two scenarios. In SON, the greatest increase in equatorial SSTs with future warming occurs in the central Pacific. Compared to their respective historical El Niños, the CESM2-LE SSP370 warm pool spreads from the central Pacific further towards the eastern Pacific (Fig. 3), while a strengthened western Pacific warm pool

is observed in the CMIP6 SSP370 composite (Fig. 2, Fig. S1). But qualitatively speaking, the WNP DJF northerlies, summer to fall western Pacific westerlies, and surface convergence in the central equatorial Pacific leading up to the El Niño are considerably stronger in the SSP370 scenarios of both models (Figs. 2 and 3).

The frequency comparisons of earlier and later 31-year periods within each scenario in Figure 4 complement the anomaly composite depictions of strengthened WNP–ENSO dynamics with enhanced warming in Figures 2 and 3. “Warm events” are more frequent for all later periods of historical and SSP370 runs of CMIP6 and CESM2-LE (Fig. 4a). “Cold events” are less frequent for later periods of CMIP6 historical and SSP370 runs, and CESM2-LE SSP370 runs (Fig. 4b). The slight increase in frequency of “cold events” in the later period of CESM2-LE historical runs (Fig. 4b) may be linked to the limitation of CESM2 ensembles in capturing the observed weakening of the warming trend in recent decades (Danabasoglu et al. 2020) or amplified low-frequency natural variability (Wang et al. 2013). The overall increasing (decreasing) frequencies of later “warm events” (“cold events”) nevertheless indicate that climate warming increases the probability of WNP-induced El Niños (Fig. 4a).

Combined with the intensification of JJA westerlies in the western equatorial Pacific of future scenarios (Figs. 2 and 3), the rise in annual frequencies of CMIP6 historical events of El Niños preceded by summer westerlies in the last 30 years of the runs (Fig. 5) indicates a growing association between El Niños and JJA westerly anomalies under enhanced warming. Lead–lag relationships in Figure 6 dynamically link the WNP influence to the tropical oceanic precursors of El Niño through the summer westerlies. Decreasing (increasing) sea surface height and shoaling (deepening) of the mixed layer depth in the western (eastern) equatorial Pacific 1 year after a cold WNP phase (Fig. 6a, b) are consistent with advection of water and propagation of thermocline anomalies from the western Pacific to the central–eastern Pacific driven by equatorial wind stress under extratropical influence. These E–W gradients are stronger in the SSP370 scenario. The frequencies of cold WNP events (i) coinciding with WNP DJF northerly wind anomalies followed

by positive (DJF+1) sea surface height anomalies in the eastern equatorial Pacific (Fig. 6c), and (ii) followed by the JJA westerly wind anomalies in the western equatorial Pacific and positive (DJF+1) mixed layer depth anomalies in the eastern equatorial Pacific (Fig. 6d), increase with future warming.

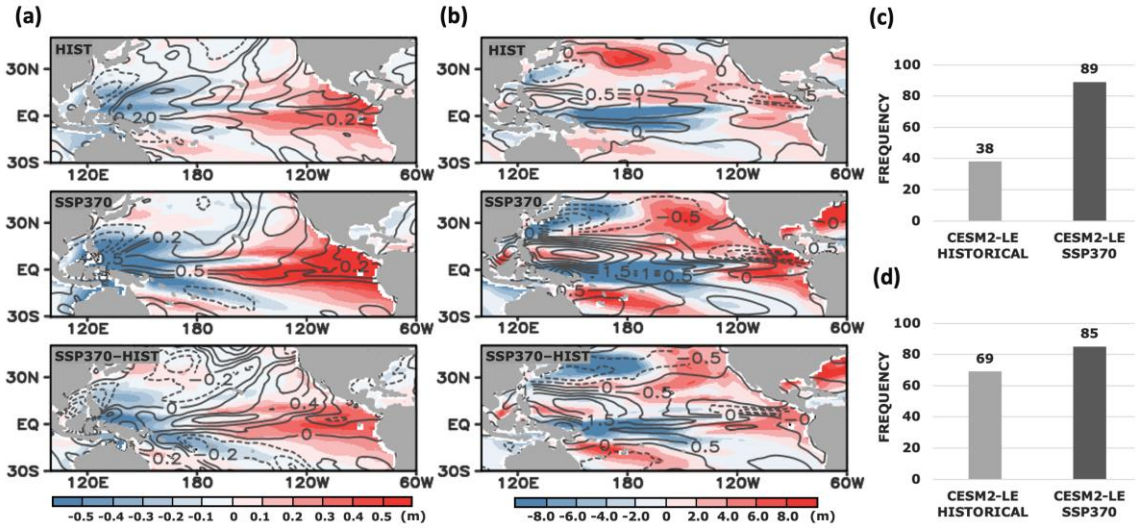

Fig. 6 CESM2-LE anomaly composites of "warm events". (a) DJF meridional surface wind anomalies (m/s; contours) and (DJF+1) sea surface height anomalies (m; shading – left scale bar). (b) JJA zonal surface wind anomalies (m/s; contours) and (DJF+1) mixed layer depth anomalies (m; shading – right scale bar). The histograms on the right show the historical and SSP370 frequencies of cold WNP events (c) coinciding with DJF northerly wind anomalies from the western North Pacific to western equatorial Pacific followed by positive (DJF+1) sea surface height anomalies in the eastern equatorial Pacific, and (d) followed by JJA westerly wind anomalies in the western equatorial Pacific and positive (DJF+1) mixed layer depth anomalies in the eastern equatorial Pacific.

As both amplitude and frequencies of the El Niño precursor patterns in the upper ocean increase with warming, SST budget analysis can help break down the distribution of heat in the mixed layer (equation 2). As shown in Figure 7, the Ekman heat advection anomaly composite maps account for heat being transported by wind-driven Ekman currents in the 1-year lead WNP–ENSO relationship. Ekman transport in the E–W equatorial Pacific causes a tilt in sea surface height by creating areas of convergence and divergence and affects the mixed layer depth gradients by causing downwelling and upwelling (Elias 2021). The geostrophic heat advection anomaly

composites in Figure 8 display similar spatial patterns as Ekman heat advection, with the signs reversed. Positive (negative) fluxes indicate divergent (convergent) zones of Ekman (Fig. 7) and geostrophic (Fig. 8) heat. In MAM, an anomaly of Ekman heat convergence (and geostrophic heat divergence) develops in the central–eastern equatorial Pacific, where it strengthens and expands further west in the seasons leading up to the El Niño. These patterns are stronger in SSP370 than historical runs and synchronous with the development of SON maximum positive SST anomalies and surface convergence in the central Pacific with future warming (Figs. 2 and 3).

The central equatorial Pacific heat anomalies in Figures 7 and 8 can be linked to the equatorial Pacific zonal winds. WWBs are reported to increase the ocean heat content more rapidly by promoting Ekman convergence (Hu and Federov 2019). Near the equator, the climatological mean annual Ekman vertical velocity is positive, and the mean annual wind stress is easterly (Webster 2020). Ekman advection under non-El Niño conditions is divergent from approximately 5°S to 5°N of the Pacific Ocean. The net water transport is from the equator, where surface outflow is replaced by upwelling, towards the centers of the Pacific subtropical gyres of both hemispheres. Geostrophic convergence is a response to the Ekman divergence to balance variations in sea surface height from the subtropical gyres to the equator. Typically, Ekman (geostrophic) advection along the equator has a cooling (warming) effect (Dong and Kelly 2004). During an El Niño, weakening of the easterly trade winds by anomalous westerlies weaken Ekman heat divergence and upwelling in the central–eastern equatorial Pacific. Strong westerly anomalies may even reverse the direction of the trade winds and promote Ekman convergence (and subsequently geostrophic divergence) at the equator by advecting warm water more effectively towards the central–eastern Pacific (Figs. 7 and 8).

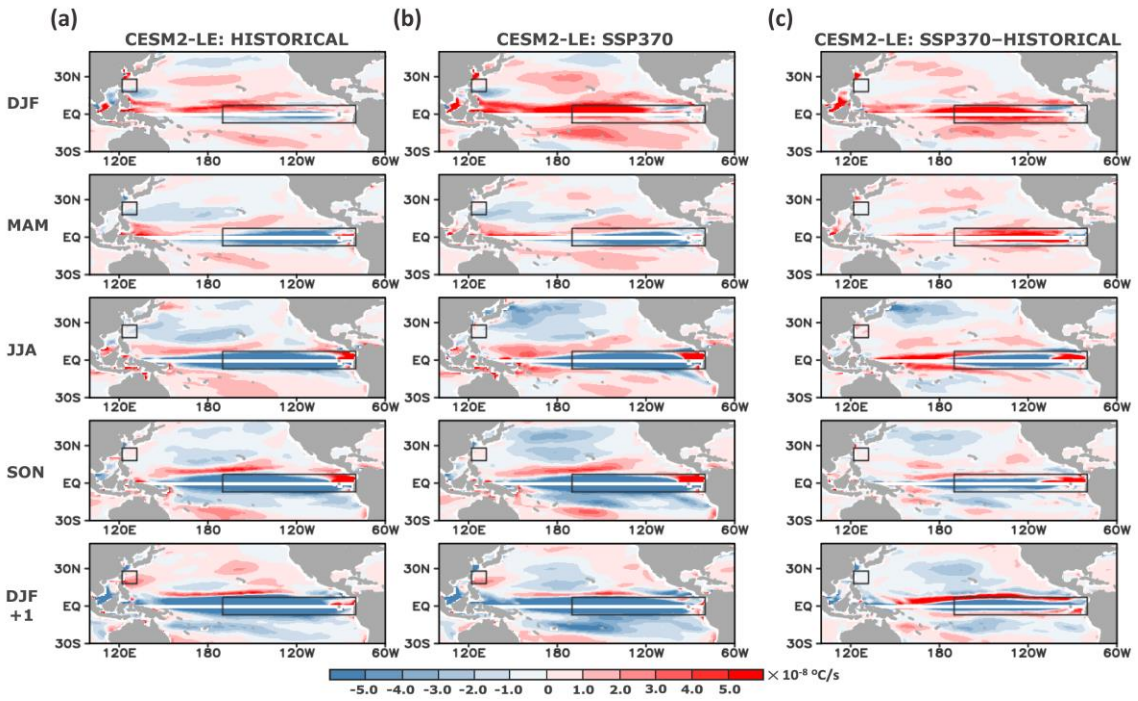

Fig. 7 CESM2-LE Ekman heat advection composites of "warm events". Columns represent (a) historical runs, (b) SSP370 runs, and (c) SSP370–historical difference. Rows represent seasonal evolution from the cold WNP (DJF) to the El Niño (DJF+1). The Ekman vertical velocity is undefined at the equator where the Coriolis parameter is zero.

The signs of Ekman and geostrophic heat advection tend to abruptly reverse in narrow zones just outside the central equatorial Pacific center, especially for the SSP370–historical composites (Figs. 7–9). While wind direction does not necessarily have to reverse for a transition to occur between convergence and divergence of the advection terms (Talley et al. 2011), the varying wind speeds in the same direction can cause sudden changes in wind stress curl and promote strengthened downwelling and upwelling in adjacent zones (Fig. 9). The westerly wind anomalies strengthen a few degrees away from the equator in the central Pacific but weaken outside the convergence zone changing the wind stress curl to cyclonic. As a result, the flow becomes more divergent (convergent) or positive (negative) away from the central equatorial Pacific convergent (divergent) centers of Ekman (geostrophic) heat advection from MAM to DJF+1. With SSP370 warming, the opposite wind stress curl anomalies from 0 to 10 degrees of the Northern (Southern) hemisphere promote southward (northward) transport of warmer water from zones of Ekman

divergence where upwelling anomalies are produced, towards the downwelling areas of Ekman convergence to balance the meridional sea surface height gradient (Fig. 9). WNP influence under future warming is more likely to strengthen Ekman heat convergence (and geostrophic heat divergence) in the central equatorial Pacific to promote an easier transition to El Niño (Figs. 7 and 8).

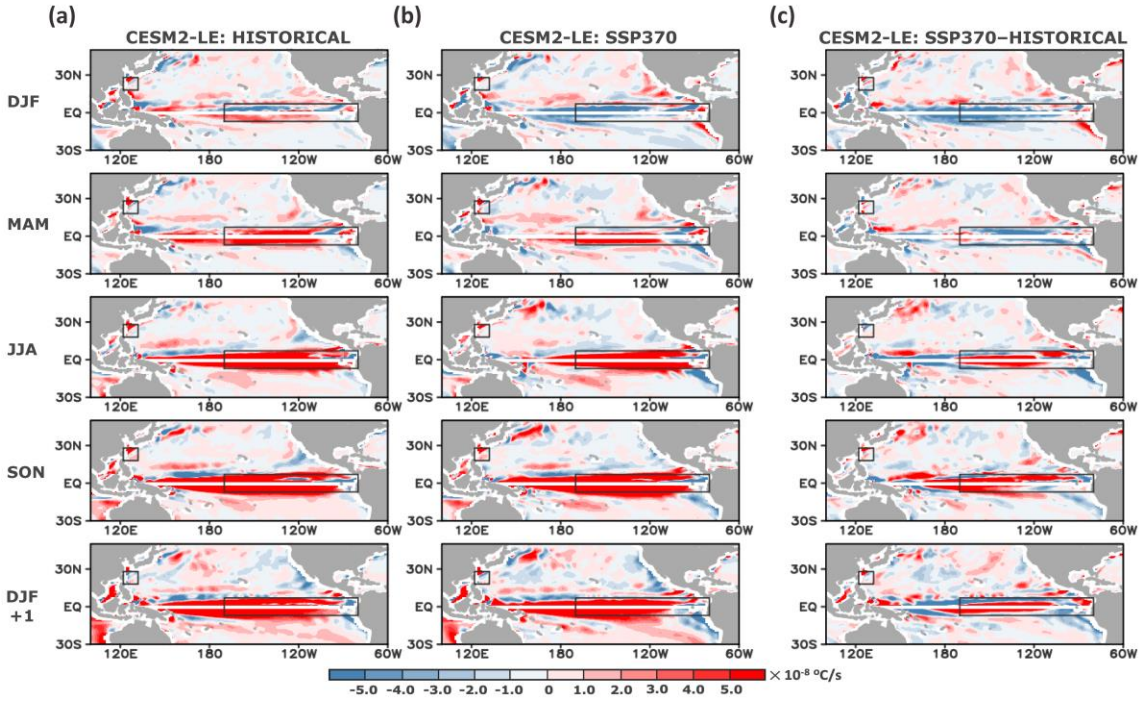

Fig. 8 CESM2-LE geostrophic heat advection composites of "warm events". Columns represent (a) historical runs, (b) SSP370 runs, and (c) SSP370–historical difference. Rows represent seasonal evolution from the cold WNP (DJF) to the El Niño (DJF+1). The Ekman vertical velocity is undefined at the equator where the Coriolis parameter is zero.

Lastly, the entrainment anomaly composite maps in Figure 10 show how heat flux between the mixed layer and the water below changes with future warming in the 1-year lead relationship between WNP (DJF) and ENSO (DJF+1). Positive (negative) fluxes indicate movement of heat from the water below (mixed layer) into the mixed layer (water below). The entrainment temperature can modulate the relative strength of zonal advection and thermocline feedback in a coupled system, which can affect growth and development of SST anomalies. ENSO-related SST anomalies prior to 1980 were initiated in the eastern Pacific before propagating westward along the

equator (Rasmusson and Carpenter 1982). However, the first appearance of the SST anomalies since 1980 occurs in the central Pacific and then propagates eastward during the development phase (Wallace et al. 1998). These changes have been attributed to decadal shifts in entrainment temperatures pre- and post- 1980 (Zhu et al. 2011). Entrainment prior to 1980 favored thermocline feedback during the growth phase of ENSO and zonal advective feedback during transition phase of ENSO. In contrast, entrainment after 1980 contributes to thermocline feedback during the growth and longer lasting transition of ENSO and weakens the zonal advective feedback. Eastward propagation of downwelling equatorial Kelvin waves along the Pacific thermocline can entrain the thermocline anomalies into the mixed layer and shift positive SST and sea surface height anomalies to the eastern Pacific (Zhou and Zhu 2009). Positive entrainment anomalies occur in both scenarios across most of the E–W equatorial Pacific in the seasons leading up to the El Niño (Fig. 10). The stronger SSP370 entrainment anomaly center between 150°W and 110°W during the WNP to ENSO transition period (Fig. 10) is consistent with initiation of SSTs in the central Pacific with climate change (Fig. 3). Therefore, future warming may strengthen basin-wide entrainment during the transition period and shift the thermocline anomalies towards the central–eastern Pacific (Fig. 10) to promote eastward expansion of the warm pool during an El Niño under WNP influence (Fig. 3).

I note how heat flux between the mixed layer and the atmosphere change with future warming in the WNP–ENSO relationship by plotting the air–sea heat flux anomaly composite maps (Fig. S2). Positive (negative) fluxes indicate movement of heat from air (sea) to sea (air). Strong negative fluxes in the equatorial Pacific become more prominent in the seasons leading up to an El Niño (Fig. S2). As the patterns of air–sea heat flux appear to simply be a response to a strengthened temperature gradient from the ocean to the atmosphere due to warming SSTs prior to an El Niño (Fig. S2) and the diffusion term is negligible compared to other terms of the SST budget equation (Fig. S3), both terms are excluded from discussion in this study.

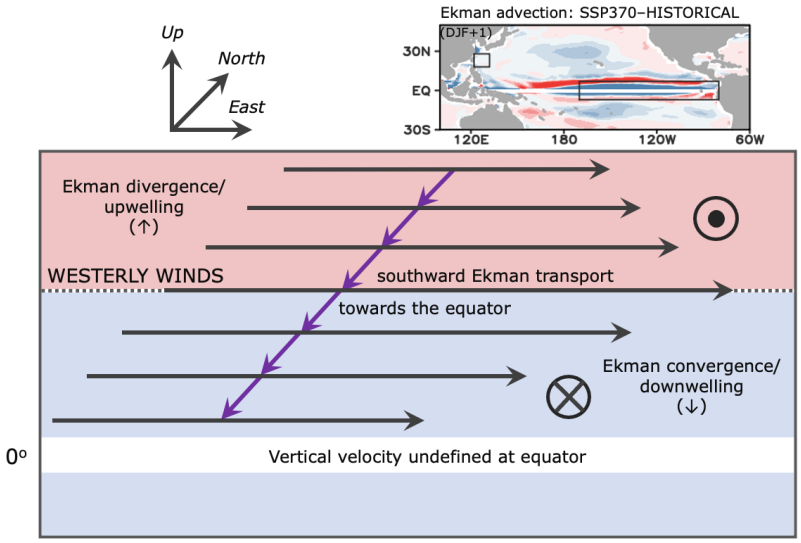

Fig. 9 Schematic diagram showing changes in SSP370 Ekman advection with wind stress curl (modified from Talley et al. 2011). With SSP370 forcing, a strengthened convergent (downwelling) center develops in the central equatorial Pacific and is surrounded by strengthened divergent (upwelling) zones outside the center. Warm water flows towards the convergent center from sites of upwelling anomalies to downwelling anomalies to balance the meridional sea surface height gradient.

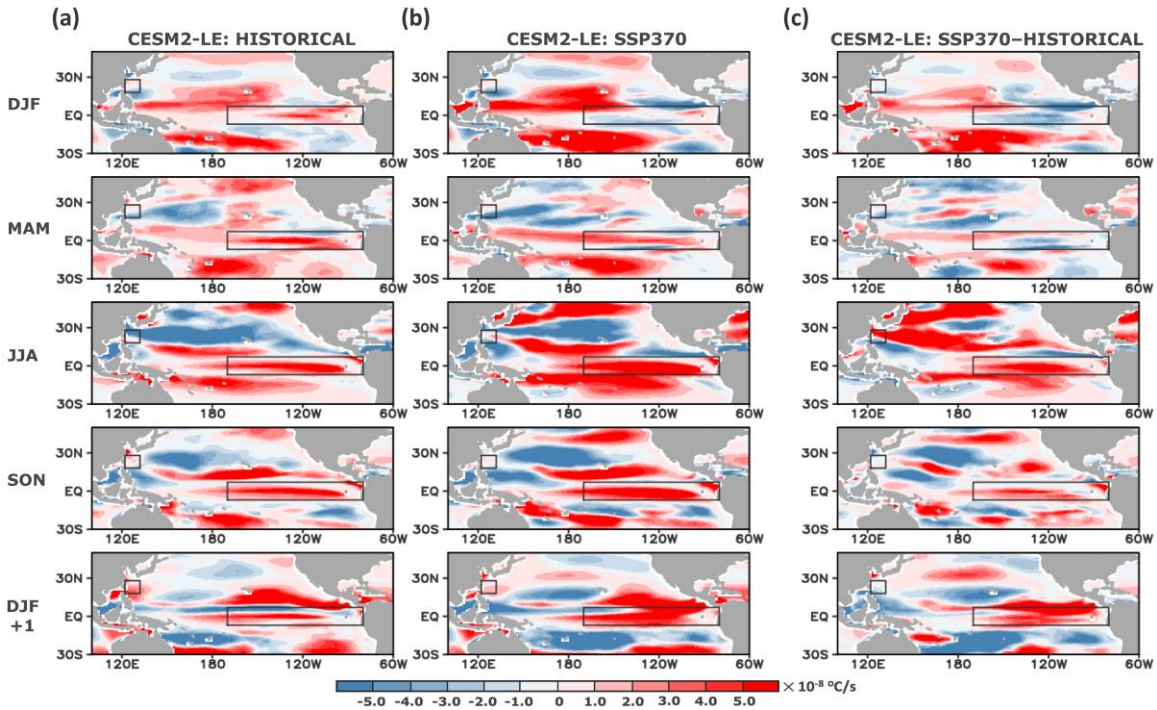

Fig. 10 CESM2-LE entrainment composites of "warm events". Columns represent (a) historical runs, (b) SSP370 runs, and (c) SSP370–historical difference. Rows represent seasonal evolution from the cold WNP (DJF) to the El Niño (DJF+1).

2.5 Discussion

According to the analyses in this chapter, WNP-induced westerly anomalies affect ENSO diversity primarily by zonal advection and thermocline feedback depending on the background states of the tropical precursors (Fig. 11). The increasing amplitude and frequency of the summer westerly anomalies in a warming climate imply stronger and more frequent El Niños with future warming under WNP influence. Intensification of the westerlies induces stronger westerly wind stress and amplifies Kelvin wave activity in the western equatorial Pacific. The net effect is stronger downstream effects related to the Bjerknes feedback to promote an easier transition to an amplified El Niño. Under non-El Niño conditions, the easterly trade winds over the central Pacific maintain the zonal thermocline depth gradient and control the E–W heat distribution in the mixed layer. Downwelling equatorial Kelvin waves can trigger an EP El Niño via positive feedback between the central Pacific zonal winds and eastern Pacific SST anomalies (Kessler et al. 1995; Wang 2015; Li and Federov 2022). As a westerly wind anomaly excites a downwelling Kelvin wave, it weakens the easterlies in the central Pacific and relaxes the thermocline slope. Stronger westerlies may even reverse the direction of winds towards the east. The resultant negative (anticyclonic) wind stress curl anomalies in the central Pacific promote eastward movement of the surface current and warmer SSTs. With global warming, convergence intensifies convection over the central Pacific and strengthens the wind stress curl, which subsequently strengthens advection further towards the eastern Pacific. Below the surface, the amplified wave propagates eastward along the thermocline slope and suppresses it further by displacing more warm water towards the eastern Pacific and facilitating SST increase by entrainment, resulting in a stronger EP El Niño (Figs. 3, 10). However, downwelling equatorial Kelvin waves are also involved in the development of more frequent CP El Niños with enhanced warming. Studies show that the initial zonal mean thermocline state in the tropical Pacific has shifted to a more La Niña-like state since 2000 (Xiang et al. 2013; Mosquera Vasquez et al. 2014). A steeper thermocline slope in the western equatorial Pacific can impede propagation of the wave to the east of 120°W. Early dispersion of the waves in central Pacific

would prevent the Bjerknes feedback from being triggered in the eastern Pacific and confine the maximum positive SST anomalies to the central Pacific. Stronger future background warming in the western equatorial Pacific may also shift the warm pool west of the date line to produce a western Pacific (WP) ENSO as observed in the CMIP6 SST and surface wind anomaly composites (Fig. 2). Eastward propagation of thermocline anomalies under WNP influence with future warming depends on the interplay between amplified Kelvin wave activity and the zonal mean thermocline state.

The strengthening effects of both Ekman and geostrophic heat advection and entrainment of subsurface water in the equatorial Pacific under SSP370 forcing stress on the role of the *relative strength* of zonal advective feedback and thermocline feedback in modulating diversity of WNP-induced El Niños with future warming. Zonal advection and upwelling have been linked to geostrophic balance between zonal geostrophic current and meridional thermocline depth gradient (Jin and An 1999; An and Jin 2001). The stronger westerly wind stress under SSP370 forcing intensifies zonal advection of warm water along the E–W equatorial Pacific while westerly wind stress curl anomalies induce downwelling and upwelling anomalies in the central Pacific which promote meridional advection of warmer water towards the central equatorial Pacific to balance the larger variations in sea surface height and mixed layer depth gradients (Fig. 10). Although zonal advective feedback is the main contributor to the formation and early development of a CP El Niño with enhanced warming, thermocline feedback in the central Pacific is also critical in further development of warmer SSTs. Stronger positive entrainment anomalies in the central–eastern equatorial Pacific with SSP370 forcing can strengthen the positive feedback between the central Pacific zonal winds and eastern Pacific SST anomalies by propagating the maximum thermocline anomalies further east of 150°W during the El Niño (Fig. 10). With future warming, a deeper central–eastern Pacific thermocline resulting from increased entrainment of warmer water into the mixed layer combined with the background state of a charged western Pacific during the initiation phase can produce basin-wide SST anomalies and deep thermocline. These conditions and westerly

anomalies are critical for EP El Niño development and are only simulated by partially coupled experiments when WNP influence is included (Fosu et al. 2020). Without WNP influence, the warm pool is restricted to the central Pacific over a shallow thermocline (Fosu et al. 2020). El Niños that originate in the western Pacific but mature in the eastern Pacific are the strongest El Niños that can be produced and involve both zonal feedback in the central Pacific and thermocline feedback in the eastern Pacific (Wang et al. 2019).

Westerly anomalies and thermocline setting in the tropics combined with extratropical influence have been key factors in contributing to ENSO diversity in recent decades. WWBs may achieve peak magnitudes strong enough to prevail across most of the equatorial Pacific and promote advection of warm water further towards the eastern Pacific. The 1997/98 El Niño is the strongest EP El Niño ever recorded and was characterized by stronger westerly anomalies than the mixed CP-EP El Niño of 2015/16 (Fig. 1b, c). WWBs and warm SSTs extended further east of the dateline by winter 1997/98 compared to winter 2015/16. The maximum thermocline depth in the eastern Pacific during the summer of 1997 was three times lower than the depth in summer 2015 (Lim et al. 2017; Paek et al. 2017). Downwelling anomalies in the eastern Pacific had developed by the summer of 1997 but the 2015/16 El Niño was preceded by upwelling anomalies in the eastern Pacific in the months leading up to the event. The weaker EP dynamics and WWBs of the 2015/16 event compared to 1997/98 event suggest that tropical dynamics alone cannot explain the persistence of the strong central Pacific SST anomaly center of the 2015/16 El Niño. The dominantly CP dynamics associated with the 2015/16 El Niño have been linked to strengthened extratropical forcing that lasted through most of 2015. A negative NPO phase and positive PMM phase in 2015 sustained the warm central Pacific SST anomaly center in the seasons leading up to the El Niño through the WES feedback and Bjerknes feedback (Paek et al. 2017). PMM southwesterlies produce equatorward and easterly Ekman flow that reduce upwelling in the central equatorial Pacific and increase SSTs (Zhang et al. 2009). Stronger SSP370 off-equatorial MAM southwesterly anomalies in the western Pacific (Fig. 3) imply an amplified PMM connection to

WNP and ENSO with future warming that can generate stronger westerly anomalies in the equatorial Pacific when considering the combined effects of both extratropical precursors on the tropical dynamics of ENSO.

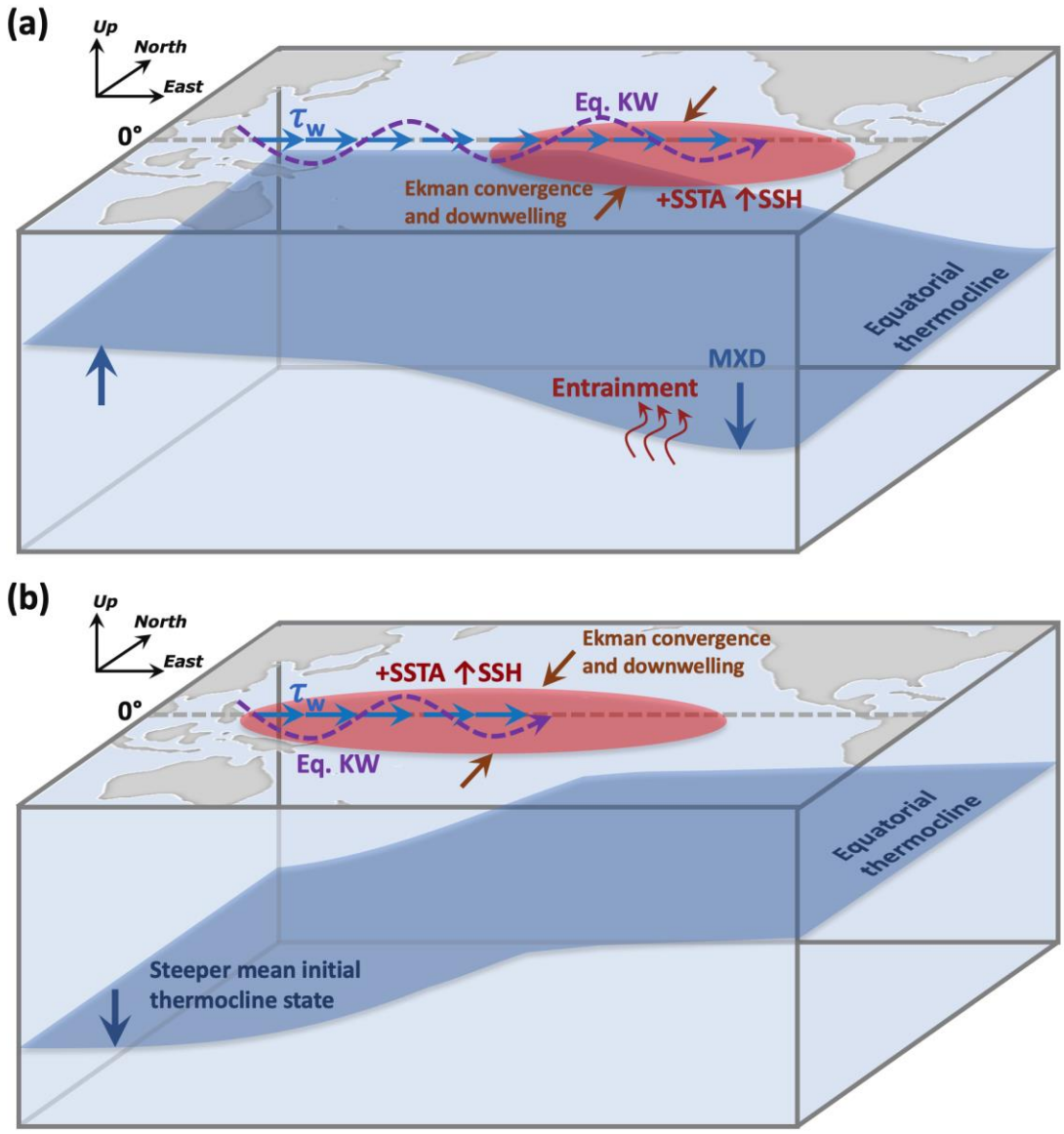

Fig. 11 Under future warming, WNP-induced westerly anomalies affect ENSO diversity primarily by zonal advection and thermocline feedback depending on the background states of the tropical precursors. (a) Stronger westerly wind stress (τ_w) may strengthen advection of warmer water further towards the eastern Pacific and increase sea surface height. Entrainment of thermocline anomalies into the mixed layer increase the mixed layer depth and are favorable for EP El Niños. (b) Weaker τ_w or a steeper mean initial thermocline state can hinder propagation of equatorial Kelvin waves and thermocline anomalies east of the central Pacific and promote either CP El Niños or WP El

Niños. τ_w curl anomalies weaken the easterly trade winds and promote Ekman heat convergence and downwelling in the equatorial Pacific. MXD=mixed layer depth; SSH=sea surface height; Eq. KW=equatorial Kelvin wave.

2.6 Concluding Remarks

In summary, the increase in amplitude and frequency of El Niños preceded by JJA westerly wind events with warming highlight the growing importance of WWBs in the development of El Niños under the warming climate. The summer westerly wind anomalies in the western equatorial Pacific intensify with warming, and the central equatorial Pacific SSTs, surface convergence, and Ekman convergence (geostrophic divergence) become stronger in the seasons prior to a WNP-preceded El Niño, indicating a more pronounced central Pacific focus from the transition to mature phase. Eastward shift of positive entrainment anomalies and increasing sea surface height and mixed layer depth anomalies in the eastern Pacific during the El Niño with future warming are also consistent with stronger advection of warmer water and propagation of thermocline anomalies towards the eastern Pacific. Depending on the relative strength of these two mechanisms and the background state of ENSO precursors, westerly wind stress and the resultant downwelling equatorial Kelvin waves under WNP influence may promote either a CP El Niño or an EP El Niño, or even shift the warm pool west of the dateline to produce a WP El Niño as observed in recent decades. The strength of westerly wind anomalies and the mean initial thermocline state affect both, advection of warm surface water and propagation of subsurface thermocline anomalies by Kelvin waves in the equatorial Pacific. As both WNP and PMM can trigger anomalous westerly advection along the equatorial Pacific, and the amplitude and frequency of ENSO influenced by each extratropical mode are shown to increase with warming, future warming is expected to strengthen the three-way link and promote stronger and more frequent El Niños.

2.7 Supplementary Material

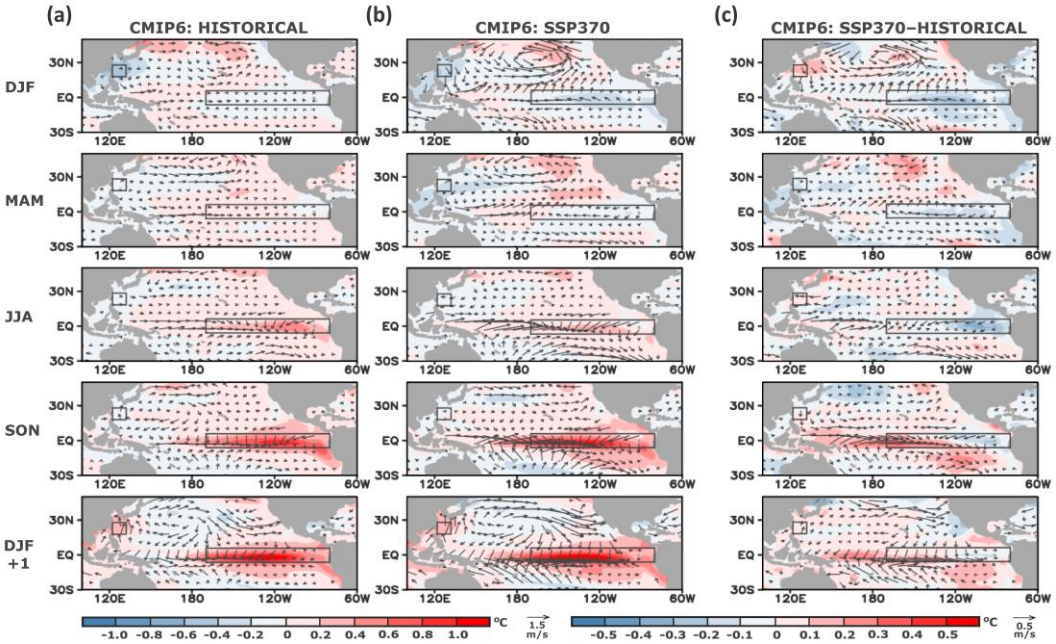

Fig. S1 CMIP6 SST and surface wind anomaly composites of "warm events" using equal (3–5) ensembles for each model. Columns represent (a) historical runs, (b) SSP370 runs, and (c) SSP370–historical difference. Rows represent seasonal evolution from the cold WNP (DJF) to the El Niño (DJF+1). Left scale bar and arrow legend are for (a) and (b). Right scale bar and arrow legend are for (c).

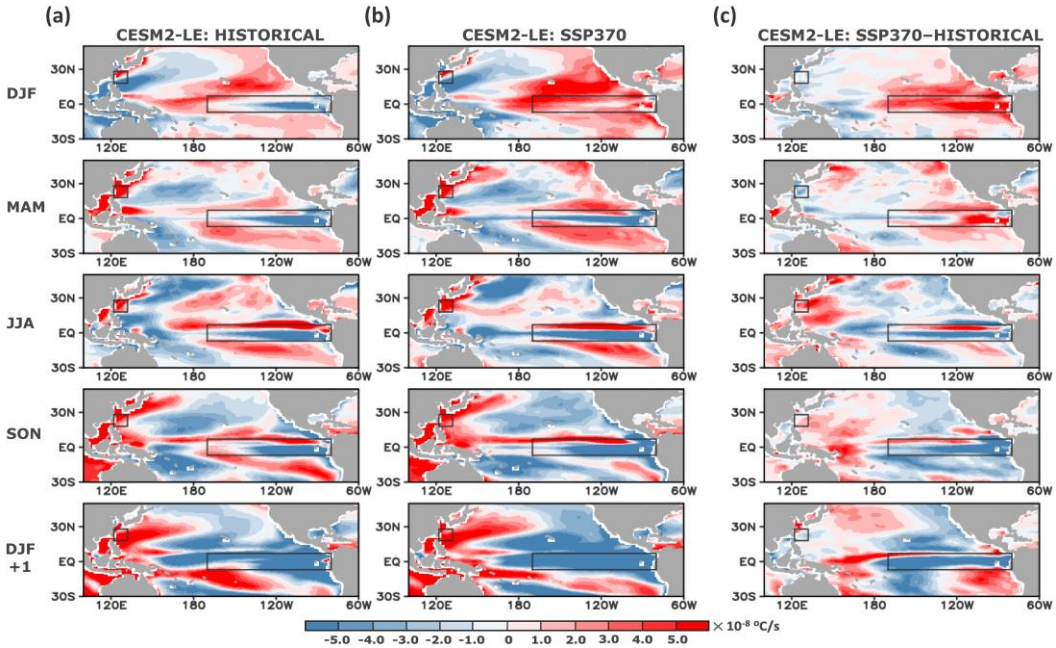

Fig. S2 CESM2-LE air–sea heat flux composites of "warm events". Columns represent (a) historical runs, (b) SSP370 runs, and (c) SSP370–historical difference. Rows represent seasonal evolution from the cold WNP (DJF) to the El Niño (DJF+1).

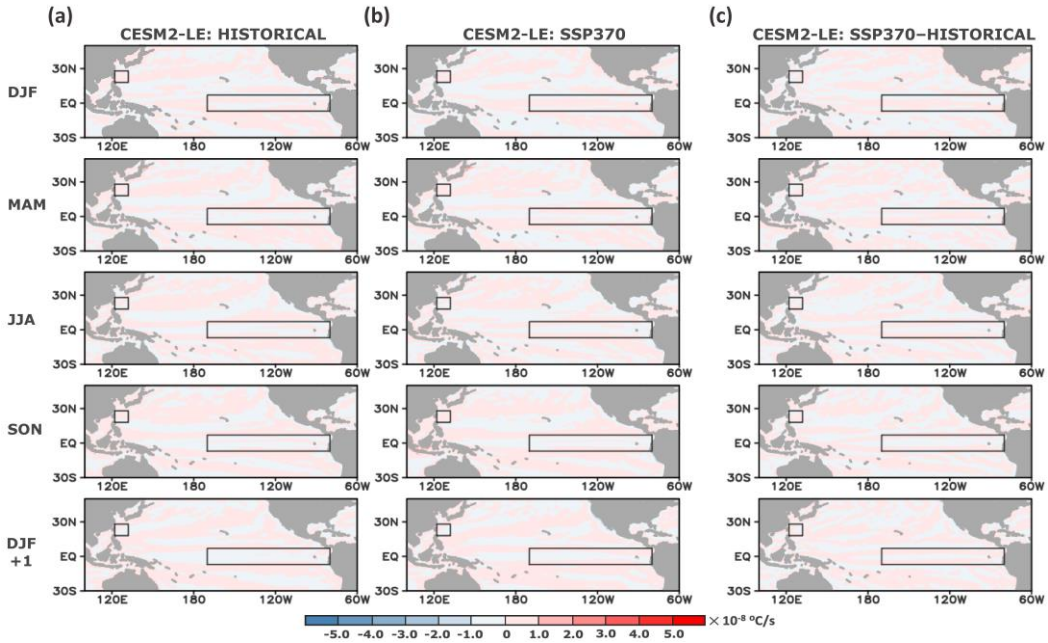

Fig. S3 CESM2-LE diffusion composites of "warm events". Columns represent (a) historical runs, (b) SSP370 runs, and (c) SSP370–historical difference. Rows represent seasonal evolution from the cold WNP (DJF) to the El Niño (DJF+1).

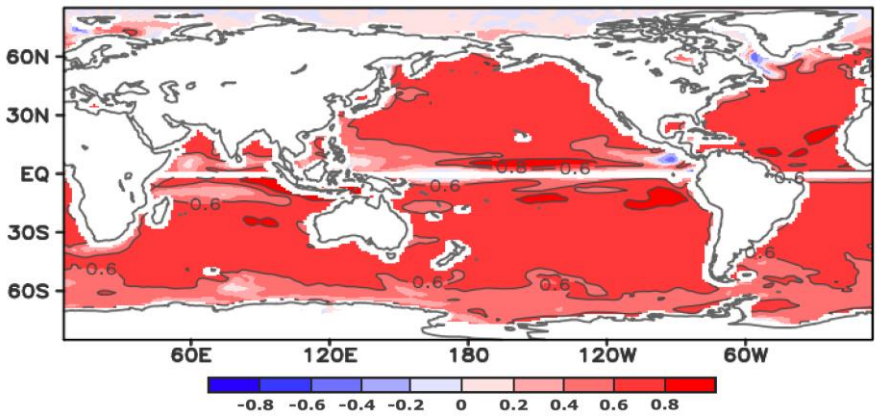

Fig. S4 Average point-to-point correlation of the LHS of the SST budget equation with the RHS averaged from 1970 to 2014 between 50 CESM2 large ensembles using Fisher's Z transformation. The global ensemble mean of 50 ensembles is > 0.6 for most of the oceans.

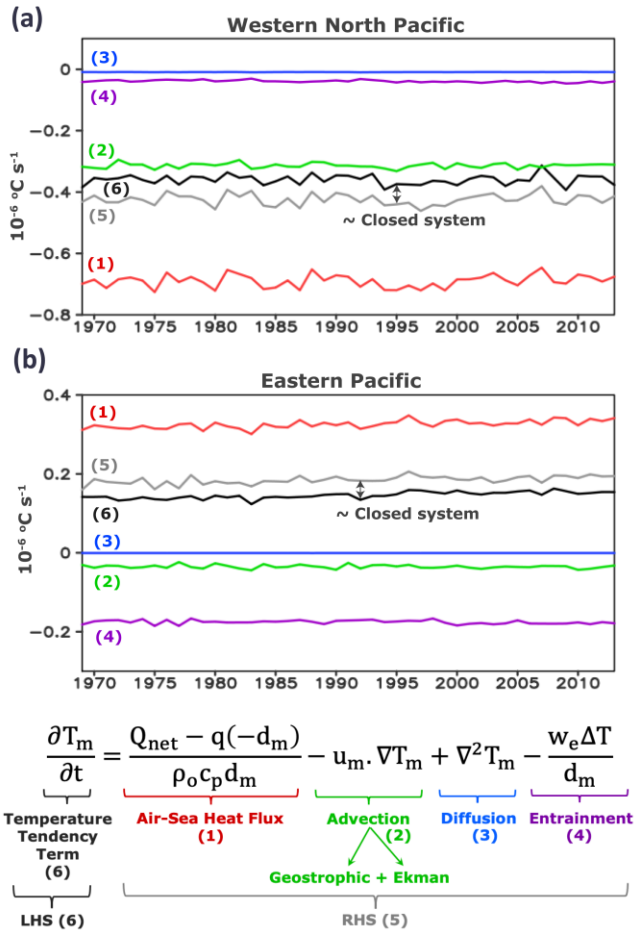

Fig. S5 Temporal evolution of the LHS of the SST budget equation with each term on the RHS and their sum in the (a) western North Pacific and (b) the eastern Pacific regions.

REFERENCES

Alexander MA, Vimont DJ, Chang P, Scott JD (2010) The impact of extratropical atmospheric variability on ENSO: Testing the seasonal footprinting mechanism using coupled model experiments. J Clim 23:2885–2901. https://doi.org/10.1175/2010JCLI3205.1

An S-I, Jin F-F (2001) Collective role of zonal advective and thermocline feedbacks in ENSO mode. J Clim 14:3421–3432. https://doi.org/10.1175/1520-0442(2001)014<3421:CROTAZ>2.0.CO;2

An S-I, Wang B (2000) Interdecadal change of the structure of the ENSO mode and its impact on the ENSO frequency. J Clim 13:2044–2055. https://doi.org/10.1175/1520-0442(2000)013<2044:ICOTSO>2.0.CO;2

Anderson BT, Perez RC, Karspeck A (2013) Triggering of El Niño onset through trade wind–induced charging of the equatorial Pacific. Geophys Res Lett 40:1212–1216. https://doi.org/10.1002/grl.50200

Ashok K, Behera SK, Rao SA, Weng H, Yamagata T (2007) El Niño Modoki and its possible teleconnection. J Geophys Res 112:C11007. https://doi.org/10.1029/2006JC003798

Battisti DS, Hirst AC (1989) Interannual Variability in a Tropical Atmosphere–Ocean Model: Influence of the Basic State, Ocean Geometry and Nonlinearity. J Atmos Sci 46:1687–1712. https://doi.org/10.1175/1520-0469(1989)046<1687:IVIATA>2.0.CO;2

Behringer DW, Ji M, Leetmaa A (1998) An improved coupled model for ENSO prediction and implications for ocean initialization. Part I: The ocean data assimilation system. Mon Wea Rev 126:1013–1021. https://doi.org/10.1175/1520-0493(1998)126<1013:AICMFE>2.0.CO;2

Behringer DW, Xue Y (2004) Evaluation of the global ocean data assimilation system at NCEP: The Pacific Ocean. Eighth Symposium on Integrated Observing and Assimilation Systems for Atmosphere, Oceans, and Land Surface, AMS 84th Annual Meeting, Washington State Convention and Trade Center, Seattle, Washington, 11–15.

Bjerknes J (1966) A possible response of the atmospheric Hadley circulation to equatorial anomalies of ocean temperature. Tellus 18: 820–829. https://doi.org/10.1111/j.2153-3490.1966.tb00303.x

Bjerknes J (1969) Atmospheric teleconnections from the equatorial Pacific. Mon Weather Rev 97:163–172. https://doi.org/10.1175/1520-0493(1969)097%3c0163:atftep%3e2.3.co;2

Bond NA, Overland JE, Spillane M, Stabeno P (2003) Recent shifts in the state of the North Pacific. Geophys Res Lett 30:2183. https://doi.org/10.1029/2003GL018597

Boschat G, Terray P, Masson S (2013) Extratropical forcing of ENSO. Geophys Res Lett 40:1605–1611. https://doi.org/10.1002/grl.50229

Boucher O, Servonnat J, Albright AL et al (2020) Presentation and evaluation of the IPSL-CM6A-LR climate model. J Adv Model Earth Syst 12:e2019MS002010. https://doi.org/10.1029/2019MS002010

Cane MA, Zebiak SE, Dolan SC (1986) Experimental forecasts of El Niño. Nature 321:827–832. https://doi.org/10.1038/321827a0

Capotondi A, Sardeshmukh PD (2015) Optimal precursors of different types of ENSO events. Geophys Res Lett 42:9952–9960. https://doi.org/10.1002/2015GL066171

Chakravorty S, Perez RC, Anderson BT, Giese BS, Larson SM, Pivotti V (2020) Testing the trade wind charging mechanism and its influence on ENSO variability. J Clim 33:7391–7411. https://doi.org/10.1175/JCLI-D-19-0727.1

Chen D, Cane MA, Kaplan A, Zebiak SE, Huang D (2004) Predictability of El Niño over the past 148 years. Nature 428:733–736. https://doi.org/10.1038/nature02439

Chen D, Lian T, Fu C, Cane MA, Tang Y, Murtugudde R, Song X, Wu Q, Zhou L (2015) Strong influence of westerly wind bursts on El Niño diversity. Nature Geosci 8:339–345. https://doi.org/10.1038/ngeo2399

Chen H-C, Tseng Y-H, Hu Z-Z, Ding R (2020) Enhancing the ENSO Predictability beyond the Spring Barrier. Sci Rep 10:984. https://doi.org/10.1038/s41598-020-57853-7

Chen S, Yu B (2020) The seasonal footprinting mechanism in large ensemble simulations of the second generation Canadian earth system model: uncertainty due to internal climate variability. Clim Dyn 55:2523–2541. https://doi.org/10.1007/s00382-020-05396-y

Compo GP, Whitaker JS, Sardeshmukh PD et al (2011) The Twentieth Century Reanalysis Project. Q J R Meteorol Soc 137:1–28. https://doi.org/10.1002/qj.776

Danabasoglu G, Lamarque J-F, Bacmeister J et al (2020) The Community Earth System Model Version 2 (CESM2). J Adv Model Earth Syst 12: e2019MS001916. https://doi.org/10.1029/2019MS001916

Delcroix T, Picaut J (1998) Zonal displacement of the western equatorial Pacific “fresh pool”. J Geophys Res 103(C1):1087–1098. https://doi.org/10.1029/97JC01912

Di Lorenzo E, Cobb KM, Furtado JC, Schneider N, Anderson BT, Bracco A, Alexander MA, Vimont DJ (2010) Central Pacific El Niño and decadal climate change in the North Pacific Ocean. Nature Geosci 3:762–765. https://doi.org/10.1038/ngeo984

Ding R, Li J, Tseng Y-H, Sun C, Guo Y (2015) The Victoria mode in the North Pacific linking extratropical sea level pressure variations to ENSO. J Geophys Res Atmos 120:27–45. https://doi.org/10.1002/2014jd022221

Ding, R., and Coauthors, 2022: Multi-year El Niño events tied to the North Pacific Oscillation. *Nat. Commun.*, **13**, 3871, https://doi.org/10.1038/s41467-022-31516-9

Dong S, Gille ST, Sprintall J (2007) An assessment of the Southern Ocean mixed layer heat budget. J Clim 20:4425–4442. https://doi.org/10.1175/JCLI4259.1

Dong S, Kelly KA (2004) Heat budget in the Gulf Stream Region: the importance of heat storage and advection. J Phys Ocean 34:1214–1231. https://doi.org/10.1175/1520-0485(2004)034<1214:HBITGS>2.0.CO;2

Duan W, Liu X, Zhu K, Mu M (2009) Exploring the initial errors that cause a significant "spring predictability barrier" for El Niño events. J Geophys Res 114:C04022. https://doi.org/10.1029/2008JC004925

Duan W, Wei C (2012) The 'spring predictability barrier' for ENSO predictions and its possible mechanism: Results from a fully coupled model. Int J Climatol 33:1280–1292. https://doi.org/10.1002/joc.3513

Elias S (2021) Changes in Ocean Circulation Patterns. In: Elias S (ed) Threats to the Arctic, 1st edn. Elsevier, pp 27–44. https://doi.org/10.1016/B978-0-12-821555-5.00001-2

Eyring V, Bony S, Meehl GA, Senior CA, Stevens B, Stouffer RJ, Taylor KE (2016) Overview of the Coupled Model Intercomparison Project Phase 6 (CMIP6) experimental design and organization. Geosci Model Dev 9:1937–1958. https://doi.org/10.5194/gmd-9-1937-2016

Fan H, Yang S, Wang C, Wu Y, Zhang G (2022) Strengthening Amplitude and Impact of the Pacific Meridional Mode on ENSO in the Warming Climate Depicted by CMIP6 Models. J Clim 35:5195–5213. https://doi.org/10.1175/JCLI-D-21-0683.1

Fedorov AV, Philander SG (2000) Is El Niño changing?. Science 288:1997–2002. https://doi.org/10.1126/science.288.5473.1997

Fisher RA (1915) Frequency distribution of the values of the correlation coefficient in samples of an indefinitely large population. Biometrika 10:507–521. https://doi.org/10.1093/biomet/10.4.507

Fosu B, He J, Wang S-Y (2020) The influence of wintertime SST variability in the Western North Pacific on ENSO diversity. Clim Dyn 54:3641–3654. https://doi.org/10.1007/s00382-020-05193-7

Graham NE, White WB (1988) The El Niño cycle: A natural oscillator of the Pacific Ocean-atmosphere system. Science 240:1293–1302. https://doi.org/10.1126/science.240.4857.1293

Hajima T, Watanabe M, Yamamoto A et al (2020) Development of the MIROC-ES2L Earth system model and the evaluation of biogeochemical processes and feedbacks. Geosci Model Dev 13:2197–2244. https://doi.org/10.5194/gmd-13-2197-2020

Hu S, Fedorov AV (2019) The extreme El Niño of 2015–2016: the role of westerly and easterly wind bursts, and preconditioning by the failed 2014 event. Clim Dyn 52:7339–7357. https://doi.org/10.1007/s00382-017-3531-2

Huang B, Thorne PW, Banzon VF, Boyer T, Chepurin G, Lawrimore JH, Menne MJ, Smith TM, Vose RS, Zhang H-M (2017) Extended Reconstructed Sea Surface Temperature, Version 5 (ERSSTv5): Upgrades, Validations, and Intercomparisons. J Clim 30:8179–8205. https://doi.org/10.1175/JCLI-D-16-0836.1

Ineson S, Balmaseda MA, Davey MK, Decremer D, Dunstone NJ, Gordon M, Ren H-L, Scaife AA, Weisheimer A (2018) Predicting El Niño in 2014 and 2015. Sci Rep 8:10733. https://doi.org/10.1038/s41598-018-29130-1

Jia F, Cai W, Gan B, Wu L, Di Lorenzo E (2021) Enhanced North Pacific impact on El Niño/Southern Oscillation under greenhouse warming. Nat Clim Chang 11:840–847. https://doi.org/10.1038/s41558-021-01139-x

Jin F-F, An S-I (1999) Thermocline and zonal advective feedbacks within the equatorial ocean recharge oscillator model for ENSO. Geophys Res Lett 26:2989–2992. https://doi.org/10.1029/1999GL002297

Jin FF (1997a) An equatorial ocean recharge paradigm for ENSO. Part I: Conceptual model. J Atmos Sci 54:811–829. https://doi.org/10.1175/1520-0469(1997)054<0811:AEORPF>2.0.CO;2

Jin FF (1997b) An equatorial ocean recharge paradigm for ENSO. Part II: A stripped-down coupled model. J Atmos Sci 54:830–847. https://doi.org/10.1175/1520-0469(1997)054<0830:AEORPF>2.0.CO;2

Kalnay E, Kanamitsu M, Kistler R et al (1996) The NCEP/NCAR 40-year reanalysis project. Bull Amer Meteor Soc 77:437–472. https://doi.org/10.1175/1520-0477(1996)077<0437:TNYRP>2.0.CO;2

Kao H-Y, Yu J-Y (2009) Contrasting eastern-Pacific and central-Pacific types of ENSO. J Clim 22:615–632. https://doi.org/10.1175/2008JCLI2309.1

Kaplan A, Cane MA, Kushnir Y, Clement AC, Blumenthal MB, Rajagopalan B (1998) Analyses of global sea surface temperature 1856–1991. J Geophys Res 103(C9):18567–18589. https://doi.org/10.1029/97jc01736

Karspeck AR, Anderson JL (2007) Experimental implementation of an ensemble adjustment filter for an intermediate ENSO model. J Clim 20:4638–4658. https://doi.org/10.1175/JCLI4245.1

Kelley M, Schmidt GA, Nazarenko LS et al (2020) GISS-E2.1: Configurations and climatology. J Adv Model Earth Syst 12:e2019MS002025. https://doi.org/10.1029/2019MS002025

Kessler WS, McPhaden MJ, Weickmann KM (1995) Forcing of intraseasonal Kelvin waves in the equatorial Pacific. J Geophys Res 100(C6):10613–10631. https://doi.org/10.1029/95JC00382

Larson SM, Kirtman BP (2013) The Pacific Meridional Mode as a trigger for ENSO in a high-resolution coupled model. Geophys Res Lett 40:3189–3194. https://doi.org/10.1002/grl.50571

Larson SM, Kirtman BP (2014) The Pacific meridional mode as an ENSO precursor and predictor in the North American multimodel ensemble. J Clim 27:7018–7032. https://doi.org/10.1175/JCLI-D-14-00055.1

Latif M, Barnett TP, Cane MA, Flügel M, Graham NE, von Storch H, Xu J-S, Zebiak SE (1994) A review of ENSO prediction studies. Clim Dyn 9:167–179. https://doi.org/10.1007/BF00208250

Levine AFZ, McPhaden MJ (2016) How the July 2014 easterly wind burst gave the 2015–2016 El Niño a head start. Geophys Res Lett 43:6503–6510. https://doi.org/10.1002/2016GL069204

Li Z, Fedorov AV (2022) Coupled dynamics of the North Equatorial Countercurrent and Intertropical Convergence Zone with relevance to the double-ITCZ problem. Proc Natl Acad Sci 119(31): e2120309119. https://doi.org/10.1073/pnas.2120309119

Lian T, Chen D, Tang Y (2017) Genesis of the 2014–2016 El Niño events. Sci China Earth Sci 60:1589–1600. https://doi.org/10.1007/s11430-016-8315-5

Lim Y-K, Kovach RM, Pawson S, Vernieres G (2017) The 2015/2016 El Niño Event in Context of the MERRA-2 Reanalysis: A Comparison of the Tropical Pacific with 1982/1983 and 1997/1998. J Clim 30:4819–4842. https://doi.org/10.1175/JCLI-D-16-0800.1

Linkin ME, Nigam S (2008) The North Pacific Oscillation–west Pacific teleconnection pattern: Mature-phase structure and winter impacts. J Clim 21:1979–1997. https://doi.org/10.1175/2007JCLI2048.1

Luo J-J, Masson S, Behera SK, Yamagata T (2008) Extended ENSO predictions using a fully coupled ocean-atmosphere model. J Clim 21:84–93. https://doi.org/10.1175/2007JCLI1412.1

McPhaden MJ (1999) Climate oscillations: Genesis and evolution of the 1997–98 El Niño. Science 283:950–954. https://doi.org/10.1126/science.283.5404.950

McPhaden MJ (2004) Evolution of the 2002/03 El Niño. Bull Amer Meteor Soc 85:677–696. https://doi.org/10.1175/BAMS-85-5-677

Mosquera-Vásquez K, Dewitte B, Illig S (2014) The Central Pacific El Niño intraseasonal Kelvin wave. J Geophys Res Oceans 119:6605–6621. https://doi.org/10.1002/2014JC010044

Mu M, Duan W, Wang B (2007a) Season-dependent dynamics of nonlinear optimal error growth and El Niño-Southern Oscillation predictability in a theoretical model, J Geophys Res 112:D10113. https://doi.org/10.1029/2005JD006981

Mu M, Wang Q, Duan W, Jiang Z (2014) Application of conditional nonlinear optimal perturbation to targeted observation studies of the atmosphere and ocean. J Meteorol Res 28:923–933. https://doi.org/10.1007/s13351-014-4057-8

Mu M, Xu H, Duan W (2007b) A kind of initial errors related to “spring predictability barrier” for El Niño events in Zebiak-Cane model. Geophys Res Lett 34:L03709. https://doi.org/10.1029/2006GL027412

O'Kane TJ, Sandery PA, Monselesan DP, Sakov P, Chamberlain MA, Matear RJ, Collier MA, Squire DT, Stevens L (2019) Coupled Data Assimilation and Ensemble Initialization with

Application to Multiyear ENSO Prediction. J Clim 32:997–1024. https://doi.org/10.1175/JCLI-D-18-0189.1

Paek H, Yu J-Y, Qian C (2017) Why were the 2015/2016 and 1997/1998 extreme El Niños different?. Geophys Res Lett 44:1848–1856. https://doi.org/10.1002/2016GL071515

Pegion K, Alexander M (2013) The seasonal footprinting mechanism in CFSv2: simulation and impact on ENSO prediction. Clim Dyn 41:1671–1683. https://doi.org/10.1007/s00382-013-1887-5

Pegion KV, Selman C (2017) Extratropical Precursors of the El Niño–Southern Oscillation. In: Wang S-YS, Yoon J-H, Funk CC, Gillies RR (eds) Climate Extremes Patterns and Mechanisms, 1st edn. Wiley, New Jersey, pp 301–314. https://doi.org/10.1002/9781119068020.ch18

Picaut J, Ioualalen M, Menkes C, Delcroix T, McPhaden MJ (1996) Mechanism of the zonal displacements of the Pacific warm pool: Implications for ENSO. Science 274:1486–1489. https://doi.org/10.1126/science.274.5292.1486

Picaut J, Masia F, Penhoat Y du (1997) An advective-reflective conceptual model for the oscillatory nature of the ENSO. Science 277:663–666. https://doi.org/10.1126/science.277.5326.663

Pivotti V, Anderson BT, Cherchi A, Bellucci A (2022) North Pacific trade wind precursors to ENSO in the CMIP6 HighResMIP multimodel ensemble. Clim Dyn. https://doi.org/10.1007/s00382-022-06449-0

Rasmusson EM, Carpenter TH (1982) Variations in Tropical Sea Surface Temperature and Wind Associated with the Southern Oscillation/El Niño. Mon Wea Rev 110:354–384. https://doi.org/10.1175/1520-0493(1982)110<0354:VITSST>2.0.CO;2

Rodgers KB, Lee S-S, Rosenbloom N (2021) Ubiquity of human-induced changes in climate variability. Earth Syst Dynam 12:1393–1411. https://doi.org/10.5194/esd-12-1393-2021

Rogers JC (1981) The North Pacific Oscillation. J Climatol 1:39–57. https://doi.org/10.1002/joc.3370010106

Schneider U, Becker A, Finger P, Meyer-Christoffer A, Rudolf B, Ziese M (2011) GPCC Full Data Reanalysis Version 6.0 at 0.5°:Monthly Land-Surface Precipitation from Rain-Gauges built on GTS-based and Historic Data. https://doi.org/10.5676/DWD_GPCC/FD_M_V6_050

Séférian R, Nabat P, Michou M et al (2019) Evaluation of CNRM Earth-System model, CNRM-ESM2-1: role of Earth system processes in present-day and future climate. J Adv Model Earth Syst 11:4182–4227. https://doi.org/10.1029/2019MS001791

Sellar AA, Jones CG, Mulcahy JP et al (2019) UKESM1: Description and evaluation of the U.K. Earth System Model. J Adv Model Earth Syst 11:4513–4558. https://doi.org/10.1029/2019MS001739

Shi L, Ding R (2020) Contributions of tropical–extratropical oceans to the prediction skill of ENSO after 2000. Atmos Oceanic Sci Lett 13:338–345. https://doi.org/10.1080/16742834.2020.1755600

Shi L, Ding R, Hu S, Li J, Tseng Y, Li X (2022) Influence of the North Pacific Victoria mode on the spring persistence barrier of ENSO. J Geophy Res Atmos 127:e2021JD036206. https://doi.org/10.1029/2021JD036206

Slivinski LC, Compo GP, Sardeshmukh PD et al (2021) An Evaluation of the Performance of the Twentieth Century Reanalysis Version 3. J Clim 34:1417–1438. https://doi.org/10.1175/JCLI-D-20-0505.1

Snyder C (1996) Summary of an informal workshop on adaptive observations and FASTEX. Bull Amer Meteor Soc 77:953–961. https://doi.org/10.1175/1520-0477-77.5.953

Stuecker MF (2018) Revisiting the Pacific Meridional Mode. Sci Rep 8:3216. https://doi.org/10.1038/s41598-018-21537-0

Suarez MJ, Schopf PS (1988) A Delayed Action Oscillator for ENSO. J Atmos Sci 45:3283–3287. https://doi.org/10.1175/1520-0469(1988)045<3283:ADAOFE>2.0.CO;2

Swart NC, Cole JNS, Kharin VV et al (2019) The Canadian Earth System Model version 5 (CanESM5.0.3). Geosci Model Dev 12:4823–4873. https://doi.org/10.5194/gmd-12-4823-2019

Talley LD, Pickard GL, Emery WJ, Swift JH (2011) Atlantic Ocean. In: Talley LD et al (eds) Descriptive Physical Oceanography, 6th edn. Academic Press, Massachusetts, pp 245–301. https://doi.org/10.1016/B978-0-7506-4552-2.10009-5

Tatebe H, Ogura T, Nitta T et al (2019) Description and basic evaluation of simulated mean state, internal variability, and climate sensitivity in MIROC6. Geosci Model Dev 12:2727–2765. https://doi.org/10.5194/gmd-12-2727-2019

Tian B, Ren H-L (2022) Diagnosing SST Error Growth during ENSO Developing Phase in the BCC_CSM1.1(m) Prediction System. Adv Atmos Sci 39:427–442. https://doi.org/10.1007/s00376-021-1189-5

Timmermann A, An S-I, Kug J-S et al (2018) El Niño–Southern Oscillation complexity. Nature 559:535–545. https://doi.org/10.1038/s41586-018-0252-6

Torrence C, Webster PJ (1998) The annual cycle of persistence in the El Niño/Southern Oscillation. Q J R Meteorol Soc 124:1985–2004. https://doi.org/10.1002/qj.49712455010

Trenberth KE, Hoar TJ (1996) The 1990–1995 El Niño–Southern Oscillation event: Longest on record. Geophys Res Lett 23:57–60. https://doi.org/10.1029/95GL03602

Vecchi GA, Wittenberg AT (2010) El Niño and our future climate: where do we stand?. WIREs Clim Chg 1:260–270. https://doi.org/10.1002/wcc.33

Vimont DJ, Wallace JM, Battisti DS (2003) The seasonal footprinting mechanism in the Pacific: Implications for ENSO. J Clim 16:2668–2675. https://doi.org/10.1175/1520-0442(2003)016<2668:TSFMIT>2.0.CO;2

Walker GT, Bliss EW (1932) World Weather V. Mem R Meteorol Soc 4:53–84.

Wallace JM, Rasmusson EM, Mitchell TP, Kousky VE, Sarachik ES, von Storch H (1998) On the structure and evolution of ENSO-related climate variability in the tropical Pacific: Lessons from TOGA. J Geophys Res 103(C7):14241–14259. https://doi.org/10.1029/97JC02905

Wang B (2015) Dynamic Meteorology | Kelvin Waves. In North GR, Pyle J, Zhang F (eds) Encyclopedia of Atmospheric Sciences, 2nd edn. Academic Press, Massachusetts, pp 347–352. https://doi.org/10.1016/B978-0-12-382225-3.00191-2

Wang B, Luo X, Yang Y-M, Sun W, Cane MA, Cai W, Yeh S-W, Liu J (2019) Historical change of El Niño properties sheds light on future changes of extreme El Niño. Proc Natl Acad Sci 116:22512–22517. https://doi.org/10.1073/pnas.1911130116

Wang C, Weisberg RH, Virmani JI (1999) Western Pacific interannual variability associated with the El Niño-Southern Oscillation. J Geophys Res 104(C3):5131–5149. https://doi.org/10.1029/1998JC900090

Wang S-Y, Jiang X, Fosu B (2015) Global eastward propagation signals associated with the 4–5-year ENSO cycle. Clim Dyn 44:2825–2837. https://doi.org/10.1007/s00382-014-2422-z

Wang S-Y, L'Heureux M, Chia H-H (2012) ENSO prediction one year in advance using western North Pacific sea surface temperatures. Geophys Res Lett 39:L05702. https://doi.org/10.1029/2012GL050909

Wang S-Y, L'Heureux M, Yoon J-H (2013) Are greenhouse gases changing ENSO precursors in the western North Pacific?. J Clim 26:6309–6322. https://doi.org/10.1175/JCLI-D-12-00360.1

Webster PJ (1995) The annual cycle and the predictability of the tropical coupled ocean-atmosphere system. Meteorl Atmos Phys 56:33–55. https://doi.org/10.1007/BF01022520

Webster PJ (2020) Fundamental Processes. In Webster PJ (ed) Dynamics of the Tropical Atmosphere and Oceans, 1st edn, Wiley-Blackwell, New Jersey, pp 79–104.

Webster PJ, Yang S (1992) Monsoon and ENSO: Selectively interactive systems. Q J R Meteorol Soc 118:877–926. https://doi.org/10.1002/qj.49711850705

Weisberg RH, Wang C (1997) A western Pacific oscillator paradigm for the El Niño-Southern Oscillation. Geophys Res Lett 24:779–782. https://doi.org/10.1029/97GL00689

Wu X, Han G, Zhang S, Liu Z (2016). A study of the impact of parameter optimization on ENSO predictability with an intermediate coupled model. Clim Dyn 46:711–727. https://doi.org/10.1007/s00382-015-2608-z

Xiang B, Wang B, Li T (2013) A new paradigm for the predominance of standing Central Pacific Warming after the late 1990s. Clim Dyn 41:327–340. https://doi.org/10.1007/s00382-012-1427-8

Xie S-P, Philander SGH (1994) A coupled ocean–atmosphere model of relevance to the ITCZ in the eastern Pacific. Tellus 46A:340–350. https://doi.org/10.3402/tellusa.v46i4.15484

Yeh S-W, Kug J-S, Dewitte B, Kwon M-H, Kirtman BP, Jin F-F (2009) El Niño in a changing climate. Nature 461:511–514. https://doi.org/10.1038/nature08316

Yu J-Y, Fang S-W (2018) The distinct contributions of the seasonal footprinting and charged-discharged mechanisms to ENSO complexity. Geophys Res Lett 45:6611–6618. https://doi.org/10.1029/2018GL077664

Yu J-Y, Kao P, Paek H, Hsu H-H, Hung C, Lu M-M, An S-I (2015) Linking emergence of the central Pacific El Niño to the Atlantic multidecadal oscillation. J Clim 28:651–662. https://doi.org/10.1175/JCLI-D-14-00347.1

Yu L, Rienecker MM (1998) Evidence of an extratropical atmospheric influence during the onset of the 1997–98 El Niño. Geophys Res Lett 25:3537–3540. https://doi.org/10.1029/98GL02628

Yu Y, Duan W, Xu H, Mu M (2009) Dynamics of nonlinear error growth and season-dependent predictability of El Niño events in the Zebiak–Cane model. Q J R Meteorol Soc 135:2146–2160. https://doi.org/10.1002/qj.526

Yukimoto S, Kawai H, Koshiro T et al (2019) The Meteorological Research Institute Earth System Model Version 2.0, MRI-ESM2.0: Description and Basic Evaluation of the Physical Component. J Meteor Soc Japan 97:931–965. https://doi.org/10.2151/jmsj.2019-051

Zhang L, Chang P, Ji L (2009) Linking the Pacific meridional mode to ENSO: Coupled model analysis. J Clim 22:3488–3505. https://doi.org/10.1175/2008JCLI2473.1

Zhang Q, Guan Y, Yang H (2008) ENSO amplitude change in observation and coupled models. Adv Atmos Sci 25:361–366. https://doi.org/10.1007/s00376-008-0361-5

Zhang S, Harrison, MJ, Wittenberg AT, Rosati A, Anderson JL, Balaji V (2005) Initialization of an ENSO forecast system using a parallelized ensemble filter. Mon Wea Rev 133:3176–3201. https://doi.org/10.1175/MWR3024.1

Zhou G-Q, Zhu J-S (2009) Impact of subsurface entrainment on ENSO prediction: 1997−98 El Niño. Atmos Oceanic Sci Lett 2:261−266. https://doi.org/10.1080/16742834.2009.11446821

Zhu J-S, Zhou G-Q, Zhang R-H, Sun Z (2011) On the role of oceanic entrainment temperature (Te) in decadal changes of El Niño/Southern Oscillation. Ann Geophys 29:529–540. https://doi.org/10.5194/angeo-29-529-2011

CHAPTER 3

THE 2–3 YEAR PROPAGATION OF SST ANOMALIES FROM THE WESTERN NORTH PACIFIC AND ITS IMPACT ON ENSO PREDICTIONS

3.1 Abstract

Warm and cold sea surface temperature (SST) anomalies propagate from the western North Pacific to the central–eastern equatorial Pacific in 2–3 years and coincide with the development of El Niños and La Niñas, respectively. The analyses in this chapter show that the warm anomaly results from strengthened trade winds that intensify the western boundary current, and subsequently increase the flux of warmer water from the Western Pacific Warm Pool to the western North Pacific. The propagation appears to be related to the asymmetry of the North Pacific Subtropical Gyre as the gyre is punctuated by multiple intervals of geostrophic adjustment over 2–3 years. The slow, broad, and shallow eastern boundary current promotes prolonged propagation across almost the entire width of the basin. This equatorward flow is facilitated by the wind stress curl, Coriolis deflection, and the sea surface height gradient from the subtropics to the tropics. The net southeast movement of the anomaly along the gyre increases the warm water volume in the Western Pacific Warm Pool and intensifies the east–west tropical warm water volume gradients over the course of 3 years, developing westerly anomalies in the western equatorial Pacific in the year leading up to an El Niño. As warm and cold anomalies propagating from the western North Pacific are either at or near geostrophic equilibrium, their persistence may potentially extend El Niño–Southern Oscillation prediction lead times up to 3 years in advance.

3.2 Introduction

El Niño–Southern Oscillation (ENSO) is characterized by interannual variations in the tropical Pacific atmosphere, ocean surface and subsurface (Walker and Bliss 1932; Bjerknes 1966,

1969), with diverse impacts on weather and climate across the globe through atmospheric teleconnection (e.g., Yeh et al. 2018a; Taschetto et al. 2020). ENSO prediction has made great strides following the development of the Cane-Zebiak model used in the forecast of the 1986 El Niño (Cane et al. 1986) and the derivations of various negative feedback modes that helped explained the oscillatory nature of ENSO (e.g., Suarez and Schopf 1988; Picaut et al. 1996, 1997; Jin 1997a, b; Weisberg and Wang 1997). Most other early efforts to improve ENSO prediction focused on tropical dynamics (e.g., Zebiak 1989; McPhaden et al. 1992); however, the progress in recent decades resulted from the observed effects of climate warming. ENSO patterns in the 21st century have diversified from eastern Pacific to central Pacific (Yu and Kao 2007; Kao and Yu 2009) or western Pacific (Wang et al. 2019) events. The sharp decline in forecast skill of post-1990 predictions made through the boreal spring (Webster and Yang 1992; Torrence and Webster 1998; Yu et al. 2009; Duan and Wei 2012) led to the introduction of five major extratropical air–sea interactions in the North Pacific as precursors that develop either during or prior to the spring preceding an ENSO event, and some are associated with the westward migration of ENSO anomalies (e.g., Paek et al. 2017; Tseng et al. 2022). These are the Seasonal Footprinting Mechanism (Vimont et al. 2003a; Alexander et al. 2010), Pacific Meridional Mode (PMM; Zhang et al. 2009; Larson and Birtman 2013, 2014), Trade Wind Charging (Anderson et al. 2013; Chakravorty et al. 2020), Victoria Mode (Bond et al. 2003; Ding et al. 2015) and opposite-signed sea surface temperature (SST) variability in the western North Pacific (WNP; Wang et al. 2012, 2013; Fosu et al. 2020). The integration of extratropical precursors with tropical dynamics in models yield higher prediction skill scores (Boschat et al. 2013; Chen et al. 2020; Shi and Ding 2020; Zhao et al. 2022). With steady improvement in seasonal prediction in other respects, most models now have the potential to predict El Niños and La Niñas up to 6–12 months in advance (Jin et al. 2008; Tippett et al. 2019; Liu et al. 2022).

Despite significant progress in overcoming the spring predictability barrier through extratropical dynamics, challenges in ENSO prediction are far from resolved. Presently, a reliable forecast can be achieved after a warm or cold anomaly becomes evident; however, prediction before or during the transition period is still difficult and restricts lead times to 12 months. Most extratropical precursors proposed to date are linked to the North Pacific Oscillation (NPO; Walker and Bliss 1932), the second leading mode of atmospheric circulation variability in the North Pacific (Rogers 1981; Linkin and Nigam 2008; Yu and Kim 2011; Park et al. 2013). An NPO phase has an inherently short lifespan in the boreal winter that may extend into early spring (Vimont et al. 2003b). During this period, it activates an extratropical precursor that subsequently triggers an El Niño by the following winter (Vimont et al. 2003a; Alexander et al. 2010; Chen and Yu 2020). Although extensive research has been conducted on the role of NPO in driving multiple extratropical precursors, there is no widely accepted theory on the fundamental dynamics that cause the sea level pressure variability characteristic of NPO itself. Prediction at lead times greater than 1 year related to NPO may be explored through its role in generating multi-year El Niños (Kim and Yu 2020, 2022; Ding et al. 2022), but this approach is specific to noncyclic ENSO evolution and does not adequately apply to the dynamics of oscillatory events. NPO-induced precursors mainly impact El Niños and are less effective in the development of La Niñas (Pegion and Selman 2017; Zhao et al. 2022). Another challenge arises from the several indices derived from different methods to define NPO in the literature (Wallace and Gutzler 1981; Wang et al. 2007; Linkin and Nigam 2008; Yu and Kim 2011; Furtado et al. 2012; Park et al. 2013), raising questions regarding which index most accurately represents NPO. Even when a common method is employed to obtain an NPO index, such as utilizing the second empirical orthogonal function of sea level pressure variability, the regions specified for the analyses vary greatly between studies (e.g., Wang et al. 2007; Yu and Kim 2011).

As warming intensifies and the subtropical impacts on ENSO become stronger (Fang and Yu 2020; Jia et al. 2021; Kim and Yu 2021; Fan et al. 2022; Kim et al. 2023), complications arise within 1-year lead forecasts as well. It becomes increasingly important to ascertain the probable location of the maximum SSTA; however, ENSO diversity has proven difficult to simulate in models (Yu and Kim 2010; Ham and Kug 2012; Capotondi et al. 2020). Central Pacific ENSO have different global impacts (Larkin and Harrison 2005; Kim and Kug 2018) and exhibit different dynamics than eastern Pacific ENSO (Kao and Yu 2009; Capotondi et al. 2015). As a result, the key factors and approach considered in predictions and the associated skill vary greatly depending on ENSO diversity. Eastern Pacific ENSO prediction relies on the strength of variations in thermocline feedback that promote peak SSTAs in the eastern Pacific (Dewitte et al. 2012; Karnauskas 2013) while central Pacific ENSO prediction is mostly related to extratropical dynamics (Vimont et al. 2014) and the warm water volume in the east–west equatorial Pacific that indicate suppressed growth of SSTAs in the eastern Pacific (Ashok et al. 2007; Yeh et al. 2014; Ren et al. 2017) – conflicting dynamics that have led to false alarms, unforeseen events, and teleconnection forecast errors (McPhaden 2004, 2015; Shin and Huang 2016; Jong et al. 2018). Some studies suggest that central Pacific ENSO has greater potential predictability than eastern Pacific ENSO due to greater persistence of central Pacific anomalies (Kim et al. 2009), increased frequency of central Pacific events in recent decades (Lee and McPhaden 2010; Wang et al. 2019) and stronger influence of extratropical precursors (Pegion and Selman 2017; Pegion et al. 2020), yet models have better performance predicting eastern Pacific ENSO than central Pacific ENSO (Yang and Jiang 2014; Ren et al. 2016, 2019; Lee et al. 2018). While the frequency of central Pacific El Niños is projected to increase further with climate change (Yeh et al. 2009; Kim and Yu 2012; Shin et al. 2022), models also show that warming will amplify any eastern Pacific El Niños that develop (Cai et al. 2014, 2018; Shin et al. 2022). The predominantly stochastic nature and growing importance of the relative strength of zonal advective feedback vs. thermocline feedback in predicting the peak SSTA location makes ENSO diversity a crucial yet complex element in

seasonal forecasts. However, extending lead times and moving away from the tropics allows for a shift in focus towards the deterministic mechanisms that have the potential to promote ENSO with a stronger head start, regardless of the conditions in the equatorial Pacific that may occur within 1-year lead time, whether they facilitate or prevent growth of SSTAs, or have preferred forms of ENSO diversity.

The dynamics of ENSO oscillators imply that ENSO is self-sustaining to some degree and its long-term thermal memory resides in the upper ocean in various forms. The higher heat capacity and thermal inertia of water compared to the atmosphere or land also allows the upper ocean to store more heat than any other climate subsystem and release heat slowly over months to years, making ocean surface to subsurface conditions pertinent in studying persistence of both warm and cold SSTA. Most of the ocean heat is circulated by large-scale horizonal gyres and meridional overturning cells (Ganachaud and Wunsch 2003; Kuhlbrodt et al. 2007; Buckley and Marshall 2016), with the vast majority of the heat between the tropical and subtropical Pacific Ocean primarily transported by wind-driven gyres confined to the thermocline (Wijffels et al. 1996; Talley 2003; Ferrari and Ferreira 2011). An El Niño is sourced by the Western Pacific Warm Pool (Bjerknes 1966, 1969) that is sustained by convergence from the North and South Pacific Subtropical Gyres (Wyrtki 1973, 1989). While the mean equatorial thermocline is deeper in the western Pacific than in the eastern Pacific, the North Equatorial Countercurrent is a narrow extension of the warm pool at the surface in the eastern Pacific and may initiate Bjerknes feedback in multiple ways. As the trade winds weaken, westerly anomalies can strengthen the eastward flowing geostrophic countercurrent, displace warmer water towards the eastern Pacific and deepen the thermocline (Bjerknes 1966; Delcroix et al. 1992). With enhanced warming, a warmer Western Pacific Warm Pool can also induce a stronger temperature gradient from the western Pacific to the cold tongue in the central–eastern Pacific and strengthen the countercurrent, giving rise to westerly anomalies that further strengthen the positive feedback (Ashafahani et al. 2021). A stronger North

Pacific Subtropical Gyre may generate a stronger countercurrent that drains the warm pool towards the eastern Pacific during an El Niño (Wyrtki 1973, 1989). Since the recharge and discharge of tropical ocean heat during ENSO is linked to Sverdrup transport (Jin 1997a, b) and geostrophic gyres are permanent ocean features, a longer lead thermal predictor of ENSO may be derived from the subtropical gyres as water returns to tropics.

Wang et al. (2015) document a series of recurring warm and cold SSTA propagating from the western North Pacific to the central–eastern equatorial Pacific in approximately 2–3 years, coinciding with development of El Niños and La Niñas, respectively (also depicted in Fig. 1a,b). A warm or cold WNP phase is defined by an SSTA magnitude greater than 0.5°C in the western North Pacific in the boreal winter (Wang et al. 2012). The recurring events date as far back as the late 1800s, but this propagation was likely prevalent long before the instrumental era. The aforementioned major extratropical precursors proposed to date occur within 1 year preceding an ENSO and cannot account for the 2–3-year propagation or persistence of these anomalies.

In this study, we focus on discerning the mechanisms behind the formation of the warm SSTA in the western North Pacific and its unusually prolonged propagation to the tropics prior to an El Niño. We show that the warm WNP SSTA results from a strengthened western boundary current linked to strengthened trade winds. The analyses suggest that the 3-year SSTA propagation is related to the asymmetry of the North Pacific Subtropical Gyre. We explain how the warm SSTA propagates along the southeastern quadrant of the gyre where the flow is slower, shallower, broader, and equatorward compared to the western side. Although this study focuses on the propagation specific to the warm SSTA, we intermittently reapply some dynamics to the cold SSTA to verify plausibility of the hypothesis and highlight its application to oscillatory events. The direction and speed of geostrophic currents from the tropics to the subtropics work in conjunction with the topography of the ocean to redistribute heat and may be used to explain the formation, propagation, and persistence of subtropical SSTAs that have the potential to promote ENSO long after they form.

3.3 Methodology

3.3.1 Data

All observational and model data used in this study are monthly data. Surface wind reanalysis data of 2.5° resolution are from NCEP/NCAR Reanalysis 1 (Kalnay et al. 1996). SST reanalysis data of 2° resolution are from NOAA ERSST Version 5 (Huang et al. 2017). Ocean reanalysis and assimilation data for 8 other variables were acquired from NCEP Global Ocean Data Assimilation System (Behringer at al. 1998; Behringer and Xue 2004). These include sea surface height (SSH), mixed layer depth (MLD), isothermal layer depth (ILD), zonal and meridional currents, vertical velocity, potential temperature, and salinity data of 1/3° horizonal resolution and 40 vertical levels of 10 m resolution in the upper 200 m for multi-level data. The model data used in this study are historical runs for 10 variables, each composed of 50 ensembles of 1° resolution CESM2-LE (Danabasoglu et al. 2020; Rodgers et al. 2021). These include surface temperature, SSH, MLD, solar shortwave heat flux, total surface heat flux including shortwave flux, zonal and meridional wind stress, and 60 vertical-level zonal and meridional ocean currents. The WNP index is defined as the area between 18°N–28°N and 122°E–132°E (Wang et al. 2012). All model data were detrended prior to analyses to focus on the dynamics associated with interannual variability.

3.3.2 Analyses

Warm WNP anomaly composites for multiple variables were constructed from the following warm WNP winters: DJF 1972/73, 1982/83, 1987/88, 1998/99, 2000/01, 2006/07, 2015/16. We also plotted anomaly composites of SST, surface winds, SSH and MLD for 1, 2 and 3 winters following the respective warm WNP years to show the evolution of the warm SSTA and its associated anomalies in the years leading up to El Niño conditions (Fig. 2). To verify that the propagation of both warm and cold SSTA is persistent throughout the 3-year period and is not a wintertime variability, we produced seasonal SSTA composites from the WNP phase in DJF to the

respective ENSO phase in DJF+3 (Figs. S1 and S3). We added seasonal anomaly composites for SSH and MLD from JJA to DJF+1 to identify key features associated with the development of tropical precursors of an El Niño during the initial stages of the warm SSTA propagation (Fig. S2).

The Sverdrup transport equation (e.g., Aoki and Kutsuwada 2008; Gray and Riser 2014) terms were calculated using CESM2-LE data:

$$\underbrace{V_g}_{\text{Geostrophic transport}} = \underbrace{\frac{1}{\rho_o \beta}\left(\frac{\partial \tau_y}{\partial x} - \frac{\partial \tau_x}{\partial y}\right)}_{\text{Sverdrup transport}} + \underbrace{\frac{\tau_x}{\rho_o f}}_{\text{–Ekman transport}} \quad \ldots (1)$$

where ρ_o is the sea water density, τ_x and τ_y are the zonal and meridional wind stress respectively, f is the Coriolis parameter, β is the Rossby parameter.

The mixed layer temperature tendency equation from Dong et al. (2007) in Eq. (2) was used to decompose heat sources in the mixed layer using CESM2-LE data:

$$\underbrace{\frac{\partial T_m}{\partial t}}_{\text{Temperature tendency}} = \underbrace{\frac{Q_{net} - q(-d_m)}{\rho_o c_p d_m}}_{\text{Air–sea heat flux}} - \underbrace{\left(\frac{\tau}{\rho_o f d_m} + \frac{-g\nabla\eta}{f}\right).\nabla T_m}_{\text{Advection (Ekman + geostrophic}} + \underbrace{\kappa\nabla^2 T_m}_{\text{Diffusion}} - \underbrace{\frac{w_e \Delta T}{d_m}}_{\text{Entrainment}} \quad \ldots (2)$$

where T_m is the mixed layer temperature, Q_{net} is the net surface heat flux, d_m is the mixed layer depth, $q(-d_m)$ is the downward radiative heat flux at the bottom of the mixed layer, c_p is the specific heat of sea water at constant pressure, τ includes both zonal and meridional wind stress, η is the sea surface height, g is the acceleration due to gravity, κ is the horizontal eddy diffusivity coefficient, w_e is the entrainment velocity, and ΔT is the temperature difference between the mixed layer and the layer just below.

The entrainment velocity w_e was calculated using the equation below (Qui and Kelly 1993; Luo and Yamagata 2003; Dong and Kelly 2004; Tozuka et al. 2017):

$$w_e = \frac{2m_0 u_*^3}{\alpha g d_m \Delta T} + \left(\frac{2}{\rho_0 c_p d_m \Delta T} \int_{-d_m}^{0} q(z)\, dz \right) - \frac{1}{\rho_0 c_p \Delta T}[Q_{net} + q(-d_m)] - \frac{m_c}{2\rho_0 c_p \Delta T}[|Q_{net}| - Q_{net}] \quad \dots (3)$$

where m_0 and m_c are constant coefficients 0.5 and 0.83 respectively, $u_* = (|\tau|/\rho_0)^{1/2}$ is the frictional velocity, and α is the thermal expansion coefficient. $q(z)$ is the downward radiative heat flux at depth z that can be calculated using the following equation:

$$q(z) = q(0)\left[R \exp\left(\frac{z}{\gamma_1}\right) + (1-R)\exp\left(\frac{z}{\gamma_2}\right)\right] \quad \dots (4)$$

where $q(0)$ is the shortwave radiative flux at the sea surface, R is the separation constant 0.67, and γ_1 and γ_2 are attenuation constants 1 and 17 respectively.

The WNP SST was regressed with each term of Eq. (2) from 3 years before to 5 years after a warm WNP phase.

P-values obtained for the anomaly composites and correlations are greater than 0.05 (not shown). While these values are not statistically significant, they do not necessarily imply that the result is not real or important. P-values indicate the probability that the observed effect occurred by random chance. In complex systems like climate, other factors such as effect size, temporal and spatial scales, persistence of patterns, or the relevance of the finding to broader climatic trends may well overshadow the p-value in terms of importance.

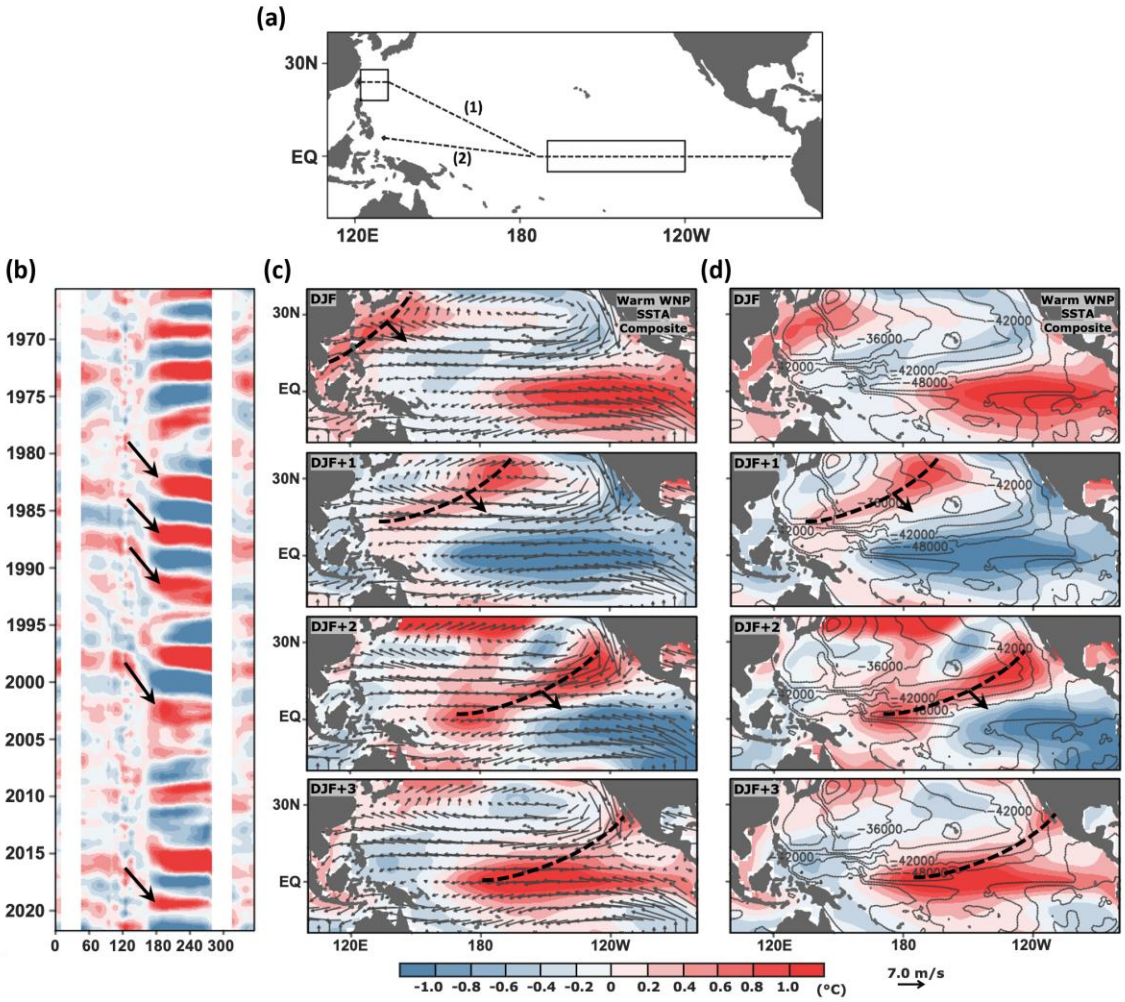

Fig. 1. (a) Latitude selections for longitude-time sections in this study. (b) Longitude-time section of SSTA along path (1) of (a). The SSTA were band-pass filtered within 3–7 years to reflect low-frequency mode of the ENSO cycle. Warm and cold SSTA propagate from the western North Pacific towards the central–eastern equatorial Pacific in 2–3 years and coincide with development El Niños and La Niñas, respectively. Black arrows indicate propagation of the warm SSTA. Top row of columns (c) and (d) is the warm WNP SSTA (°C; shading) composite followed by three consecutive rows of SSTA composites 1, 2 and 3 winters later. The rotational wind (m/s; vectors) climatology in (c) delineates the anticyclonic surface flow in the subtropics. The stream function (m^2/s; contours) climatology of surface currents in (d) delineates the asymmetric gyre circulation centered in the northwest subtropical basin. The dashed black curve in (c) and (d) traces the northeast–southwest orientation of the warm SSTA strip and is parallel to the southeastern quadrant of the gyre throughout the propagation.

3.4 Results

3.4.1 Formation of the warm WNP anomaly: The role of the trade winds

During a warm WNP phase in DJF, the northeasterly trade winds strengthen and generate positive (negative) wind stress curl anomalies in the tropics (subtropics) that intensify divergence (convergence) and upwelling (downwelling; Figs. 2a–c). Anomalous surface divergence between the opposite wind stress curl fields is strongest in the western equatorial Pacific. The SST, SSH and MLD decrease in the Western Pacific Warm Pool as the negative (positive) curl anomalies over the subtropical (tropical) part of the warm pool strengthen the Kuroshio current (North Equatorial Countercurrent) and increase warm water flow towards the western North Pacific (eastern equatorial Pacific). It is important to note that the positive SSTA observed in the eastern Pacific during the warm WNP phase is not associated with an El Niño because trade winds inherently weaken during an El Niño, and the positive SSHA and MLDA detected in the eastern Pacific in DJF are very weak compared to those of an El Niño, as shown in DJF+3. During an El Niño, westerly anomalies in the western equatorial Pacific primarily advect the warm surface water of the Western Pacific Warm Pool to the central–eastern Pacific, capable of substantially increasing the warm water volume to produce considerable sea level rise in presence of gravity and sufficient increase in weight of the warm surface water to depress the thermocline to a greater depth. Conversely, during a warm WNP phase, the diverging warm surface water of the Western Pacific Warm Pool is distributed between the eastern equatorial Pacific and the western North Pacific, giving rise to a smaller increase in warm water volume in the eastern Pacific. While the warm SSTA signal in the eastern Pacific in DJF might be comparable in magnitude to an El Niño, this can be explained by buoyancy differences that sustain the warmer and less dense water at the surface regardless of its volume. However, a greater warm water volume than that supplied by divergence of the Western Pacific Warm Pool during a warm WNP phase is required to further increase the positive SSHA and MLDA (i.e., the vertical extent of the warm surface water) in the eastern Pacific to magnitude characteristic of an El Niño.

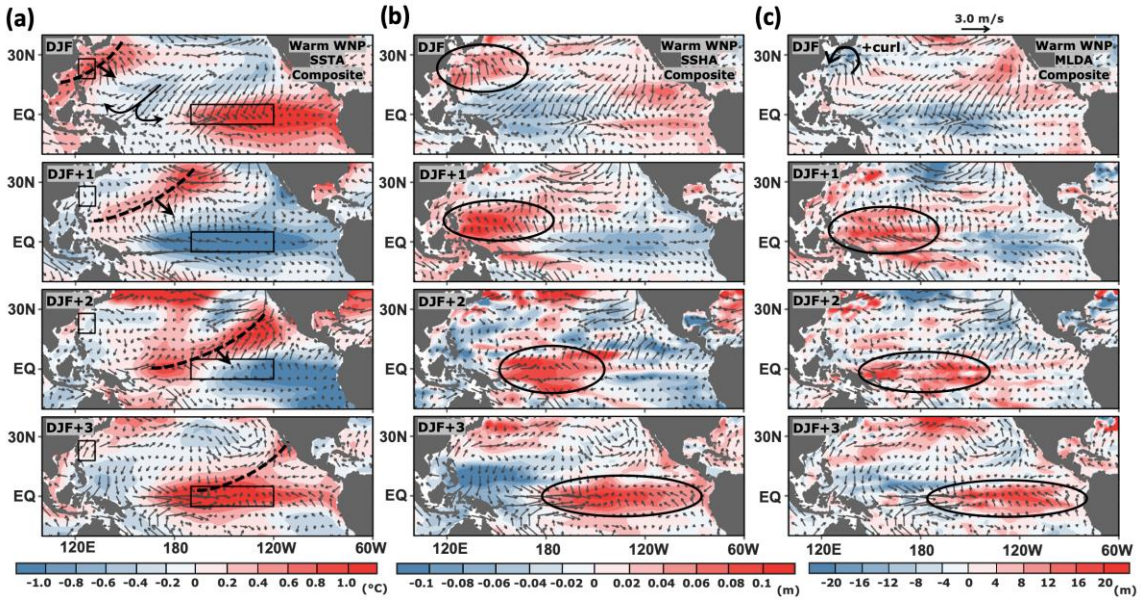

Fig. 2. Top row represents the warm WNP anomaly composites of (a) SST (°C; shading), (b) SSH (m; shading) and (c) MLD (m; shading) and (a–c) surface wind anomalies (m/s; vectors), followed by consecutive rows of the respective anomaly composites 1, 2 and 3 winters later. Black square (rectangle) in (a) defines the WNP (Niño 3.4) index. Positive SSTA in the western North Pacific in DJF is accompanied by positive SSH and wind stress curl anomalies and negative MLDA. From DJF+1 to DJF+3, the warm SSTA strip traced by dashed black curve in (a) propagates from the western North Pacific towards the central–eastern equatorial Pacific while positive SSHA and MLDA (defined by black ellipses in (b) and (c), respectively) propagate with the tropical portion of the warm SSTA from 0°–15°N in the western Pacific to the central–eastern equatorial Pacific.

3.4.2 Evolution of the warm WNP anomaly during propagation

In the western North Pacific, the positive SSTA in DJF is accompanied by positive SSH and wind stress curl anomalies and negative MLDA (Figs. 2a–c). At 30°N, the positive SSTA shifts eastward from DJF to MAM, and then extends southwest from MAM to SON to form a strip, initiating transport of warmer water towards lower latitudes (Fig. S1). From JJA to SON, positive SSHA and MLDA propagate southwest from the subtropical to tropical segment of the SSTA strip (Fig. S2). This decreases the vertical extent of the warm SSTA in the subtropics, while increasing it in the tropics (Fig. S2). However, buoyancy differences maintain the intensity of the warm SSTA in the subtropics (Fig. S1). By DJF+1, the SSTA is separated from the western boundary coastline in the subtropics, and positive SSTA, SSHA and MLDA become discernible in the tropics just north of the western equatorial Pacific, implying a further increase in warm water volume in the

Western Pacific Warm Pool (Figs. 2 and S2). For the remainder of the 3-year period, the warm SSTA continues to reshape by systematically alternating between eastward displacement and southwest extension, progressively strengthening the Western Pacific Warm Pool by DJF+2. From DJF+2 to DJF+3, the positive SSTA, SSHA and MLDA migrate from the Western Pacific Warm Pool to the central–eastern equatorial Pacific and coincide with El Niño development. The warm (cold) SSTA strip in Fig. S1 (Fig. S3) is flanked by a parallel cold (warm) SSTA strip to the east during the earlier part of the propagation when the warm (cold) anomaly is near the coastline, and to the west as the warm (cold) anomaly moves through the interior of the basin. This indicates that any SSTA originating from the western North Pacific propagate in a similar pattern.

3.4.3 Surface winds and surface currents in the subtropical Pacific

The evolution of the SSTA, SSHA and MLDA in Figs. 2a–c can be traced to gyre circulation patterns. The negative curl between the trade winds and mid-latitude westerlies drives the symmetric anticyclonic winds over the subtropical North Pacific (Fig. 1c). The surface current flow of the North Pacific Subtropical Gyre between 10°N and 35°N (Fig. 1d) is consistent with the surface wind rotation, with the exception that the gyre is asymmetric both zonally and meridionally. Western intensification due to the Coriolis parameter increasing with latitude skews the gyre center to the west of the ocean basin (Stommel 1948). The further north the water moves along the western boundary, the stronger the deflection to the right, which generates the most intense rotational flow to the northwest. The western North Pacific center has the maximum SSH between the tropical and subtropical North Pacific (Fig. 3) as a result of Ekman convergence. Water flowing downslope in any direction will be deflected to the right to sustain the rotational flow. The anticyclonic curl gives rise to the eastward-flowing Subtropical Countercurrent from the convergent center. Water spreading outward from the raised center to the east flows a short distance downslope along the Kuroshio extension before it is deflected to the southwest. The further east of the center the water reaches, the slower the gyre speeds, and therefore the weaker the southwest deflection, even with

constant Coriolis parameter along the latitude. This contributes to the widely spaced eastern boundary current that spans the entire width of the subtropical North Pacific basin east of 140°E (Fig. 1d). During a warm WNP phase, the warm SSTA develops along the west and center of the gyre (Figs. 1d). During propagation, the warm SSTA strip drifts along the southeastern part of the gyre and is oriented parallel to the stream function contours in the northeast–southwest direction (Figs. 1d).

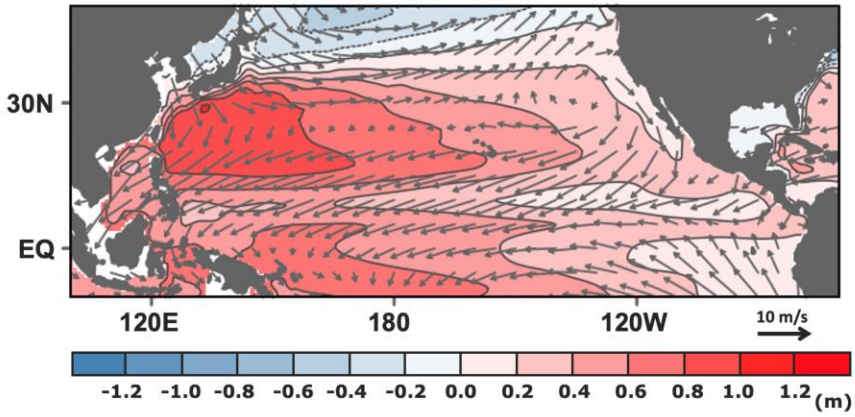

Fig. 3. SSH (relative to geoid) and surface wind climatology. SSH slopes down from the western North Pacific to the central–eastern equatorial Pacific and from the western equatorial Pacific to the central–eastern equatorial Pacific.

3.4.4 The western boundary current during the warm WNP phase

The surface current anomalies in Fig. 4a are consistent with the surface wind anomalies during the warm WNP phase in Fig. 2. The westward current anomalies at 15°N are 45 degrees to the right of the strengthened trade winds (Fig. 4a). Northward or northwestward currents indicating intensification of the Kuroshio current develop along the east coast of the Philippines (Fig. 4a) and slope to greater depths from 10°N to 25°N (Fig. 4c). However, increased speeds along the western boundary strengthen coastal friction and promote positive curl anomalies that make the northward signal less clear near the surface between 20°N and 30°N (Fig. 4c). Downwelling in the subtropics at greater depths is stronger during the warm WNP phase due to strengthened convergence of the western boundary current, but this signal is also weaker at the surface due to divergence and

upwelling anomalies associated with a positive curl (Fig. 4c). These conflicting impacts of a stronger western boundary current explain why a negative MLDA is observed in the western North Pacific (Fig. 2c) despite positive SSTA and SSHA (Fig. 2a,b) from increased warm water flux.

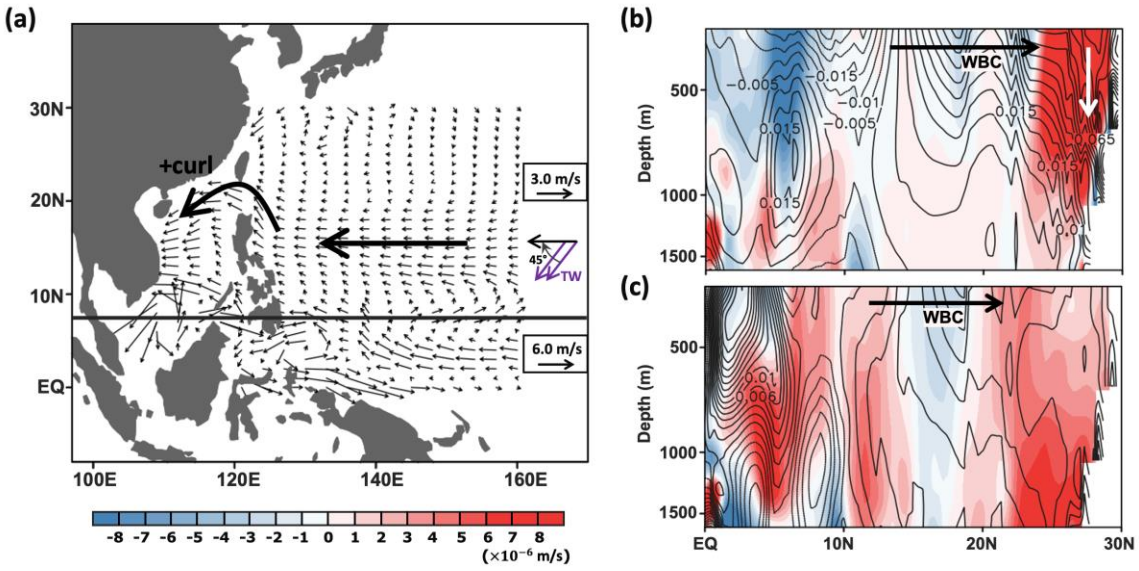

Fig. 4. (a) Warm WNP (DJF) anomaly composite of surface currents (m/s). The vectors are scaled differently north and south of 8°N (solid horizontal black line) as the surface currents are much stronger in the tropics compared to the subtropics. Westward current anomalies at 15°N are 45 degrees to the trade wind (TW) anomalies in DJF of Fig. 2a. Northward current anomalies (positive curl anomalies) form just east (north) of the Philippines. (b) Climatology of meridional currents (m/s; contours) and vertical velocity (m/s; shading) averaged between 122°E and 132°E. The northward currents extend to great depths (>1500 m) characteristic of western boundary currents (WBC). Strong downwelling (white arrow) occurs in the subtropics. (c) Same as (b) except for warm WNP (DJF) anomaly composite. The western boundary current is stronger during the warm WNP phase.

3.4.5 Surface to subsurface profile in the western North Pacific during the warm WNP phase

The strengthened convergence of the western boundary current is critical in the formation (build up) of the warm WNP SSTA (SSHA), but it is the strengthened divergence that preserves the SSTA after formation by controlling vertical processes in the western North Pacific. The MLD represents the base of the ocean mixed layer. Above the MLD, turbulent mixing of surface water evens out the temperature and salinity gradients to yield water of uniform density. Below the MLD, mixing is restricted, and density increases with depth. In contrast, the ILD represents the top of the

thermocline, below which temperature decreases rapidly with depth, but the direction of salinity change can vary. When salinity stratification takes place, a barrier layer thickness separates the ILD and the MLD. During the warm WNP phase, fluctuations in MLDA and ILDA between the equator and 17°N show that variations of the two variables differ in both magnitude and direction of change, and the anomalies vary by less than 5 m (Figs. 5a–d). However, in the subtropics, the anomalies of both variables are strictly negative and of equal magnitudes that increase with latitude by up to 20 m at 30°N (Fig. 5d). This suggests that shoaling of the MLD and the thermocline in the subtropics are likely the result of the same process – strengthened coastal friction in the western North Pacific. The barrier layer thickness remains constant even as it shoals during upwelling and retains heat in the mixed layer by inhibiting mixing with colder water below. Negative salinity and positive potential temperature anomalies occur near the surface between 15°N and 30°N during the warm WNP phase (Figs. 6a–c). These anomalies decrease with depth and disappear at the ILD (Figs. 6a,b). The climatological potential temperature below the ILD decreases with ocean depth due to increasing density (Fig. 6c). While salinity typically increases with depth, a salinity inversion exists below the ILD in the western North Pacific (Fig. 6c). Thermocline salinity inversions are common in many upwelling systems and also inhibit vertical mixing in the thermocline (e.g., Armstrong et al. 1987; Brandt et al. 2015; Thomsen et al. 2016; Burchard et al. 2017). A decreasing potential temperature with depth below the ILD in presence of lower salinity is likely due to stronger cooling in the thermocline from upwelling that keeps vertical density differences large enough to maintain stability despite a salinity inversion. Introduction of warmer and fresher water during the warm WNP phase through lateral surficial processes further strengthens vertical stratification from the surface to subsurface in the western North Pacific.

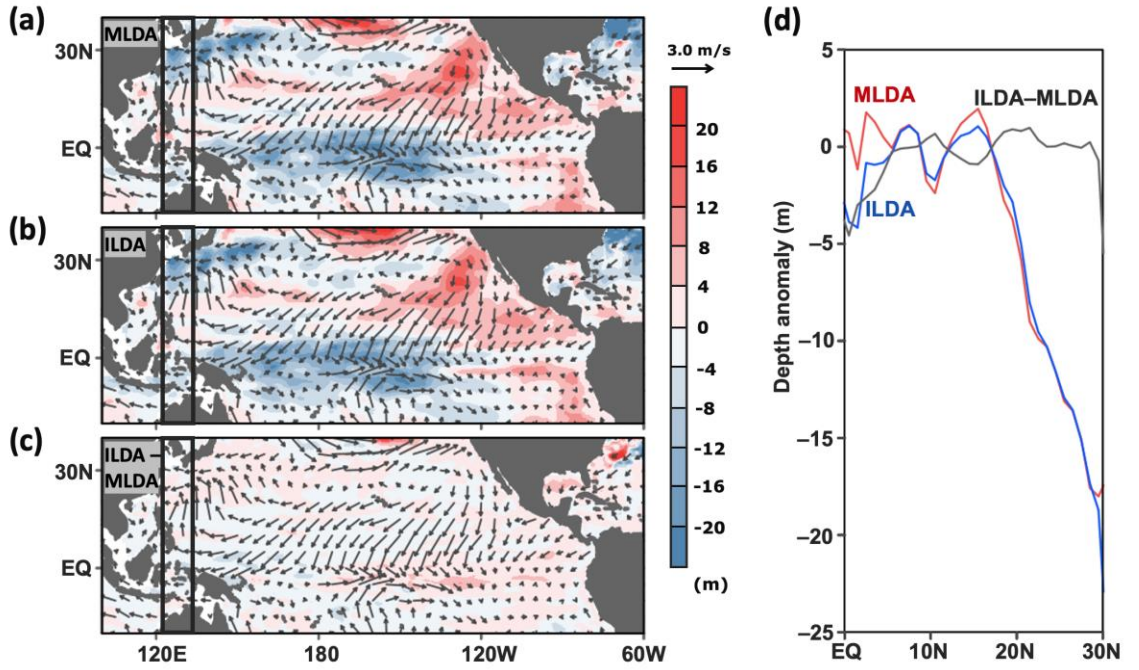

Fig. 5. Warm WNP (DJF) anomaly composites of (a) MLD (m; shading) and (b) ILD (m; shading) and (c) ILD–MLD (m; shading) overlaid by surface wind anomalies (m/s; vectors). Negative MLDA and ILDA in the western North Pacific in (a) and (b) indicate shoaling of both variables. (d) MLDA, ILDA and ILDA–MLDA zonally averaged between 122°E and 132°E as outlined in (a–c). MLD and ILD in the subtropics during the warm WNP phase shoal by equal magnitudes that increase with latitude.

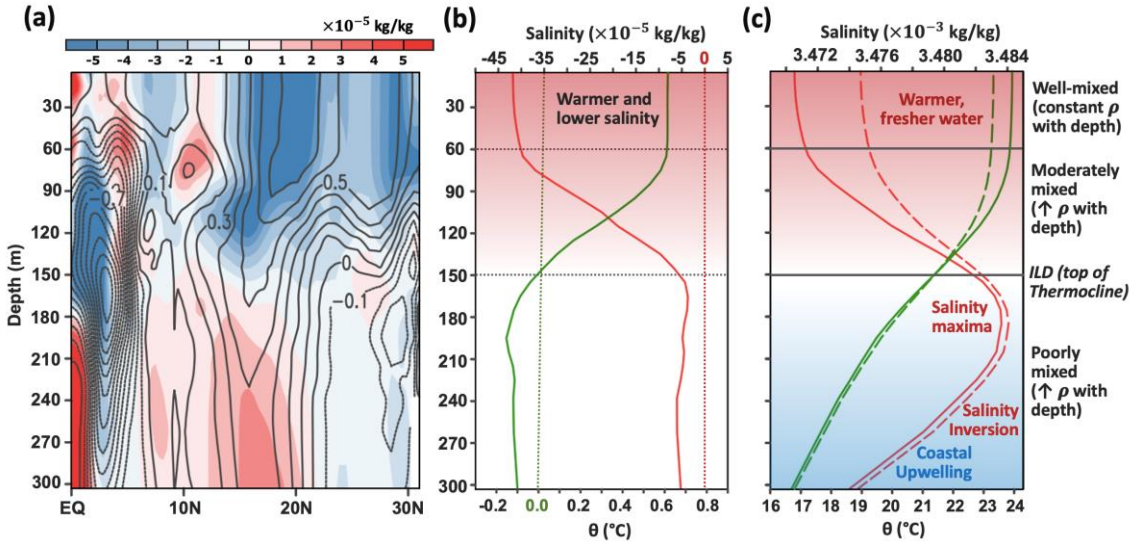

Fig. 6. (a) Vertical profiles of warm WNP (DJF) anomaly composites of potential temperature (θ; °C; contours) and salinity (kg/kg; shading) averaged between 122°E and 132°E. (b) Same as (a) except averaged using the WNP index (18°N–28°N and 122°E–132°E). (c) Same as (a) except averaged using the WNP index for climatology (dashed curves) and the warm WNP phase (solid

curves) to show the background state of the vertical structure. The solid curves minus dashed curves in (c) yield the respective anomalies in (b). The red and green curves in both (b) and (c) represent salinity and potential temperature, respectively. Negative salinity and positive potential temperature anomalies form at the surface in the western North Pacific during the warm WNP phase.

3.4.6. Surface to subsurface transport in the subtropics and tropics

I further decomposed the horizontal transport between the tropical and subtropical Pacific Ocean in Fig. 7. At the surface in the tropics, Ekman transport is driven by wind stress-induced friction and the Coriolis effect which promotes divergence and upwelling. The net water transport is orthogonal to the surface wind direction, which promotes convergence and downwelling in the subtropics. Geostrophic flow is achieved when the pressure gradient force in response to the SSH gradient from the subtropics to tropics is balanced by the Coriolis force. During short intervals of geostrophic adjustment, inertial effects become more important than the rotational effects, resulting in incremental displacement from equilibrium. Geostrophic transport is also a subsurface response to Ekman transport. Upwelling (downwelling) and divergence (convergence) in the Ekman layer at the surface in the tropics (subtropics) promotes convergence (divergence) in the geostrophic layer in the subsurface in the tropics (subtropics) to replace (reduce) the surface outflow (inflow). As a result, geostrophic flow can transport heat through the subsurface (Figs. 7f,h), from the subtropics towards just north of the western equatorial Pacific by a negative curl, followed by a positive curl in the tropics that redirects the water to the central–eastern equatorial Pacific (Figs. 8). The net effect of Ekman and geostrophic transport and therefore net meridional transport driven by wind stress curl is provided by Sverdrup transport (Fig. 7b). Sverdrup transport is negligible at the equator because the surface divergence in the Ekman layer (Fig. 7e) is nearly balanced by subsurface convergence in the geostrophic layer (Fig. 7g). It is most negative (positive) in the subtropics (tropics) with the highest volume flow rate towards the tropics (subtropics) initiating at the Kuroshio extension (10°N; Fig. 7b). The zonal wind stress curl at 30°N is a much stronger driver of southward flow than the meridional wind stress curl (Figs. 7c,d). This emphasizes the significance of eastward flow along the Kuroshio extension in promoting equatorward Sverdrup

transport. The Subtropical Countercurrent slopes down to the north towards downwelling regions under the convergent zone. It may facilitate southward flow from the Kuroshio extension towards the tropics, both at the surface by southward deflection and through the subsurface by divergence in the subtropical geostrophic layer (Fig. 8).

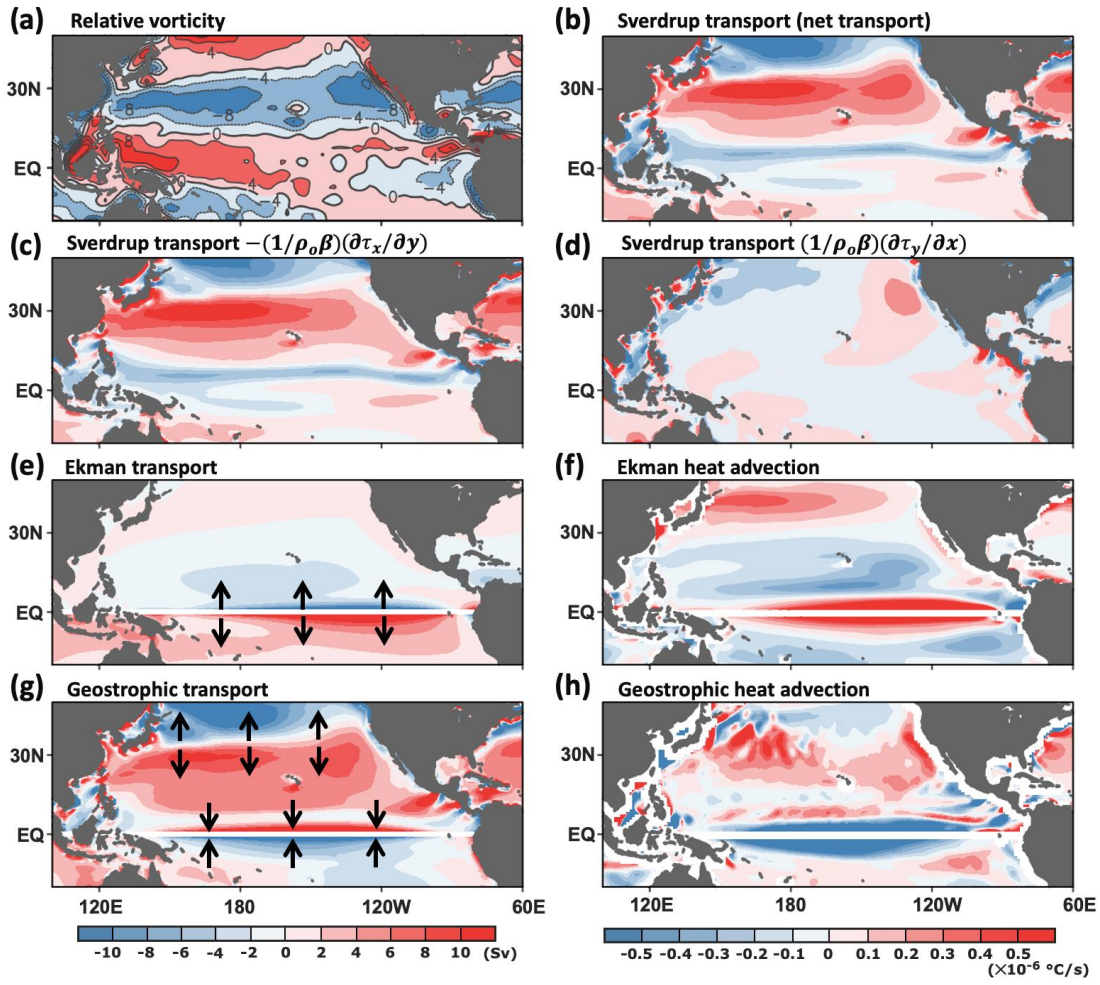

Fig. 7. Climatology of (a) relative vorticity ($\times 10^{-6}s^{-1}$) of surface winds, (b) Sverdrup transport (net transport), (c) zonal and (d) meridional wind stress curl components of Sverdrup transport, (e) Ekman transport, (f) Ekman heat advection, (g) geostrophic transport, and (h) geostrophic heat advection. Positive (negative) shaded values in (a) indicate positive (negative) curl. Positive (negative) values in (b–e) and (g) indicate southward (northward) volume transport. Positive (negative) values in (f) and (h) indicate heat lost (gained) by divergence (convergence). Arrows indicate contribution of each term towards (e) mass and (g) heat divergence or convergence between the tropics and subtropics. Left scale bar is for (b–e) and (g). Right scale bar is for (f) and (h).

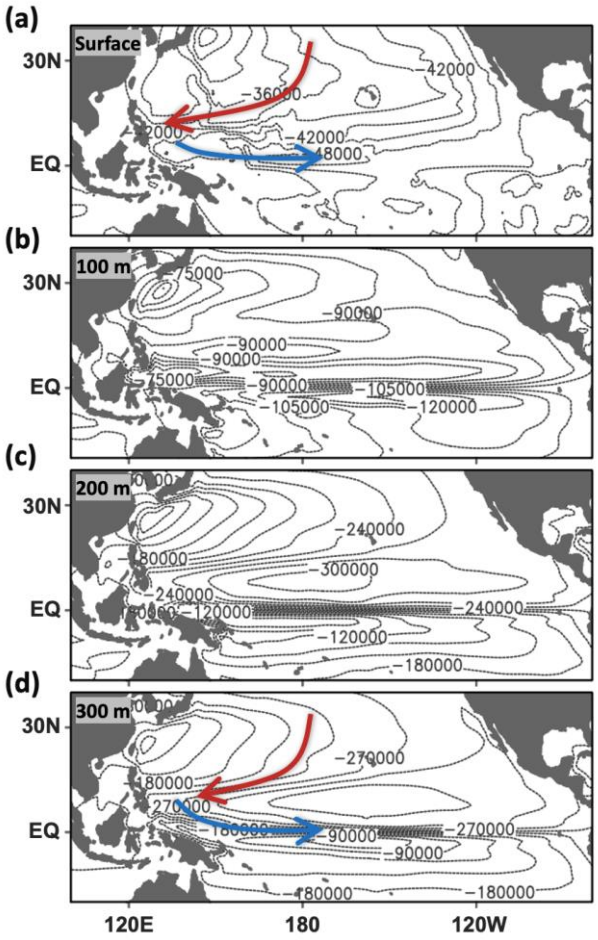

Fig. 8. Stream function (m^2/s) climatology of currents at (a) the surface (b) 100 m, (c) 200 m, and (d) 300 m. The flow is consistent with depth in the western Pacific. Surface to subsurface equatorward transport is promoted by a negative curl from the subtropics to the western tropical Pacific (red arrow; southwest flow), followed by a positive curl towards the central–eastern equatorial Pacific (blue arrow; southeast flow).

3.4.7 Lead-lag correlations of warm WNP SSTA with surface and subsurface anomalies

Lead-lag correlations of warm WNP SSTA with various anomalies reveal persistent features that propagate with both warm and cold SSTA during the equatorward transport (Figs. 9a–c and 10a,b). Positive correlations of SSTA and zonal current and negative correlations of meridional current in the western North Pacific propagate southeast from Y+0 and reach the central–eastern equatorial Pacific by Y+3. Similar 3-year propagation is associated with the negative SSTA correlations (e.g., from Y–2 to Y+1, or Y+2 to Y+5). Any eastward (westward) displacement (Fig. 9a) of the positive (negative) SSTA is accompanied by southward (northward) deflection (Fig. 9b). Negative (positive) relative vorticity anomaly correlations propagate with the positive (negative) SSTA patterns and increase magnitudes towards lower latitudes (Fig. 9c). The contribution of relative vorticity to the absolute vorticity increases with decreasing latitude because planetary vorticity becomes weaker. Positive SSHA (MLDA) correlations begin adjacent to (15 degrees east of) the coastline in the western North Pacific at Y+0 (Fig. 10a) and propagate with the positive SSTA correlations in the next 3 years (Figs. 9a–c). Although a negative MLDA signal is observed in the western North Pacific during a warm WNP phase, the sign becomes positive with offshore movement (Figs. 2c and 10a). Further east of coastal upwelling, the MLDAs reflect the strengthened convergence and downwelling of an intensified western boundary current. Positive SSHA and MLDA correlations at Y+1 shift from 130°E just north of the equator to the central–eastern equatorial Pacific by Y+3 (Fig. 10b). Negative SSHA and MLDA correlations propagate with the negative SSTA signals, and parallel to the positive SSHA and MLDA correlations (Figs. 9a–c and 10a,b).

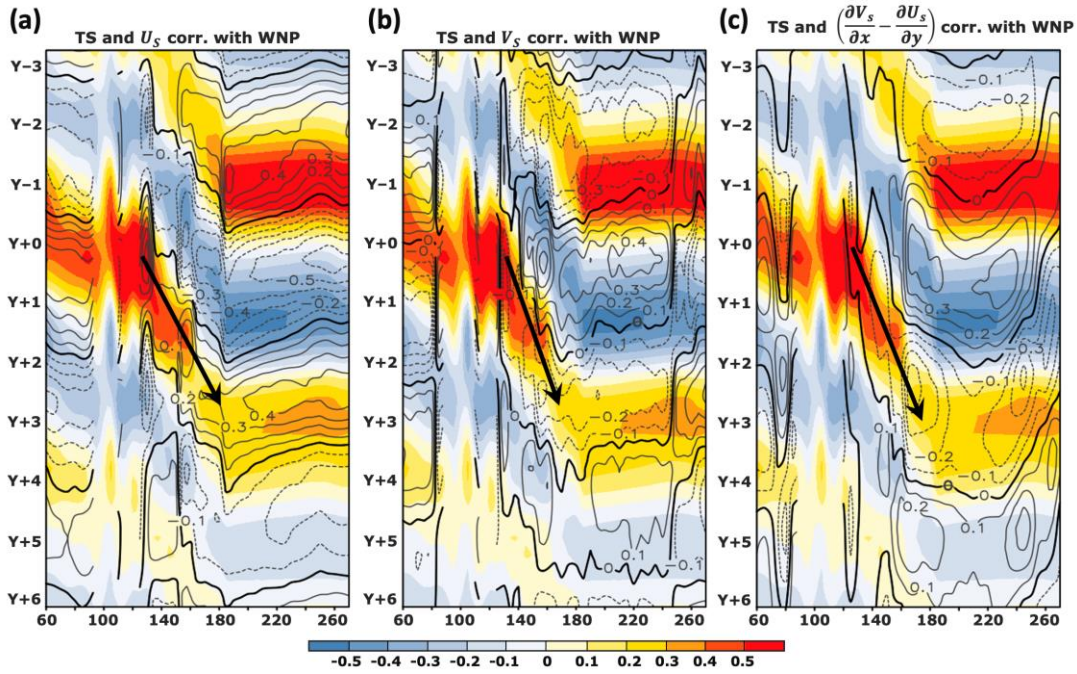

Fig. 9. Longitude-time sections of warm WNP SSTA at Y+0 correlated with anomalies of (a) zonal surface currents (contours), (b) meridional surface currents (contours), (c) relative vorticity (contours) of the surface currents, and (a–c) surface temperature (shading). (a–c) Latitude varies with longitude according to path (1) of Fig. 1a. Y-axes indicate the year relative to the warm WNP phase. Positive (negative) SSTA correlations propagate from the western North Pacific from Y+0 (Y–2; Y+2) towards the central–eastern equatorial Pacific by Y+3 (Y+1; Y+5). Black arrows indicate propagation associated with the positive SSTA correlations. Positive (negative) current correlations in (a) are synchronous with negative (positive) current correlations in (b). (c) Negative (positive) relative vorticity correlations propagate with the positive (negative) SSTA correlations and increase in magnitude towards lower latitudes.

3.4.8 Lead-lag regressions of warm WNP SSTA with the mixed layer temperature tendency terms

WNP SSTs can also be linked to ENSO through recharge and discharge of tropical Pacific Ocean heat oscillating at interannual timescales. Lead-lag regression coefficients in the central–eastern equatorial Pacific (160°E – 260°E) at Y+3 (Fig. 11) coincide with the arrival of the positive SSTA, SSHA and MLDA signals (Figs. 9 and 10) and can be compared to El Niño-like conditions. Weakening of trade winds during an El Niño reduces the positive curl in the tropics. The negative coefficients at Y+3 in Fig. 11b indicate weaker equatorial Ekman heat divergence and upwelling. The subsurface response to weaker upwelling is strengthened heat divergence (or reduced convergence) in the geostrophic layer and yield positive coefficients at Y+3 in Fig. 11a. Positive (negative) entrainment indicate heat flux from the water below (mixed layer) into the mixed layer

(water below). As thermocline anomalies typically propagate eastward along the equatorial Pacific during an El Niño, the positive regression coefficients at Y+3 in Fig. 11c indicate stronger entrainment of subsurface water in the central–eastern Pacific. The negative coefficients at Y+3 in Fig. 11f result from a net SST decrease following the mature phase of an El Niño (Fig. 8). As the air–sea heat flux is simply a response to ENSO SSTAs and diffusion is usually negligible, Figs. 11d,e are omitted from further discussion. However, the central–eastern equatorial Pacific regression coefficients for all the terms related to other El Niños (e.g., at Y–1) are same-signed as those at Y+3. The signs are reversed for events coinciding with La Niñas at Y–3, Y+1 and Y+5. This cycle of equatorial mixed layer heat adjustments, particularly through Ekman and geostrophic heat advection and entrainment, implies a strong relationship between WNP SSTs and both positive and negative feedback of ENSO.

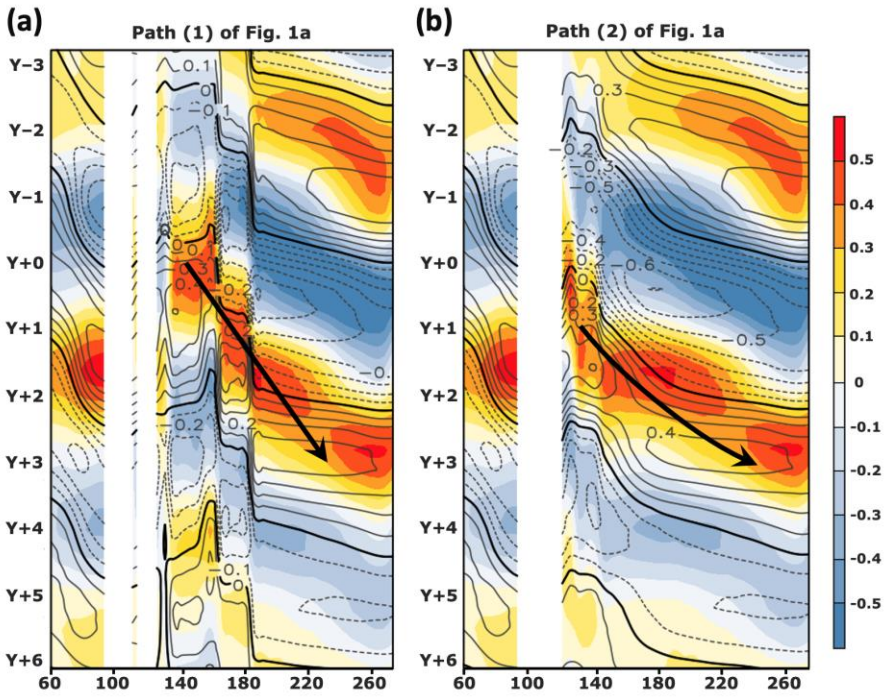

Fig. 10. Longitude-time sections of warm WNP SSTA at Y+0 correlated with SSHA (contours) and MLDA (shading). Latitude varies with longitude according to Fig. 1a path (1) for (a) and path (2) for (b). Y-axes indicate the year relative to the warm WNP phase. Positive SSHA and MLDA correlations propagate from (a) the western North Pacific at Y+0 and (b) just north of the western equatorial Pacific at Y+1 towards the central–eastern equatorial Pacific by Y+3 (black arrows).

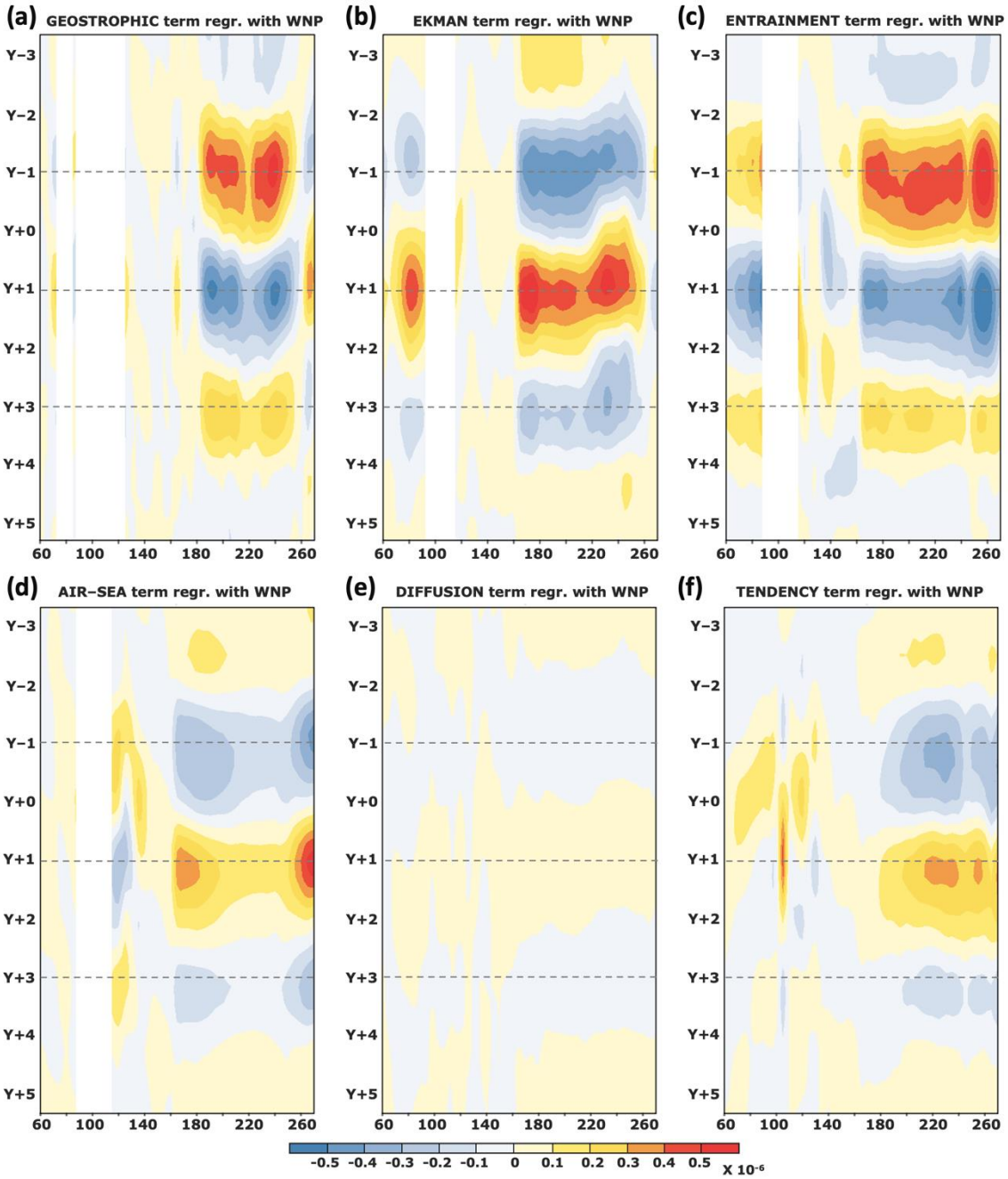

Fig. 11. Longitude-time sections of warm WNP SSTs at Y+0 regressed with mixed layer temperature tendency terms of (a) geostrophic and (b) Ekman heat advection, (c) entrainment, (d) air–sea heat flux, (e) diffusion, and (f) temperature tendency. Latitude varies with longitude according to path (1) of Fig. 1a. Values between 160°E to 260°E are related to heat adjustments in the central–eastern equatorial Pacific mixed layer. Values at Y–1 and Y+3 (Y–3, Y+1 and Y+5) can be associated with El Niño- (La Niña-) like conditions.

3.5 Discussion

3.5.1 WNP SSTA formation

According to these analyses, warm (cold) WNP SSTA formation results from an intensified (weakened) western boundary current linked to strengthened (weakened) trade winds (Figs. 2, S3). The effects of strengthened (weakened) trade winds in the equatorial Pacific vary greatly depending on the magnitude of the wind anomalies and are not always associated with La Niñas (El Niños). Strengthened (weakened) trade winds during La Niñas (El Niños) enhance (weaken) the easterly flow along the central equatorial Pacific and strengthen (weaken) the east–west gradients of SST, SSH and MLD that increase (decrease) warm water volume in the Western Pacific Warm Pool and intensify (reduce) upwelling in the eastern Pacific. However, the trade winds are much stronger (weaker) during a warm (cold) WNP phase (Figs. 2, S3). Stronger (weaker) deflection to the right in the Northern Hemisphere directs the winds towards the western (eastern) Pacific instead of the central Pacific and promotes surface divergence in the Western Pacific Warm Pool (eastern Pacific). Figures 2, 4, 5 and 6 were used to construct Figure 12 to elucidate the interpretations of WNP processes. For warm WNP phases, an intensified western boundary current increases coastal friction in the western North Pacific and promotes divergence and upwelling anomalies. Although this would intrinsically decrease the SST and SSH, the barrier layer thickness is preserved during shoaling and inhibits vertical mixing with colder water in the thermocline (Fig. 12a). The net effect of the intensified western boundary current is to increase the SST and SSH through stronger convergence of warmer, fresher water from the Western Pacific Warm Pool and strengthen vertical stratification from the surface to subsurface which preserves the warm WNP SSTA (Fig. 12b).

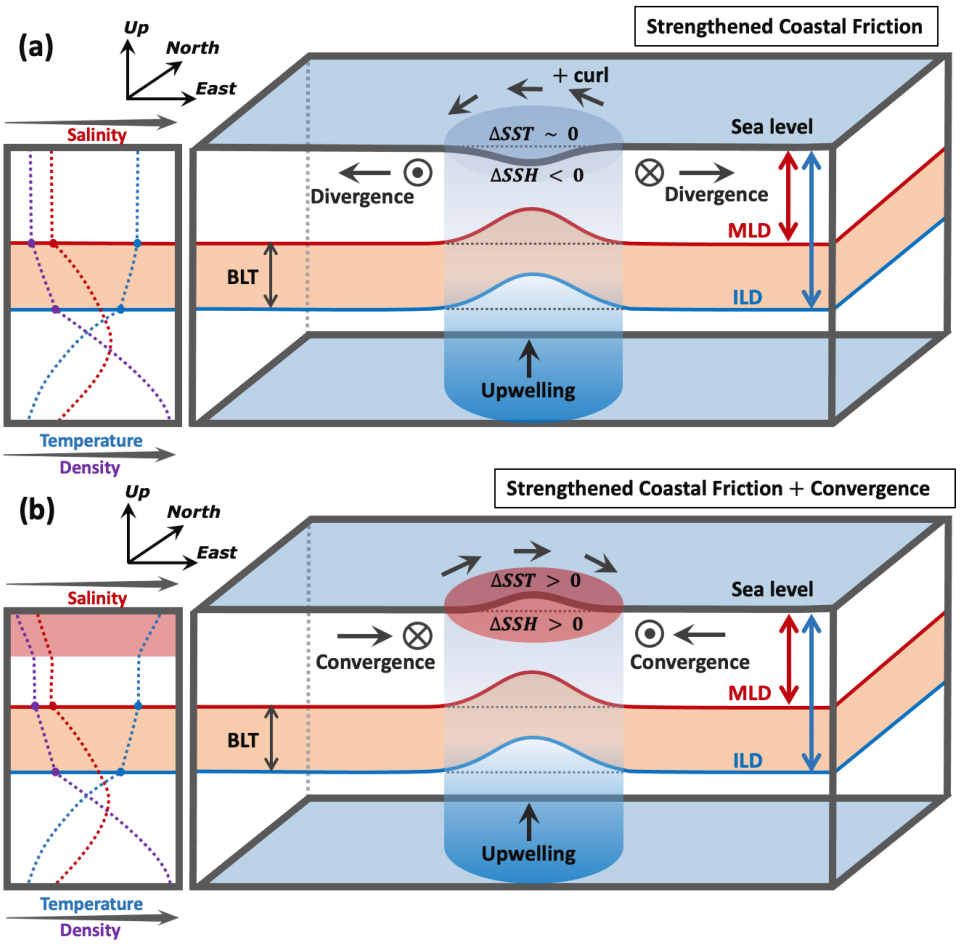

Fig. 12. Schematic diagrams illustrating the formation and preservation of warm WNP SSTAs near the coastline. (a) Positive wind stress curl anomalies from strengthened friction during the warm WNP phase promote divergence and coastal upwelling in the western North Pacific, which inherently decrease SSH and SST. Shoaling of near equal magnitude of MLD and ILD during a warm WNP phase maintains a constant barrier layer thickness (BLT), inhibits mixing between the MLD and colder water below, and retains heat in the MLD. Any changes in SST resulting from the effects of coastal upwelling are negligible. (b) Input of warmer and fresher surface water from the western boundary current converging in the western North Pacific increases the net SST and SSH. The less dense surface water strengthens the existing vertical stratification promoted by the barrier layer thickness and salinity inversion in the thermocline.

3.5.2 WNP SSTA persistence

Figures 2, 3 and 9, in conjunction with the fundamental dynamics of rotating stratified fluids compiled from various studies (Rossby 1937, 1938; Hsueh and Cushman-Roisin 1983; Ou 1984; van Heijst 1985; Cushman-Roisin and Beckers 2011), are applied in Figs. 13a–g to propose an explanation for the persistence of WNP SSTAs during propagation. A warm WNP SSTA forms

near the coastline and creates a horizontal density gradient towards the east that shifts the system out of equilibrium (Fig. 13a). To restore equilibrium, the more buoyant (denser) warm SSTA (relatively cold water) attempts to flow over (under) the relatively cold water (warm SSTA) to the east (west). In a non-rotating framework, a horizontal density gradient would allow unlimited "spilling" of both sides until all warmer (colder) water is over (under) colder (warmer) water. Such a scenario would infinitely extend an anomaly laterally and greatly reduce its vertical extent. However, in a rotating world, the Coriolis force acts on the forward acceleration and deflects the currents to the right. Fig. 13a represents the state of the system at the time of warm SSTA formation when the fluids on each side of the grey partition are at rest. When the partition is removed, the spreading is very limited for both water bodies and produces a frontal slope (Fig. 13c). This spreading distance d is the Rossby radius of deformation. As the warm SSTA (relatively cold water) starts moving east (west), the Coriolis force deflects the current southward (northward) at (under) the surface. When the warm SSTA moves away from the coastline, the same dynamics apply to the west of the SSTA that now becomes surrounded by water (Fig. 13e). The warm anomaly (relatively cold water) flows west (east) along the surface (subsurface) over (under) the relatively cold water (warm anomaly) and is deflected northward (southward), producing another frontal slope. This creates an anticyclonic (cyclonic) vorticity at the surface (base) of the warm SSTA.

Similarly, a cold WNP SSTA promotes lateral stratification towards the east and subsequently, disequilibrium (Fig. 13b). The denser (buoyant) cold SSTA (relatively warm water) flows to the east (west) under (over) the relatively warm water (cold SSTA). The eastward (westward) subsurface (surface) current of the cold SSTA (relatively warm water) is deflected southward (northward) to produce a frontal slope (Fig. 13d). Along the western edge of the SSTA as it moves away from the coastline, the cold anomaly (relatively warm water) attempts to flow to the west (east) under (over) the relatively warm water (cold SSTA) before the current is deflected

north (south; Fig. 13f). This creates a cyclonic (anticyclonic) vorticity at the surface (base) of the cold SSTA. These dynamics can be combined to place two opposite-signed SSTAs adjacent to each other in a state of equilibrium (Fig. 13g). This also explains why the warm (cold) SSTAs in Fig. 9c is associated with negative (positive) relative vorticity of surface currents. As gyres are shallow water systems, an SSTA propagating along the eastern boundary current is shallow enough to allow the entire vertical extent of the SSTA to still be influenced by the surface winds and rotational effects. By promoting lateral displacement of warm (cold) water over (under) cold (warm) water in small increments, the dynamics of rotating stratified fluids (i) confine both warm and cold SSTA in all lateral directions, (ii) preserve most of the vertical extent, and (iii) lengthen the propagation timeline. However, SSTA drift along a current may gradually shift the distribution of its water in the direction of the current, as observed in the buildup of warm water volume in the Western Pacific Warm Pool during warm SSTA propagation.

3.5.3 WNP SSTA propagation

Our analyses suggest that the 3-year WNP SSTA propagation is consistent with reshaping of an SSTA along the southeastern quadrant of the North Pacific Subtropical Gyre as it shifts between geostrophic equilibrium and geostrophic adjustment. An SSTA driven by the eastern boundary current can propagate over long distances and timescales towards the tropics largely under the influence of geostrophic flow dynamics. The SSH gradient from the gyre center is most pronounced to the southeast, which may explain why SSTA originating from the western North Pacific propagate to the central–eastern equatorial Pacific. During warm WNP SSTA propagation, the warm water reaches the tropics in two consecutive steps that are favorable for El Niño development:

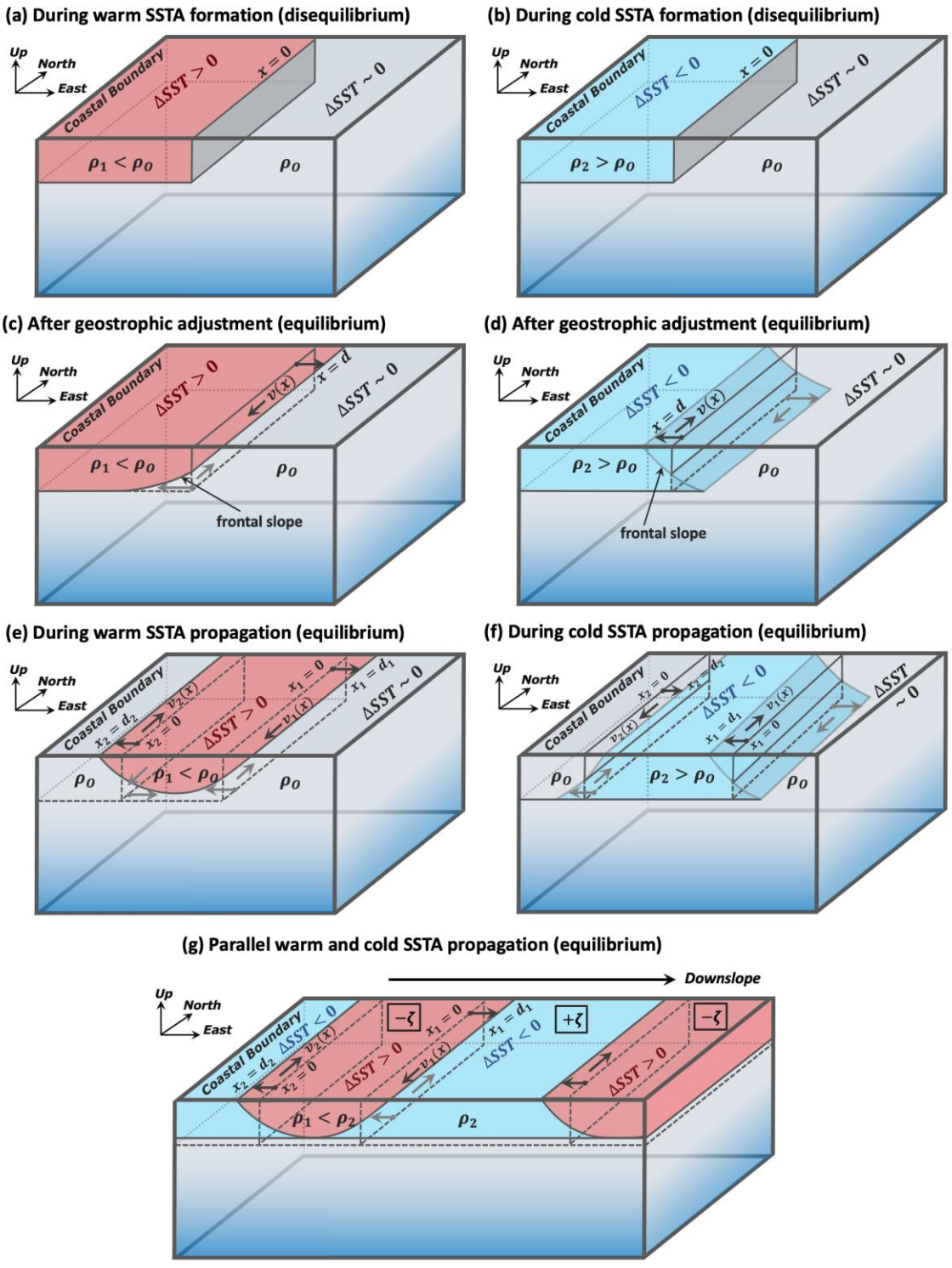

Fig. 13. Schematic illustrations associated with SSTA propagation from western North Pacific coastline. (a) Warm WNP SSTA forms near coastline and creates a horizontal density gradient towards the east (lateral stratification). (b) Same as (b) expect for cold WNP SSTA. (c) Warm SSTA (relatively cold water) travels small lateral distance to the east (west) at (below) the surface. (d) Cold SSTA (relatively warm water) travels small lateral distance to the east (west) below (at)

the surface. Coriolis force deflects currents to the right in the Northern hemisphere. The eastward (westward) currents are deflected to the south (north). In both (c) and (d), a frontal slope forms between the SSTA and adjacent water to east. (e) and (f) As the SSTAs move away from the coastline and become stratified to the west, frontal slopes form along the west of both SSTAs, generating negative (positive) relative vorticity in the warm (cold) SSTA at the surface. Frontal slopes can form in all directions of lateral stratification and preserve the vertical extent. (g) Parallel and adjacent warm and cold SSTA away from the coastline.

1) DJF TO DJF+1:

Most of the warm water volume of the SSTA is displaced southwest by the eastern boundary current and accumulates in the Western Pacific Warm Pool within the first year of propagation. During this period, the SSTA is closer to the gyre center where equatorward transport is strongest. The gyre speeds and Coriolis deflection weaken with eastward and southward movements, respectively. Strengthened downwelling during the warm WNP phase also transport heat anomalies towards the Western Pacific Warm Pool through the subsurface in the geostrophic layer. Increased warm water volume in the western tropical Pacific strengthens the east–west gradients of SST, SSH and MLD. However, westerly anomalies have yet to develop in the western equatorial Pacific in DJF+1 because (i) the warm water volume is still north of the equator (0°–15°N) and (ii) divergence associated with the cold SSTA in the equatorial Pacific (comparable to a La Niña) promotes easterly anomalies in the western equatorial Pacific.

2) DJF+1 TO DJF+3:

Steady southeast movement of the subtropical SSTA from DJF+1 to DJF+2 continues to supply the warm water to the western tropical Pacific. The cold SSTA in the equatorial Pacific shifts eastward while the warm water volume shifts slightly southeast to straddle the western equatorial Pacific. The eastward-propagating subtropical SSTA facilitates this shift by strengthening the east–west equatorial SST, SSH and MLD gradients. This promotes westerly anomalies in the western equatorial Pacific that work alongside the ongoing equatorward transport

of the subtropical SSTA strip to displace the warm water volume towards the eastern equatorial Pacific from DJF+2 to DJF+3, coinciding with an El Niño.

3.5.4 Influence of 1-year lead extratropical precursors on SSTA propagation

NPO-induced precursors may produce surface wind anomalies that help sustain the SSTA during the final year of the propagation leading up to the El Niño. A positive PMM phase in the boreal spring is characterized by the development of a warm SSTA off the coast of California and weakening of the trade winds (Fig.14a). The decrease in evaporation to the southwest of the SSTA extends the warm anomalies further southwest towards the western tropical Pacific and enhance the east–west warm water volume gradient. The warm anomaly in the northeastern subtropical Pacific may result from weakening of the high-pressure system, and subsequent weakening of the trade winds (Fig. 14b). A positive PMM phase during the final year of SSTA propagation may facilitate the transfer of warm WNP SSTA to the southwest and strengthen the east–west warm water volume gradient. This promotes westerly anomalies that shift the warm anomaly to the eastern Pacific in the seasons leading up to an El Niño. The Victoria Mode (VM) exhibits a nearly identical pattern as PMM, except VM is a basin-scale North Pacific mode that also includes negative SSTA in the western North Pacific, suggesting a close link between PMM and VM (Ding et al. 2018). PMM is sometimes be interconnected with WNP (Wang et al. 2015). A positive PMM phase may occur in the spring following a cold WNP phase the previous winter (Borhara et al. 2023) when the trade winds also inherently weaken (Fig. S3).

3.5.5 Limitations of this work

The robustness of the findings of this chapter may be impacted by results with lower than 95% confidence interval and limited sample size in observations due to sparse availability of subsurface ocean measurements prior to 2005. We relied on the performance of model data to corroborate the observations. In addition, given the limited number of existing studies, the

propagation subject remains in its early stages of exploration. This work puts forth a plausible dynamical explanation to the observations but cannot conclusively resolve this challenging issue at this time. Many future studies from different perspectives are required to address the cause.

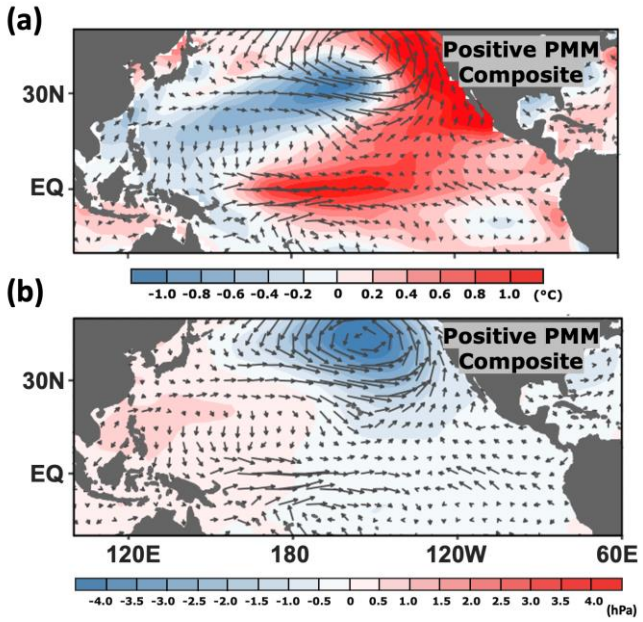

Fig. 14. (a) Positive PMM (MAM) anomaly composites of SST (°C; shading) and surface wind anomalies (m/s; vectors), followed by respective anomaly composites 1, 2 and 3 seasons later. (b) Positive PMM (MAM) anomaly composites of SLP (hPa; shading) and surface wind anomalies (m/s; vectors). The composites were constructed using the 8 PMM years extracted from the time series of the Pacific Meridional Mode by Chiang and Vimont (2004): MAM 1980, 1992, 1993, 1995, 1996, 2014, 2015 and 2016.

3.5.6 Directions for future work

I assert that this 3-year WNP–ENSO relationship is part of a more complex propagation pattern. Wang et al. (2015) identified a global eastward propagation pattern in which the SSTA signal first appears in the eastern Indian Ocean in the year prior to an El Niño, moves eastward towards the western North Pacific at the start of the El Niño year, and then towards the central Pacific to promote PMM by spring of the El Niño year. Inter-basin interactions are increasingly involved in influencing ENSO development at lead times longer than 1 year. Positive and negative phases of the Indian Ocean Dipole 14-months prior have been associated with the development of a La Niña and an El Niño, respectively (Izumo et al. 2010). SSTAs in the Western Hemisphere

Warm Pool are also reported to trigger ENSO at a 17-month lag time through PMM (Park et al. 2018). The time-varying nature of inter-basin connections documented by Schott et al. (2009) and Ham et al. (2016) aligns with the findings in this chapter of the multi-year SSTA signals linked to ENSO and their association with decadal variability. Given the complexity and uncertainties surrounding WNP dynamics compared to other climatic modes, analyses of the inter-basin connection originating from the Indian Ocean would constitute a crucial aspect of understanding the 3-year WNP–ENSO lead relationship.

3.6. Conclusions

The gradual movement of warm and cold SSTAs from the western North Pacific to the central–eastern equatorial Pacific can potentially extend ENSO prediction lead times up to 2–3 years in advance. The warm (cold) WNP SSTA results from a strengthened (weakened) western boundary current linked to strengthened (weakened) trade winds while the steady basin-scale propagation is promoted by the broader, slower, shallower, and equatorward Sverdrup transport along the eastern boundary current. Subtropical gyres and anomalies associated with rotating stratified fluids are either at or near a state of geostrophic equilibrium and therefore can persist over long periods. This study exemplifies how relationships between extratropical precursors and ENSO through subtropical gyres can lead to advancements in longer lead time (>1 year) ENSO predictions.

3.7 Supplementary Material

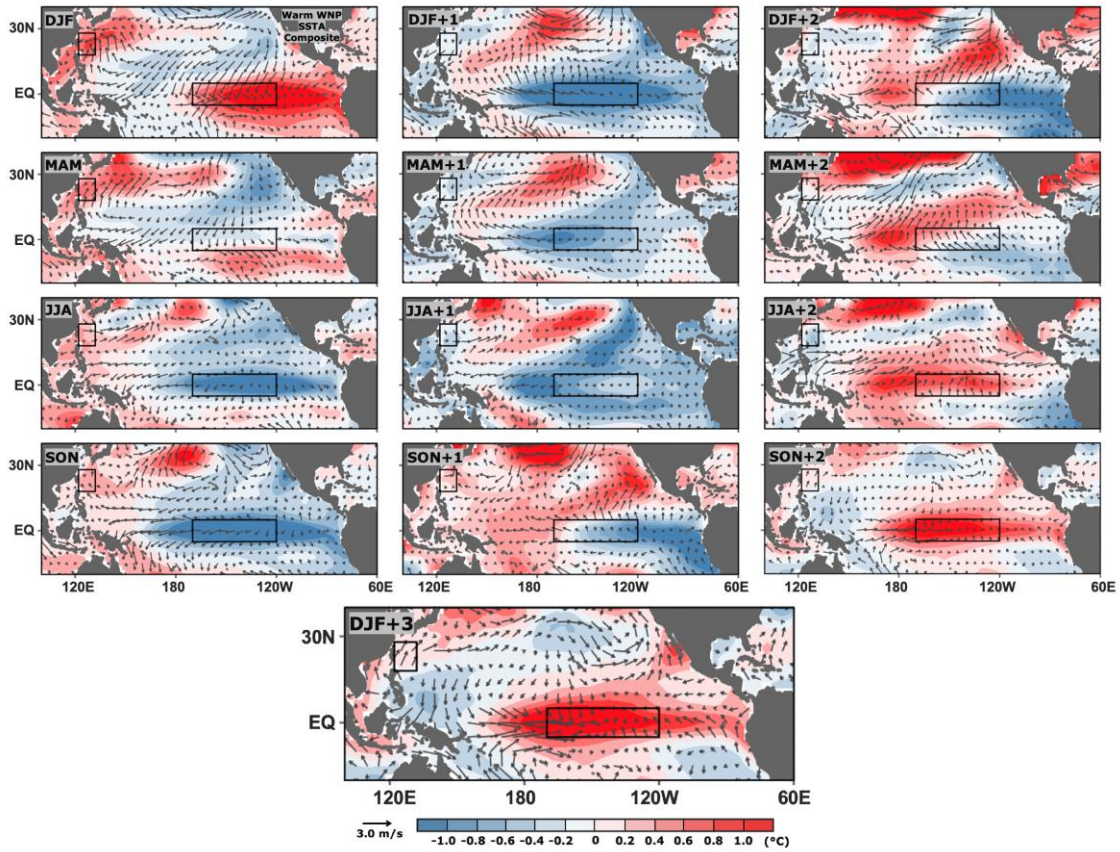

Fig. S1. Seasonal evolution of warm WNP SSTA from DJF to DJF+3. The warm SSTA strip is oriented northeast-southwest and propagates southeast throughout the 3-year period. Trade winds strengthen (weaken) during the warm WNP phase (El Niño) in DJF (DJF+3). Westerly anomalies develop in the western equatorial Pacific in the seasons leading up to an El Niño.

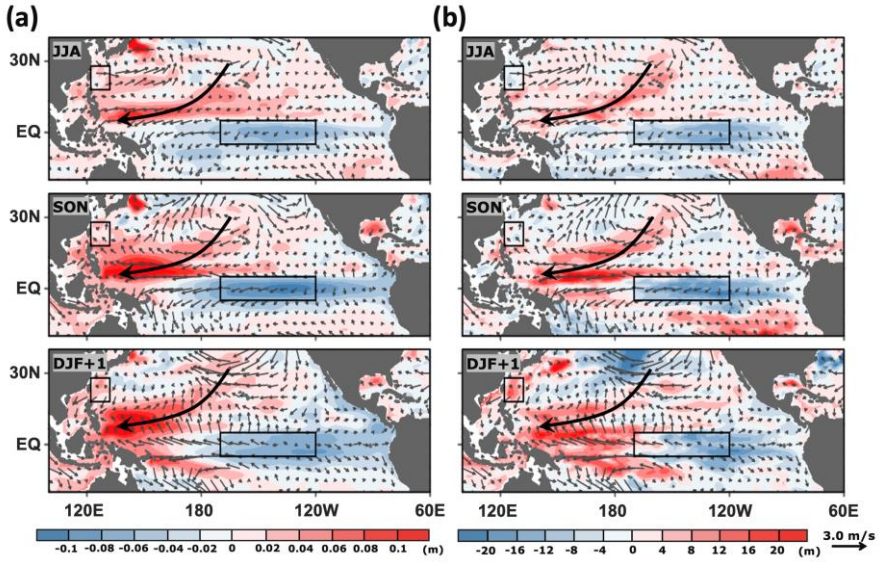

Fig. S2. Seasonal evolution of warm WNP SSHA and MLDA from JJA to DJF+1. Warm water volume decreases in the subtropics and increases in the tropics as positive SSHA and MLDA propagate southwest to the Western Pacific Warm Pool, along the SSTA strip in Fig. S1.

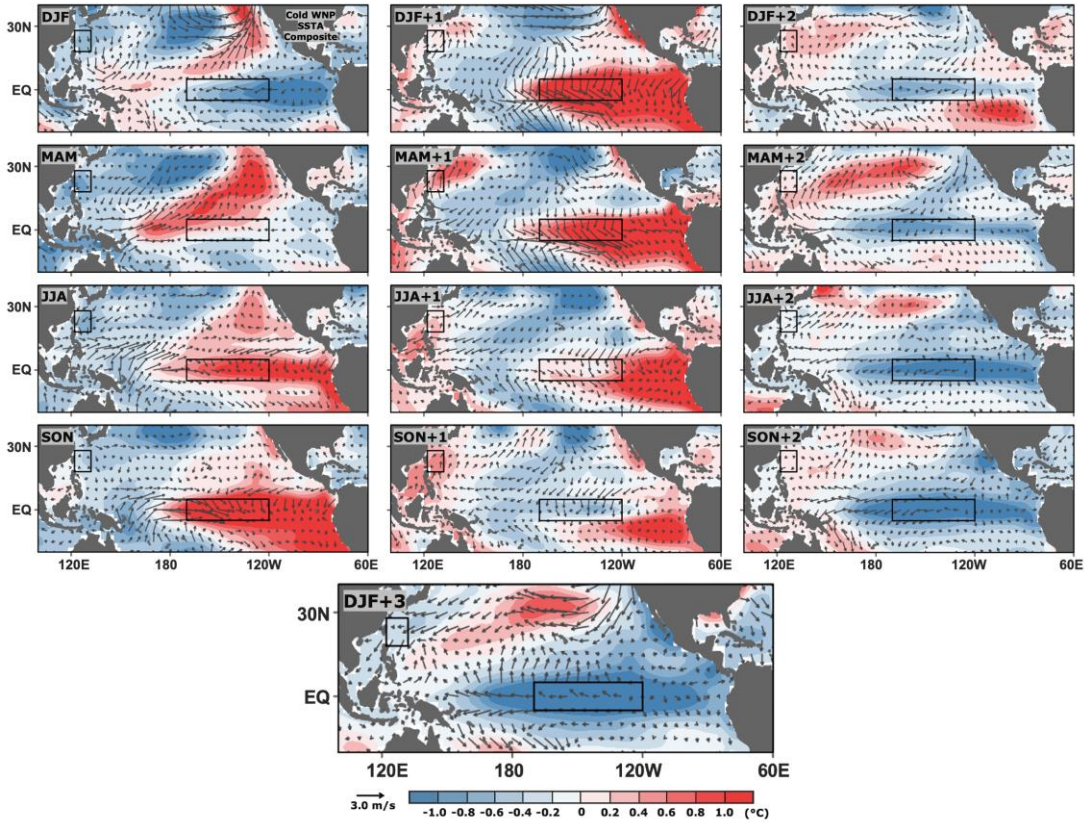

Fig. S3. Seasonal evolution of cold WNP SSTA from DJF to DJF+3. The cold SSTA strip is oriented northeast-southwest and propagates southeast throughout the 3-year period. Trade winds weaken (strengthen) during the cold WNP phase (La Niña) in DJF (DJF+3). Easterly anomalies develop in the western equatorial Pacific in the seasons leading up to a La Niña.

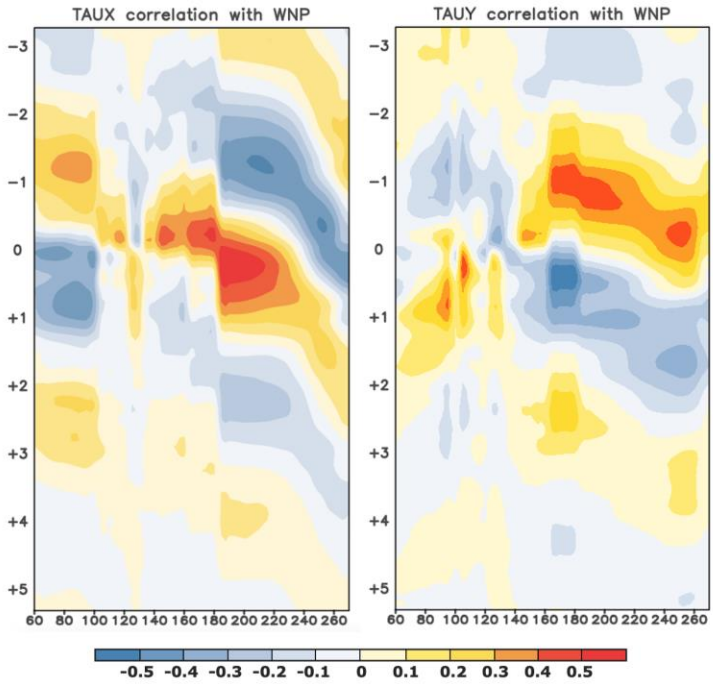

Fig. S4. Longitude-time sections of warm WNP SSTA at Y+0 correlated with anomalies of (left) zonal and (right) meridional wind stress. Latitude varies with longitude according to path (1) of Fig. 1a.

Derivation of the geostrophic transport equation:

$$\int_{z=-D_W}^{z=-D_E} v_g \, \partial z = \frac{1}{\rho \beta}\left(\frac{\partial \tau_y}{\partial x} - \frac{\partial \tau_x}{\partial y}\right) + \frac{\tau_x}{\rho f}$$

Geostrophic transport **Sverdrup transport** **–Ekman transport**

The general continuity equation for compressible or incompressible flow is expressed as (e.g., Childs 2011):

$$\frac{\partial \rho}{\partial t} + \frac{\partial(\rho u)}{\partial x} + \frac{\partial(\rho v)}{\partial y} + \frac{\partial(\rho w)}{\partial z} = 0 \qquad \ldots (1)$$

For an incompressible flow, ρ = constant in space and time, i.e., $\frac{\partial \rho}{\partial t} = \frac{\partial \rho}{\partial x} = \frac{\partial \rho}{\partial y} = \frac{\partial \rho}{\partial z} = 0$, therefore ρ can be pulled out of the derivative terms.

$$\cancel{\frac{\partial \rho}{\partial t}} + \frac{\rho \partial(u)}{\partial x} + \frac{\rho \partial(v)}{\partial y} + \frac{\rho \partial(w)}{\partial z} = 0$$

$$\rho\left(\frac{\partial u}{\partial x} + \frac{\partial v}{\partial y} + \frac{\partial w}{\partial z}\right) = 0$$

Divide by ρ on both sides, the continuity equation for an incompressible flow becomes (e.g., Childs 2011):

$$\frac{\partial u}{\partial x}+\frac{\partial v}{\partial y}+\frac{\partial w}{\partial z}=0$$

Assuming that the horizontal flows are geostrophic, the continuity equation becomes:

$$\frac{\partial u_g}{\partial x}+\frac{\partial v_g}{\partial y}+\frac{\partial w}{\partial z}=0 \qquad \ldots(2)$$

As geostrophy is the balance between Coriolis force (rotation) and horizontal pressure gradients, the geostrophic flow pressure gradients can be expressed as (e.g., Webster 2020):

$$fu_g=-\frac{1}{\rho}\frac{\partial P}{\partial y} \qquad \ldots(3)$$

$$fv_g=\frac{1}{\rho}\frac{\partial P}{\partial x} \qquad \ldots(4)$$

First, derive the $\frac{\partial}{\partial x}$ of eq. (3):

$$fu_g=-\frac{1}{\rho}\frac{\partial P}{\partial y}$$

$$\frac{\partial(fu_g)}{\partial x}=\frac{\partial(-\frac{1}{\rho}\frac{\partial P}{\partial y})}{\partial x}$$

Apply the product rule:

$$f\frac{\partial(u_g)}{\partial x}+u\cancel{\frac{\partial(f)}{\partial x}}=-\frac{1}{\rho}\frac{\partial^2 P}{\partial x\partial y}$$

f does not change with longitude $\left(\frac{\partial f}{\partial x}=0\right)$, therefore,

$$f\frac{\partial(u_g)}{\partial x}=-\frac{1}{\rho}\frac{\partial^2 P}{\partial x\partial y}$$

$$\frac{\partial(u_g)}{\partial x}=-\frac{1}{f\rho}\frac{\partial^2 P}{\partial x\partial y} \qquad \ldots(5)$$

Next, derive the $\frac{\partial}{\partial y}$ of eq. (4):

$$fv_g=\frac{1}{\rho}\frac{\partial P}{\partial x}$$

$$\frac{\partial(fv_g)}{\partial y}=\frac{\partial(\frac{1}{\rho}\frac{\partial P}{\partial x})}{\partial y}$$

Apply the product rule:

$$f\frac{\partial(v_g)}{\partial y}+v_g\frac{\partial(f)}{\partial y}=\frac{1}{\rho}\frac{\partial^2 P}{\partial x\partial y}$$

Since $\frac{\partial f}{\partial y}=\beta$,

$$f\frac{\partial(v_g)}{\partial y}+v_g\beta=\frac{1}{\rho}\frac{\partial^2 P}{\partial x\partial y}$$
$$f\frac{\partial(v_g)}{\partial y}=\frac{1}{\rho}\frac{\partial^2 P}{\partial x\partial y}-v_g\beta$$
$$\frac{\partial(v_g)}{\partial y}=\frac{1}{f\rho}\frac{\partial^2 P}{\partial x\partial y}-\frac{v_g\beta}{f} \qquad \ldots(6)$$

Substitute eq. (5) and (6) into the continuity equation of eq. (2):

$$\cancel{-\frac{1}{f\rho}\frac{\partial^2 P}{\partial x\partial y}}+\cancel{\frac{1}{f\rho}\frac{\partial^2 P}{\partial x\partial y}}-\frac{v_g\beta}{f}+\frac{\partial w}{\partial z}=0$$

The second derivatives cancel out to yield,

$$-\frac{\beta v_g}{f}+\frac{\partial w}{\partial z}=0$$
$$\beta v_g=f\frac{\partial w}{\partial z} \qquad \ldots(7)$$

Eq (7) is the well-established *Sverdrup balance* (e.g., Cushman-Roisin and Beckers 2011). Integrating eq. (7) from the base of the upper ocean (D_w) to the base of the Ekman layer (D_E) yields (e.g., Cushman-Roisin and Beckers 2011; Gray and Riser 2014):

$$\beta\int_{z=-D_W}^{z=-D_E} v_g\,\partial z=f[w_e(z=-D_E)-\cancel{w(z=-D_w)}]$$

The base of the upper ocean $z=-D_w$ here is assumed to be the "level of no motion", where the horizontal pressure gradients disappear and the vertical velocity $w(z=-D_w)$ becomes zero (e.g., Webster 2020).

$$\beta\int_{z=-D_W}^{z=-D_E} v_g\,\partial z=fw_e$$
$$\int_{z=-D_W}^{z=-D_E} v_g\,\partial z=\frac{f}{\beta}w_e \qquad \ldots(8)$$

where $w_e=\left[\nabla\times\left(\frac{\tau}{\rho f}\right)\right].k$ (e.g., Gray and Riser 2014)

$$w_e=\frac{\partial}{\partial x}\left(\frac{\tau_y}{\rho f}\right)-\frac{\partial}{\partial y}\left(\frac{\tau_x}{\rho f}\right)$$
$$w_e=\frac{1}{\rho}\left[\frac{\partial}{\partial x}\left(\frac{\tau_y}{f}\right)-\frac{\partial}{\partial y}\left(\frac{\tau_x}{f}\right)\right]$$

Apply the quotient rule:

$$w_e = \frac{1}{\rho}\left[\frac{f\frac{\partial}{\partial x}(\tau_y) - \tau_y \cancel{\frac{\partial}{\partial x}(f)}}{f^2} - \frac{f\frac{\partial}{\partial y}(\tau_x) - \tau_x\frac{\partial}{\partial y}(f)}{f^2}\right]$$

$$w_e = \frac{1}{\rho}\left[\frac{f\frac{\partial}{\partial x}(\tau_y)}{f^2} - \frac{f\frac{\partial}{\partial y}(\tau_x) + \tau_x\frac{\partial}{\partial y}(f)}{f^2}\right]$$

$$w_e = \frac{1}{\rho}\left[\frac{\frac{\partial}{\partial x}(\tau_y)}{f} - \frac{\frac{\partial}{\partial y}(\tau_x)}{f} + \frac{\tau_x\,\beta}{f^2}\right]$$

$$w_e = \frac{1}{\rho f}\left[\frac{\partial}{\partial x}(\tau_y) - \frac{\partial}{\partial y}(\tau_x) + \frac{\tau_x\,\beta}{f}\right] \qquad \text{... (9)}$$

Substitute eq (9) into eq (8) above:

$$\int_{z=-D_W}^{z=-D_E} v_g\,\partial z = \frac{1}{\rho\beta}\left[\frac{\partial}{\partial x}(\tau_y) - \frac{\partial}{\partial y}(\tau_x) + \frac{\tau_x\,\beta}{f}\right]$$

which gives us the equation in question (eq. 10):

$$\int_{z=-D_W}^{z=-D_E} v_g\,\partial z = \frac{1}{\rho\,\beta}\left(\frac{\partial\,\tau_y}{\partial x} - \frac{\partial\,\tau_x}{\partial y}\right) + \frac{\tau_x}{\rho\,f}$$

Geostrophic transport **Sverdrup transport** **–Ekman transport**

… (10)

REFERENCES

Alexander, M. A., D. J. Vimont, P. Chang, and J. D. Scott, 2010: The impact of extratropical atmospheric variability on ENSO: Testing the seasonal footprinting mechanism using coupled model experiments. *J. Climate*, **23**, 2885–2901, https://doi.org/10.1175/2010JCLI3205.1

Anderson, B. T., R. C. Perez, and A. Karspeck, 2013: Triggering of El Niño onset through trade wind–induced charging of the equatorial Pacific. *Geophys. Res. Lett.*, **40**, 1212–1216, https://doi.org/10.1002/grl.50200

Aoki, K., and K. Kutsuwada, 2008: Verification of the wind-driven transport in the North Pacific subtropical gyre using gridded wind-stress products. *J. Oceanogr.*, **64**, 49–60. https://doi.org/10.1007/s10872-008-0004-6

Armstrong, D. A., B. A. Mitchell-Innes, F. Verheye-Dua, H. Waldron, and L. Hutchings, 1987: Physical and biological features across an upwelling front in the southern Benguela. *S. Afr. J. Mar. Sci.*, **5**, 171–190, https://doi.org/10.2989/025776187784522559

Ashafahani, A. A., A. Wirasatriya, W. S. Pranowo, D. N. Sugianto, and L. Maslukah, 2021: The Dynamic of Convergence Zone Displacement in Western Pacific Ocean on 2015 Super El Niño Event. *IOP Conf. Ser. Earth Environ. Sci*., **750** 012015, https://doi.org/10.1088/1755-1315/750/1/012015

Ashok, K., S. K. Behera, S. A. Rao, H. Weng, and T. Yamagata, 2007: El Niño Modoki and its possible teleconnections. *J. Geophys. Res.*, **112**, C11007, https://doi.org/10.1029/2006JC003798

Behringer, D. W., M. Ji, and A. Leetmaa, 1998: An improved coupled model for ENSO prediction and implications for ocean initialization. Part I: The ocean data assimilation system. *Mon. Wea. Rev.*, **126**, 1013–1021, https://doi.org/10.1175/1520-0493(1998)126<1013:AICMFE>2.0.CO;2

Behringer, D. W., and Y. Xue, 2004: Evaluation of the global ocean data assimilation system at NCEP: The Pacific Ocean. *Eighth Symposium on Integrated Observing and Assimilation Systems for Atmosphere, Oceans, and Land Surface*, AMS 84th Annual Meeting, Washington State Convention and Trade Center, Seattle, Washington, 11–15.

Bjerknes, J., 1966: A possible response of the atmospheric Hadley circulation to equatorial anomalies of ocean temperature. *Tellus*, **18**, 820–829, https://doi.org/10.1111/j.2153-3490.1966.tb00303.x

Bjerknes, J., 1969: Atmospheric teleconnections from the equatorial Pacific. *Mon. Wea. Rev.*, **97**, 163–172, https://doi.org/10.1175/1520-0493(1969)097%3c0163:atftep%3e2.3.co;2

Bond, N. A., J. E. Overland, M. Spillane, and P. Stabeno, 2003: Recent shifts in the state of the North Pacific. *Geophys. Res. Lett.*, **30**, 2183, https://doi.org/10.1029/2003GL018597

Borhara, K., B. Fosu, and S.-Y. Wang, 2023: The role of the western North Pacific (WNP) as an El Niño–Southern Oscillation (ENSO) precursor in a warmer future climate. *Climate Dyn.*, https://doi.org/10.1007/s00382-023-06773-z

Boschat, G., P. Terray, and S. Masson, 2013: Extratropical forcing of ENSO. *Geophys. Res. Lett.*, **40**, 1605–1611, https://doi.org/10.1002/grl.50229

Brandt, P., and Coauthors, 2015: On the role of circulation and mixing in the ventilation of oxygen minimum zones with a focus on the eastern tropical North Atlantic. *Biogeosciences*, **12**, 489–512, https://doi.org/10.5194/bg-12-489-2015

Buckley, M. W., and J. Marshall, 2016: Observations, inferences, and mechanisms of the Atlantic Meridional Overturning Circulation: A review. *Rev. Geophys.*, **54**, 5–63, https://doi.org/10.1002/2015RG000493

Burchard, H., N. B. Basdurak, U. Gräwe, M. Knoll, V. Mohrholz, and S. Müller, 2017: Salinity inversions in the thermocline under upwelling favorable winds. *Geophys. Res. Lett.*, **44**, 1422–1428, https://doi.org/10.1002/2016GL072101

Cai, W., and Coauthors, 2014: Increasing frequency of extreme El Niño events due to greenhouse warming. *Nat. Climate Change*, **4**, 111–116, https://doi.org/10.1038/nclimate2100

Cai, W., and Coauthors, 2018: Increased variability of eastern Pacific El Niño under greenhouse warming. *Nat.*, **564**, 201–206, https://doi.org/10.1038/s41586-018-0776-9

Cane, M. A., S. E. Zebiak, and S. C. Dolan, 1986: Experimental forecasts of El Niño. *Nat.*, **321**, 827–832, https://doi.org/10.1038/321827a0

Capotondi, A., C. Deser, A. S. Phillips, Y. Okumura, and S. M. Larson, 2020: ENSO and Pacific Decadal Variability in the Community Earth System Model Version 2. *J. Adv. Model. Earth Syst.*, **12**, e2019MS002022, https://doi.org/10.1029/2019MS002022

Capotondi, A., and Coauthors, 2015: Understanding ENSO Diversity. *Bull. Amer. Meteor. Soc.*, **96**, 921–938, https://doi.org/10.1175/BAMS-D-13-00117.1

Chakravorty, S., R. C. Perez, B. T. Anderson, B. S. Giese, S. M. Larson, and V. Pivotti, 2020: Testing the Trade Wind Charging Mechanism and Its Influence on ENSO Variability. *J. Climate*, **33**, 7391–7411, https://doi.org/10.1175/JCLI-D-19-0727.1

Chen, H.-C., Y.-H. Tseng, Z.-Z. Hu, and R. Ding, 2020: Enhancing the ENSO Predictability beyond the Spring Barrier. *Sci. Rep.*, **10**, 984, https://doi.org/10.1038/s41598-020-57853-7

Chen, S., and B. Yu, 2020: The seasonal footprinting mechanism in large ensemble simulations of the second generation Canadian earth system model: uncertainty due to internal climate variability. *Climate Dyn.*, **55**, 2523–2541, https://doi.org/10.1007/s00382-020-05396-y

Chen, G., R. X. Huang, Q. Peng, and X. Chu, 2022: A Time-Dependent Sverdrup Relation and Its Application to the Indian Ocean. *J. Phys. Oceanogr.*, **52**, 1233–1244. https://doi.org/10.1175/JPO-D-21-0223.1

Chiang, J. C. H., and D. J. Vimont, 2004: Analogous Pacific and Atlantic Meridional Modes of Tropical Atmosphere–Ocean Variability. J. Climate, 17, 4143–4158, https://doi.org/10.1175/JCLI4953.1.

Childs, P. R. N., 2011: *Laws of motion*. In Rotating flow, 17–52. https://doi.org/10.1016/B978-0-12-382098-3.00002-0

Cushman-Roisin, B., and J.-M. Beckers, 2011: Introduction to Geophysical Fluid Dynamics Physical and Numerical Aspects. *Dynamics of Stratified Rotating Flows*. No. 101, Int. Geophys., 473–520, https://doi.org/10.1016/B978-0-12-088759-0.00015-8

Danabasoglu, G., and Coauthors, 2020: The Community Earth System Model Version 2 (CESM2). *J. Adv. Model. Earth Syst.*, **12**, e2019MS001916, https://doi.org/10.1029/2019MS001916

Delcroix, T., G. Eldin, M.-H. Radenac, J. Toole, and E. Firing, 1992: Variation of the western equatorial Pacific Ocean, 1986–1988. *J. Geophys. Res.*, **97**, 5423–5445, https://doi.org/10.1029/92JC00127

Dewitte, B., and Coauthors, 2012: Change in El Niño flavours over 1958–2008: Implications for the long-term trend of the upwelling off Peru. *Deep Sea Res., Part II*, **77–80**, 143–156, https://doi.org/10.1016/j.dsr2.2012.04.011

Ding, R., J. Li, Y.-H. Tseng, C. Sun, and Y. Guo, 2015: The Victoria mode in the North Pacific linking extratropical sea level pressure variations to ENSO. *J. Geophys. Res. Atmos.*, **120**, 27–45, https://doi.org/10.1002/2014jd022221

Ding, R., J. Li, Y.-h. Tseng, L. Li, C. Sun, and F. Xie, 2018: Influences of the North Pacific Victoria Mode on the South China Sea Summer Monsoon. *Atmosphere* **9**, 229, https://doi.org/10.3390/atmos9060229

Ding, R., and Coauthors, 2022: Multi-year El Niño events tied to the North Pacific Oscillation. *Nat. Commun.*, **13**, 3871, https://doi.org/10.1038/s41467-022-31516-9

Dong, S., and K. A. Kelly, 2004: Heat Budget in the Gulf Stream Region: The Importance of Heat Storage and Advection. *J. Phys. Oceanogr.* **34**, 1214–1231, https://doi.org/10.1175/1520-0485(2004)034<1214:HBITGS>2.0.CO;2

Dong, S., S. T. Gille, and J. Sprintall, 2007: An assessment of the Southern Ocean mixed layer heat budget. *J. Climate*, **20**, 4425–4442, https://doi.org/10.1175/JCLI4259.1

Duan, W., and C. Wei, 2012: The 'spring predictability barrier' for ENSO predictions and its possible mechanism: Results from a fully coupled model. *Int. J. Climatol.*, **33**, 1280–1292, https://doi.org/10.1002/joc.3513

Fan, H., S. Yang, C. Wang, Y. Wu, and G. Zhang, 2022: Strengthening Amplitude and Impact of the Pacific Meridional Mode on ENSO in the Warming Climate Depicted by CMIP6 Models. *J. Climate*, **35**, 5195–5213, https://doi.org/10.1175/JCLI-D-21-0683.1

Fang, S.-W., and J.-Y. Yu, 2020: A control of ENSO transition complexity by tropical Pacific mean SSTs through tropical-subtropical interaction. *Geophys. Res. Lett.*, **47**, e2020GL087933, https://doi.org/10.1029/2020GL087933

Ferrari, R., and D. Ferreira, 2011: What processes drive the ocean heat transport? *Ocean Model.*, **38**, 171–186, https://doi.org/10.1016/j.ocemod.2011.02.013

Fisher, R. A., 1915: Frequency distribution of the values of the correlation coefficient in samples of an indefinitely large population. *Biometrika*, **10**, 507–521, https://doi.org/10.1093/biomet/10.4.507

Fosu, B., J. He, and S.-Y. Wang, 2020: The influence of wintertime SST variability in the Western North Pacific on ENSO diversity. *Climate Dyn.*, **54**, 3641–3654, https://doi.org/10.1007/s00382-020-05193-7

Furtado, J. C., E. Di Lorenzo, B. T. Anderson, and N. Schneider, 2012: Linkages between the North Pacific Oscillation and central tropical Pacific SSTs at low frequencies. *Climate Dyn.*, **39**, 2833–2846, https://doi.org/10.1007/s00382-011-1245-4

Ganachaud, A., and C. Wunsch, 2003: Large-scale ocean heat and freshwater transports during the World Ocean Circulation Experiment. *J. Climate*, **16**, 696–705, https://doi.org/10.1175/1520-0442(2003)016<0696:LSOHAF>2.0.CO;2

Gray, A. R., and S. C. Riser, 2014: A Global Analysis of Sverdrup Balance Using Absolute Geostrophic Velocities from Argo. *J. Phys. Oceanogr*., **44**, 1213–1229, https://doi.org/10.1175/JPO-D-12-0206.1

Ham, Y.-G., J.-Y. Choi, and J.-S. Kug, 2017: The weakening of the ENSO–Indian Ocean Dipole (IOD) coupling strength in recent decades. *Climate Dyn.*, **49**, 249–261. https://doi.org/10.1007/s00382-016-3339-5

Ham, Y.-G., and J.-S. Kug, 2012: How well do current climate models simulate two types of El Niño? *Climate Dyn.*, **39**, 383–398, https://doi.org/10.1007/s00382-011-1157-3

Hsueh, Y., and B. Cushman-Roisin, 1983: On the formation of surface to bottom fronts over steep topography. *J. Geophys. Res. Oceans*, **88**, 743–750, https://doi.org/10.1029/JC088iC01p00743

Huang, B., P. W. Thorne, V. F. Banzon, T. Boyer, G. Chepurin, J. H. Lawrimore, M. J. Menne, T. M. Smith, R. S. Vose, and H.-M. Zhang, 2017: Extended Reconstructed Sea Surface Temperature, Version 5 (ERSSTv5): Upgrades, Validations, and Intercomparisons. *J. Climate*, **30**, 8179–8205, https://doi.org/10.1175/JCLI-D-16-0836.1

Izumo, T., and Coauthors, 2020: Influence of the state of the Indian Ocean Dipole on the following year's El Niño. *Nat.*, **3**, 168–172 (2010) https://doi.org/10.1038/ngeo760

Jia, F., W. Cai, B. Gan, L. Wu, and E. Di Lorenzo, 2021: Enhanced North Pacific impact on El Niño/Southern Oscillation under greenhouse warming. *Nat. Climate Change*, **11**, 840–847, https://doi.org/10.1038/s41558-021-01139-x

Jin, E. K., and Coauthors, 2008: Current status of ENSO prediction skill in coupled ocean–atmosphere models. *Climate Dyn.*, **31**, 647–664, https://doi.org/10.1007/s00382-008-0397-3

Jin, F.-F., 1997a: An equatorial ocean recharge paradigm for ENSO. Part I: Conceptual model. *J. Atmos. Sci.*, **54**, 811–829, https://doi.org/10.1175/1520-0469(1997)054<0811:AEORPF>2.0.CO;2

Jin, F.-F., 1997b: An equatorial ocean recharge paradigm for ENSO. Part II: A stripped-down coupled model. *J. Atmos. Sci.*, **54**, 830–847, https://doi.org/10.1175/1520-0469(1997)054<0830:AEORPF>2.0.CO;2

Jong, B., M. Ting, R. Seager, N. Henderson, and D. E. Lee, 2018: Role of Equatorial Pacific SST Forecast Error in the Late Winter California Precipitation Forecast for the 2015/16 El Niño. *J. Climate*, **31**, 839–852, https://doi.org/10.1175/JCLI-D-17-0145.1

Kalnay, E., and Coauthors, 1996: The NCEP/NCAR 40-year reanalysis project. *Bull. Amer. Meteor. Soc.*, **77**, 437–472, https://doi.org/10.1175/1520-0477(1996)077<0437:TNYRP>2.0.CO;2

Kao, H.-Y., and J.-Y. Yu, 2009: Contrasting eastern-Pacific and central-Pacific types of ENSO. *J. Climate*, **22**, 615–632, https://doi.org/10.1175/2008JCLI2309.1

Karnauskas, K. B., 2013: Can we distinguish canonical El Niño from Modoki? *Geophys. Res. Lett.*, **40**, 5246–5251, https://doi.org/10.1002/grl.51007

Kim, H.-M., P. J. Webster, and J. A. Curry, 2009: Impact of Shifting Patterns of Pacific Ocean Warming on North Atlantic Tropical Cyclones. *Sci.*, **325**, 77–80, https://doi.org/10.1126/science.1174062

Kim, J.-W., and J.-Y. Yu, 2020: Understanding reintensified multiyear El Niño events. *Geophys. Res. Lett.*, **47**, e2020GL087644, https://doi.org/10.1029/2020GL087644

Kim, J.-W., and J.-Y. Yu, 2021: Evolution of subtropical Pacific-onset El Niño: How its onset location controls its decay evolution. *Geophys. Res. Lett.*, **48**, e2020GL091345. https://doi.org/10.1029/2020GL091345

Kim, J.-W., and J.-Y. Yu, 2022: Single- and multi-year ENSO events controlled by pantropical climate interactions. *npj Climate Atmos. Sci.*, **5**, 88, https://doi.org/10.1038/s41612-022-00305-y

Kim, J.-W., J.-Y. Yu, and B. Tian, 2023: Overemphasized role of preceding strong El Niño in generating multi-year La Niña events. *Nat. Commun.* **14**, 6790. https://doi.org/10.1038/s41467-023-42373-5

Kim, S., and J.-S. Kug, 2018: What controls ENSO teleconnection to East Asia? Role of western North Pacific precipitation in ENSO teleconnection to East Asia. *J. Geophys. Res.*, **123**, 10406–10422, https://doi.org/10.1029/2018JD028935

Kim, S.-T., and J.-Y. Yu, 2012: The two types of ENSO in CMIP5 models. *Geophys. Res. Lett.*, **39**, L11704, https://doi.org/10.1029/2012GL052006

Kuhlbrodt, T., A. Griesel, M. Montoya, A. Levermann, M. Hofmann, and S. Rahmstorf, 2007: On the driving processes of the Atlantic meridional overturning circulation. *Rev. Geophys.*, **45**, RG2001, https://doi.org/10.1029/2004RG000166

Kutsuwada, K., A. Kakiuchi, Y. Sasai, et al., 2019: Wind-driven North Pacific Tropical Gyre using high-resolution simulation outputs. *J. Oceanogr*. 75, 81–93. https://doi.org/10.1007/s10872-018-0487-8

Larkin, N. K., and D. E. Harrison, 2005: On the definition of El Niño and associated seasonal average U.S. weather anomalies. *Geophys. Res. Lett.*, **32**, L13705, https://doi.org/10.1029/2005GL022738

Larson, S. M., and B. P. Kirtman, 2013: The Pacific Meridional Mode as a trigger for ENSO in a high-resolution coupled model. *Geophys. Res. Lett.*, **40**, 3189–3194, https://doi.org/10.1002/grl.50571

Larson, S. M., and B. P. Kirtman, 2014: The Pacific meridional mode as an ENSO precursor and predictor in the North American multimodel ensemble. *J. Climate*, **27**, 7018–7032, https://doi.org/10.1175/JCLI-D-14-00055.1

Lee, R. W., C.-Y. Tam, S.-J. Sohn, and J.-B. Ahn, 2018: Predictability of two types of El Niño and their climate impacts in boreal spring to summer in coupled models. *Climate Dyn.*, **51**, 4555–4571, https://doi.org/10.1007/s00382-017-4039-5

Lee, T., and M. J. McPhaden, 2010: Increasing intensity of El Niño in the central-equatorial Pacific. *Geophys. Res. Lett.*, **37**, L14603, https://doi.org/10.1029/2010GL044007

Linkin, M. E., and S. Nigam, 2008: The North Pacific Oscillation–west Pacific teleconnection pattern: Mature-phase structure and winter impacts. *J. Climate*, **21**, 1979–1997, https://doi.org/10.1175/2007JCLI2048.1

Liu, T., X. Song, Y. Tang, Z. Shen, and X. Tan, 2022: ENSO Predictability over the Past 137 Years Based on a CESM Ensemble Prediction System. *J. Climate*, **35**, 763–777, https://doi.org/10.1175/JCLI-D-21-0450.1

Luo, J., and T. Yamagata, 2003: A Model Study on the 1988–89 Warming Event in the Northern North Pacific. *J. Phys. Oceanogr.* **33**, 1815–1828, https://doi.org/10.1175/2413.1

McPhaden, M. J., 2004: Evolution of the 2002/03 El Niño. *Bull. Amer. Meteor. Soc.*, **85**, 677–696, https://doi.org/10.1175/BAMS-85-5-677

McPhaden, M. J., 2015: Playing hide and seek with El Niño. *Nat. Climate Change*, **5**, 791–795, https://doi.org/10.1038/nclimate2775

McPhaden, M. J., F. Bahr, Y. Du Penhoat, E. Firing, S. P. Hayes, P. P. Niiler, P. L. Richardson, and J. M. Toole, 1992: The response of the western equatorial Pacific Ocean to westerly wind bursts during November 1989 to January 1990. *J. Geophys. Res.*, **97**, 14289–14303, https://doi.org/10.1029/92JC01197

McPhaden, M. J., and R. A. Fine, 1988: A dynamical interpretation of the tritium maximum in the central equatorial Pacific. *J. Phys. Oceanogr.* **18**, 1454–1457. https://doi.org/10.1175/1520-0485(1988)018<1454:ADIOTT>2.0.CO;2

McPhaden, M. J., and D. Zhang, 2002: Slowdown of the meridional overturning circulation in the upper Pacific Ocean. *Nature* 415, 603–608. https://doi.org/10.1038/415603a

Ou, H. W., 1984: Geostrophic adjustment: A mechanism for frontogenesis. *J. Phys. Oceanogr.*, **14**, 994–1000, https://doi.org/10.1175/1520-0485(1984)014<0994:GAAMFF>2.0.CO;2

Paek, H., J.-Y. Yu, and C. Qian, 2017: Why were the 2015/2016 and 1997/1998 extreme El Niños different?. *Geophys. Res. Lett.*, **44**, 1848–1856, https://doi.org/10.1002/2016GL071515

Park, J.-Y., S.-W. Yeh, J.-S. Kug, and J. Yoon, 2013: Favorable connections between seasonal footprinting mechanism and El Niño. *Climate Dyn.*, **40**, 1169–1181, https://doi.org/10.1007/s00382-012-1477-y

Park, J.-H., J.-S. Kug, T. Li, and S. W. Behera 2018: Predicting El Niño Beyond 1-year Lead: Effect of the Western Hemisphere Warm Pool. *Sci Rep* **8**, 14957. https://doi.org/10.1038/s41598-018-33191-7

Pegion, K., C. M. Selman, S. Larson, J. C. Furtado, and E. J. Becker, 2020: The impact of the extratropics on ENSO diversity and predictability. *Climate Dyn.*, **54**, 4469–4484, https://doi.org/10.1007/s00382-020-05232-3

Pegion, K. V., and C. Selman, 2017: Extratropical Precursors of the El Niño–Southern Oscillation. *Climate Extremes Patterns and Mechanisms, Geophys. Monogr. Ser.*, No. 226, Amer. Geophys. Union, 301–314, https://doi.org/10.1002/9781119068020.ch18

Picaut, J., M. Ioualalen, C. Menkes, T. Delcroix, and M. J. McPhaden, 1996: Mechanism of the zonal displacements of the Pacific warm pool: Implications for ENSO. *Sci.*, **274**, 1486–1489, https://doi.org/10.1126/science.274.5292.1486

Picaut, J., F. Masia, and Y. Du Penhoat, 1997: An advective-reflective conceptual model for the oscillatory nature of the ENSO. *Sci.*, **277**, 663–666, https://doi.org/10.1126/science.277.5326.663

Qiu, B., and K. A. Kelly, 1993: Upper-Ocean Heat Balance in the Kuroshio Extension Region. *J. Phys. Oceanogr.* **23**, 2027–2041, https://doi.org/10.1175/1520-0485(1993)023<2027:UOHBIT>2.0.CO;2

Ren, H.-L., F.-F. Jin, B. Tian, and A. A. Scaife, 2016: Distinct persistence barriers in two types of ENSO. *Geophys. Res. Lett.* **43**, 10973–10979, https://doi.org/10.1002/2016GL071015

Ren, H.-L., R. Wang, P. Zhai, Y. Ding, and B. Lu, 2017: Upper-ocean dynamical features and prediction of the super El Niño in 2015/16: A comparison with the cases in 1982/83 and 1997/98. *J. Meteor. Res.*, **31**, 278–294, https://doi.org/10.1007/s13351-017-6194-3

Ren, H.-L., J. Zuo, and Y. Deng, 2019: Statistical predictability of Niño indices for two types of ENSO. *Climate Dyn.*, **52**, 5361–5382, https://doi.org/10.1007/s00382-018-4453-3

Rodgers, K. B., S.-S. Lee, and N. Rosenbloom, 2021: Ubiquity of human-induced changes in climate variability. *Earth Syst. Dyn.*, **12**, 1393–1411, https://doi.org/10.5194/esd-12-1393-2021

Rogers, J. C., 1981: The North Pacific Oscillation. *J. Climatol.*, **1**, 39–57, https://doi.org/10.1002/joc.3370010106

Rossby, C. G., 1937: On the mutual adjustment of pressure and velocity distributions in certain simple current systems. I. *J. Mar. Res.*, **1**, 15–28.

Rossby, C. G., 1938: On the mutual adjustment of pressure and velocity distributions in certain simple current systems. II. *J. Mar. Res.*, **2**, 239–263.

Schott, F. A., S.-P. Xie, and J. P. McCreary Jr., 2009: Indian Ocean circulation and climate variability. *Rev. Geophys.*, **47**, RG1002, https://doi.org/10.1029/2007RG000245

Shi, L., and R. Ding, 2020: Contributions of tropical–extratropical oceans to the prediction skill of ENSO after 2000. *Atmos. Oceanic Sci. Lett.*, **13**, 338–345, https://doi.org/10.1080/16742834.2020.1755600

Shi, L., R. Ding, S. Hu, J. Li, Y. Tseng, and X. Li, 2022: Influence of the North Pacific Victoria mode on the spring persistence barrier of ENSO. *J. Geophys. Res. Atmos.*, **127**, e2021JD036206, https://doi.org/10.1029/2021JD036206

Shin, C. S., and B. Huang, 2016: Revisiting the false alarm in the 2014 El Niño prediction. American Geophysical Union, Fall Meeting 2016, abstract #A43C-0239, https://ui.adsabs.harvard.edu/abs/2016AGUFM.A43C0239S/abstract

Shin, N.-Y., J.-S. Kug, M. F. Stuecker, F.-F. Jin, A. Timmermann, and G.-I. Kim, 2022: More frequent central Pacific El Niño and stronger eastern pacific El Niño in a warmer climate. *npj Climate Atmos. Sci.*, **5**, 101, https://doi.org/10.1038/s41612-022-00324-9

Stommel, H., 1948: The westward intensification of wind-driven ocean currents. *Eos Trans. Amer. Geophys. Union*, **29**, 202–206, https://doi.org/10.1029/TR029i002p00202

Suarez, M. J., and P. S. Schopf, 1988: A Delayed Action Oscillator for ENSO. *J. Atmos. Sci.*, **45**, 3283–3287, https://doi.org/10.1175/1520-0469(1988)045<3283:ADAOFE>2.0.CO;2

Talley, L. D., 2003: Shallow, Intermediate, and Deep Overturning Components of the Global Heat Budget. *J. Phys. Oceanogr.*, **33**, 530–560, https://doi.org/10.1175/1520-0485(2003)033<0530:SIADOC>2.0.CO;2

Taschetto**,** A. S., C. C. Ummenhofer, M. F. Stuecker, D. Dommenget, K. Ashok, R. R. Rodrigues, and S.-W. Yeh, 2020: ENSO Atmospheric Teleconnections. *El Niño Southern Oscillation in a Changing Climate, Geophys. Monogr. Ser.*, No. 253, Amer. Geophys. Union, 309–335, https://doi.org/10.1002/9781119548164.ch14

Thomsen, S., T. Kanzow, F. Colas, V. Echevin, G. Krahmann, and A. Engel, 2016: Do submesoscale frontal processes ventilate the oxygen minimum zone off Peru?. *Geophys. Res. Lett*., **43**, 8133–8142, https://doi.org/10.1002/2016GL070548

Tippett, M. K., M. Ranganathan, M. L'Heureux, A. G. Barnston, and T. DelSole, 2019: Assessing probabilistic predictions of ENSO phase and intensity from the North American Multimodel Ensemble. *Climate Dyn.*, **53**, 7497–7518, https://doi.org/10.1007/s00382-017-3721-y

Torrence, C., and P. J. Webster, 1998: The annual cycle of persistence in the El Niño/Southern Oscillation. *Quart. J. Roy. Meteor. Soc.*, **124**, 1985–2004, https://doi.org/10.1002/qj.49712455010

Tozuka, T., M. F. Cronin, and H. Tomita, 2017 Surface frontogenesis by surface heat fluxes in the upstream Kuroshio Extension region. *Sci. Rep.* **7**, 10258, https://doi.org/10.1038/s41598-017-10268-3

Tseng, Y.-H., J.-H. Huang, and H.-C. Chen, 2022: Improving the predictability of two types of ENSO by the characteristics of extratropical precursors. *Geophys. Res. Lett.*, **49**, e2021GL097190, https://doi.org/10.1029/2021GL097190

van Heijst, G. J. F., 1985: A geostrophic adjustment model of a tidal mixing front. *J. Phys. Oceanogr.*, **15**, 1182–1190, https://doi.org/10.1175/1520-0485(1985)015<1182:AGAMOA>2.0.CO;2

Vimont, D. J., M. A. Alexander, and M. Newman, 2014: Optimal growth of Central and East Pacific ENSO events. *Geophys. Res. Lett.*, **41**, 4027–4034, https://doi.org/10.1002/2014GL059997

Vimont, D. J., D. S. Battisti, and A. C. Hirst, 2003b: The Seasonal Footprinting Mechanism in the CSIRO General Circulation Models. *J. Climate*, **16**, 2653–2667, https://doi.org/10.1175/1520-0442(2003)016<2653:TSFMIT>2.0.CO;2

Vimont, D. J., J. M. Wallace, and D. S. Battisti, 2003a: The seasonal footprinting mechanism in the Pacific: Implications for ENSO. *J. Climate*, **16**, 2668–2675, https://doi.org/10.1175/1520-0442(2003)016<2668:TSFMIT>2.0.CO;2

Walker, G. T., and E. W. Bliss, 1932: World Weather V. *Mem. Roy. Meteor. Soc*., **4**, 53–84, https://www.rmets.org/sites/default/files/papers/ww5.pdf

Wallace, J. M., and D. S. Gutzler, 1981: Teleconnections in the geopotential height field during the Northern Hemisphere winter. *Mon. Wea. Rev.*, **109**, 784–812, https://doi.org/10.1175/1520-0493(1981)109<0784:TITGHF>2.0.CO;2

Wang, B., X. Luo, Y.-M. Yang, W. Sun, M. A. Cane, W. Cai, S.-W. Yeh, and J. Liu, 2019: Historical change of El Niño properties sheds light on future changes of extreme El Niño. *Proc. Natl. Acad. Sci. U. S. A.*, **116**, 22512–22517, https://doi.org/10.1073/pnas.1911130116

Wang, L., W. Chen, and R. Huang, 2007: Changes in the variability of North Pacific Oscillation around 1975/1976 and its relationship with East Asian winter climate. *J. Geophys. Res.*, **112**, D11110, https://doi.org/10.1029/2006JD008054

Wang, S.-Y., X. Jiang, and B. Fosu, 2015: Global eastward propagation signals associated with the 4–5-year ENSO cycle. *Climate Dyn.*, **44**, 2825–2837, https://doi.org/10.1007/s00382-014-2422-z

Wang, S.-Y., M. L'Heureux, and H.-H. Chia, 2012: ENSO prediction one year in advance using western North Pacific sea surface temperatures. *Geophys. Res. Lett.*, **39**, L05702, https://doi.org/10.1029/2012GL050909

Wang, S.-Y., M. L'Heureux, and J.-H. Yoon, 2013: Are greenhouse gases changing ENSO precursors in the western North Pacific?. *J. Climate*, **26**, 6309–6322, https://doi.org/10.1175/JCLI-D-12-00360.1

Webster, P. J., 2020: Fundamental Processes. In Webster PJ (ed) Dynamics of the Tropical Atmosphere and Oceans, 1st edn, Wiley-Blackwell, New Jersey, pp 79–104.

Webster, P. J., and S. Yang, 1992: Monsoon and ENSO: Selectively interactive systems. *Quart. J. Roy. Meteor. Soc.*, **118**, 877–926, https://doi.org/10.1002/qj.49711850705

Weisberg, R. H., and C. Wang, 1997: A western Pacific oscillator paradigm for the El Niño-Southern Oscillation. *Geophys. Res. Lett.*, **24**, 779–782, https://doi.org/10.1029/97GL00689

Wijffels, S. E., J. M. Toole, H. L. Bryden, R. A. Fine, W. J. Jenkins, and J. L. Bullister, 1996: The water masses and circulation at 10°N in the Pacific. *Deep Sea Res., Part I*, **43**, 501–544, https://doi.org/10.1016/0967-0637(96)00006-4

Wyrtki, K., 1973: Teleconnections in the Equatorial Pacific Ocean. *Sci.*, **180**, 66–68, https://doi.org/10.1126/science.180.4081.66

Wyrtki, K., 1989: Some thoughts about the west Pacific warm pool. *Proc. West. Pac. Int. Meeting and Workshop on TOGA COARE*, Nouméa, New Caledonia, Office de la recherche scientifique et technique outre-mer (ORSTOM), 99–109, https://horizon.documentation.ird.fr/exl-doc/pleins_textes/doc34-08/30199.pdf

Yang, S., and X. Jiang, 2014: Prediction of Eastern and Central Pacific ENSO Events and Their Impacts on East Asian Climate by the NCEP Climate Forecast System. *J. Climate*, **27**, 4451–4472, https://doi.org/10.1175/JCLI-D-13-00471.1

Yeh, S.-W., and Coauthors, 2018: ENSO atmospheric teleconnections and their response to greenhouse gas forcing. *Rev. Geophys.*, **56**, 185–206, https://doi.org/10.1002/2017RG000568

Yeh, S.-W., J.-S. Kug, B. Dewitte, M.-H. Kwon, B. P. Kirtman, and F.-F, Jin, 2009. El Niño in a changing climate. *Nat.*, **461**, 511–514, https://doi.org/10.1038/nature08316

Yeh, S.-W., J.-S. Kug, and S.-I. An, 2014: Recent progress on two types of El Niño: Observations, dynamics, and future changes. *Asia-Pac. J. Atmos. Sci.*, **50**, 69–81, https://doi.org/10.1007/s13143-014-0028-3

Yu, J.-Y., and H.-Y. Kao, 2007: Decadal changes of ENSO persistence barrier in SST and ocean heat content indices: 1958–2001. *J. Geophys. Res.*, 112, D13106, https://doi.org/10.1029/2006JD007654

Yu, J.-Y., and S. T. Kim, 2010: Identification of central-Pacific and eastern-Pacific types of ENSO in CMIP3 models. *Geophys. Res. Lett.*, **37**, L15705, https://doi.org/10.1029/2010GL044082

Yu, J.-Y., and S. T. Kim, 2011: Relationships between Extratropical Sea Level Pressure Variations and the Central Pacific and Eastern Pacific Types of ENSO. *J. Climate*, **24**, 708–720, https://doi.org/10.1175/2010JCLI3688.1

Yu, Y., W, Duan, H. Xu, and M. Mu, 2009: Dynamics of nonlinear error growth and season-dependent predictability of El Niño events in the Zebiak–Cane model. *Quart. J. Roy. Meteor. Soc.*, **135**, 2146–2160, https://doi.org/10.1002/qj.526

Zebiak, S. E., 1989: On the 30–60 Day Oscillation and the Prediction of El Niño. *J. Climate*, **2**, 1381–1387, http://www.jstor.org/stable/26196384

Zhang, L., P. Chang, and L. Ji, 2009: Linking the Pacific Meridional Mode to ENSO: Coupled Model Analysis. *J. Climate*, **22**, 3488–3505, https://doi.org/10.1175/2008JCLI2473.1

Zhao, Y., Y. Jin, J. Li, and A. Capotondi, 2022: The role of extratropical Pacific in crossing ENSO spring predictability barrier. *Geophys. Res. Lett*., **49**, e2022GL099488, https://doi.org/10.1029/2022GL099488

Zhou, H., X. Liu, and P. Xu, 2019: Sensitivity of Sverdrup transport to surface wind products over the tropical North Pacific Ocean. *Ocean Dynamics*, **69**, 529–542. https://doi.org/10.1007/s10236-019-01260-8

Zhou, H., D. Yuan, L. Yang, X. Li, and W. Dewar, 2018: Decadal Variability of the Meridional Geostrophic Transport in the Upper Tropical North Pacific Ocean. *J. Climate*, **31**, 5891–5910. https://doi.org/10.1175/JCLI-D-17-0639.1

CHAPTER 4

ON TANZANIA'S PRECIPTIATION CLIMATOLOGY, VARIABLITY, AND FUTURE PROJECTION

4.1 Abstract

This chapter investigates historical and projected precipitation in Tanzania using observational and climate model data. Precipitation in Tanzania is highly variable in both space and time due to topographical variations, coastal influences, and the presence of lakes. Annual and seasonal precipitation trend analyses from 1961 to 2016 show maximum rainfall decline in Tanzania during the long rainy season in the fall (March–May), and an increasing precipitation trend in northwestern Tanzania during the short rainy season in the spring (September–November). Empirical orthogonal function (EOF) analysis applied to Tanzania's precipitation patterns shows a stronger correlation with warmer temperatures in the western Indian Ocean than with the eastern-central Pacific Ocean. Years with decreasing precipitation in Tanzania appear to correspond with increasing sea surface temperatures (SST) in the Indian Ocean, suggesting that the Indian Ocean Dipole (IOD) may have a greater effect on rainfall variability in Tanzania than the El Niño-Southern Oscillation (ENSO) does. Overall, the climate model ensemble projects increasing precipitation trend in Tanzania that is opposite with the historical decrease in precipitation. This observed drying trend also contradicts a slightly increasing precipitation trend from climate models for the same historical time period, reflecting challenges faced by modern climate models in representing Tanzania's precipitation.

4.2 Introduction

In Africa, the change in precipitation extremes affects agriculture and industries that either directly or indirectly rely on the replenishment of water resources. Many studies have identified a widespread decline in precipitation in several eastern and southern African countries and these trends were linked to global warming [1–3]. Major water-related threats to Africa's geographic landmarks include melting of snow caps on Mt. Kilimanjaro in Tanzania [4], receding water levels of Lake Victoria in Tanzania, Kenya, and Uganda [5], and decreasing river flow of the Victoria Falls in Zambia and Zimbabwe [6]. Droughts have become more frequent, longer, and more severe in the last two decades, particularly the 2010–2011 East African drought when famine plunged several countries into a humanitarian crisis. This observed drying trend contradicts a projected increase in East African rainfall by climate models [2,7–9]. However, in recent years, East African countries have been plagued by frequent floods that have displaced many people and claimed lives [10]. Further analysis is necessary to understand the seemingly contradictory precipitation trends experienced in East Africa during the recent years.

In this study, we focused on Tanzania and explored the historical and projected precipitation trends in the country. Tanzania lies just south of the equator between the East African Great Lakes and the Indian Ocean. Although precipitation extremes affect Tanzania's livelihood, natural resources, and ecosystems, the future of its climate regime remains uncertain. This drawback is largely due to the shortage of in situ observations, and inconsistencies between observations and climate model simulations. Studies on East African climatology show that mean elevation has a greater effect on the frequency of rainfall than the amount of rainfall [11]. Indeed, topographic differences contribute to regional rainfall variations throughout Tanzania. Elevation increases from coast to inland and is highest in the Southern Highlands in Iringa and Mbeya, and in northeastern Tanzania in Arusha, Kilimanjaro, and Tanga (Figure 1a,b). Average annual rainfall distribution in Tanzania is unimodal (Figure 1c) and is influenced by the movement of the

Intertropical Convergence Zone (ITCZ). The ITCZ reaches south of Tanzania in December before retreating north in January until it is furthest from Tanzania in June-July-August (JJA). The peak rainy season in Tanzania is in December-January-February (DJF), followed by a gradual decline in March-April-May (MAM), before the dry season in JJA (Figure 1c). Modes of large-scale climate variability of oceanic origins are also reported to contribute to variations in Tanzania's precipitation patterns [12–16].

Although considerable research has been done on East African climate, the lack of consensus on dominant modes of climate variability and conflicting past and future precipitation trends calls for re-examination of Tanzania's precipitation patterns. We present a semi-review paper with new analysis to update literature on Tanzania's climate and trends. We conducted annual and seasonal climatology and regional analysis within Tanzania using gridded data and compared the results of this chapter to those of previous studies that focus on East Africa (e.g., [15]). We apply the updated climatology for further examination of variability and trends that are not yet satisfactorily addressed for Tanzania. Section 2 presents the datasets and methods used in this study. Section 3 discusses the results with interpretations and how they compare to findings from other studies. Section 4 presents conclusions derived from this study.

4.3 Materials and Methods

Observational data used in this study are the 0.25º Global Precipitation Climatology Centre (GPCC) monthly precipitation data provided by the NOAA/OAR/ESRL PSD, Boulder, Colorado, USA, from their website at https://www.esrl.noaa.gov/psd/ [17,18]. GPCC data from 1901 to 2016 are derived from 67,200 quality-controlled global stations [17,18] with a minimum observation of 10 years [19]. The quality of GPCC data with respect to Tanzania's domain is discussed in the supplementary material. GPCC datasets have high resolution over extended periods that allow for more robust precipitation analyses such as trend and climatological analyses, comparison with climate model simulations, and drought monitoring. For topography, we used the 1-arc-minute

shaded relief data from ETOPO1 Global Relief from the National Geophysical Data Center (NGDC) of the National Oceanic and Atmospheric Administration (NOAA; [20]) using bathymetric, topographic, and shoreline data from numerous global and regional digital datasets.

GPCC precipitation datasets were used to perform annual and seasonal trend analyses and empirical orthogonal function (EOF) analysis to study spatial patterns of climate variability and how they change with time [21,22]. EOF analyzes space-time datasets by reducing the data to spatial patterns known as EOFs that explain most of the data, and temporal patterns known as principal components (PC; [23]) that can be correlated with other variables [24]. We applied EOF analysis on annual precipitation in Tanzania during 1961–2016 to explore spatial variations in precipitation patterns and used the principal components of precipitation from EOF analysis to explore the temporal variations of the leading precipitation patterns. Additionally, monthly Sea Surface Temperature (SST) dataset of 2^{o} resolution was derived from NOAA's extended reconstructed SST (ERSST, version 5; [25]). The SST dataset was used to assess remote climate influences (i.e., teleconnections) of persistent ocean temperature anomalies on regional precipitation patterns by correlating the principal components from the EOF analysis with the SST anomalies.

Reanalysis data are compilations of meteorological data spanning extended time scales (decadal to centennial) from various sources (e.g., rain gauge, remote sensing, radiosonde etc.) that maximize available information and resolution of the data by using numerical weather forecast and data assimilation techniques. Reanalysis data for 850-hPa temperature, winds, and relative humidity of 2.5^{o} resolution were obtained from the National Centers for Environmental Prediction/National Center for Atmospheric Research (NCEP/NCAR) Reanalysis 1 (R1; [26]). Low-level 850-hPa winds and relative humidity were used to study annual and seasonal climatology of the atmospheric circulation patterns over Tanzania.

To understand climate change caused by natural variability or changes in radiative forcings, climate model outputs need to be analyzed collectively for the examination of future climate

projections [27,28]. Coupled Model Intercomparison Project (CMIP) is a collaborative effort that set protocols to improve climate models by comparing model simulations under similar scenarios to each other and to observations [29]. Climate model simulations for historical and projected precipitation were downloaded from the CMIP5 server at http://climexp.knmi.nl/ [30]. The annual extremes of daily CMIP5 data are from ETCCDI extreme indices archive at the Canadian Center for Climate Modelling and Analysis [31,32]. Each CMIP5 model was based on anthropogenic forcing of the representative concentration pathway 8.5 (RCP8.5; [33,34]) to study extreme scenario. Historical precipitation time series were derived from 44 ensembles of CMIP5 data from 1861 to 2005 and from 2006 to 2100 for future projections.

4.4 Results

4.4.1. Climatology

The climatology of Tanzania's precipitation is heterogeneous across the country due to complexities related to combined large-scale effects of topography, winds, humidity, and dynamics of tropical circulation; therefore, it is important to revisit and examine the climatological features of precipitation. Seasonality of rainfall along coastal areas is different than further inland, and annual precipitation is higher near coasts (Figure 2a–e). Annual precipitation climatology shows maximum cumulative rainfall in southwestern Tanzania while the central region receives the lowest rainfall in the country (Figure 2a). Two high precipitation centers are localized over the Southern Highlands: one over Morogoro and Iringa, and another over Mbeya to the north of Lake Malawi (Figure 2a). Other precipitation centers occur in northwestern Tanzania over Kigoma, Kagera, and western Lake Victoria, and in northeastern Tanzania over Tanga and Kilimanjaro (Figure 2a). Seasonal climatology reveals that most of the annual rainfall occurs between December and May, with varying spatial distribution from DJF to MAM (Figure 2b,c). Southern and western to central Tanzania receive maximum seasonal rainfall in DJF whereas northern and eastern Tanzania receive

maximum seasonal rainfall in MAM (Figure 2b,c). In JJA, precipitation is uniformly distributed among regions and does not typically exceed 100 mm (Figure 2d). In the spring of September-October-November (SON), northwestern Tanzania receives the most rainfall in the country (Figure 2e).

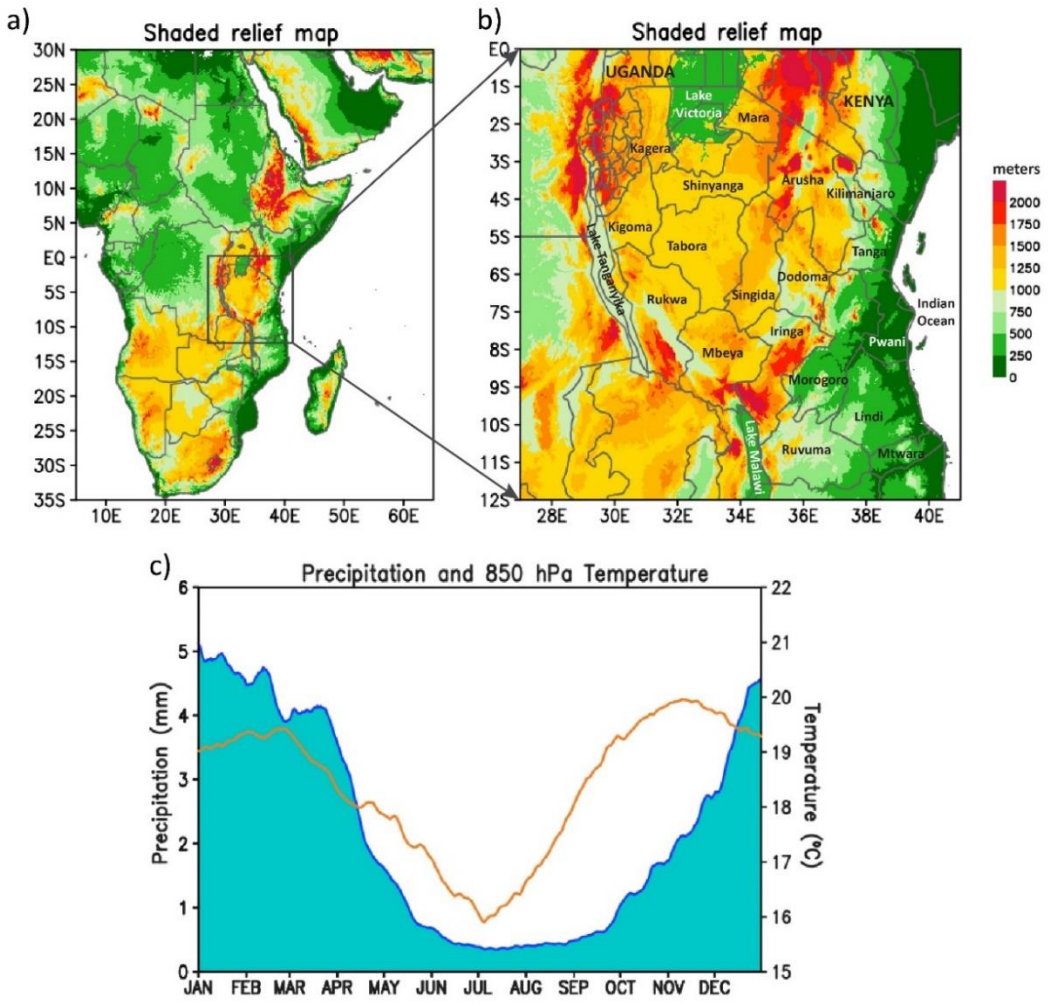

Figure 1. Shaded relief (m) maps of (**a**) Africa and (**b**) Tanzania from ETOPO1. (**c**) 10-day running mean (1981–2010) precipitation (mm) for Tanzania (0–15S, 30–40E) (shaded in blue), and 850-hPa temperature (°C, orange curve). The 850-hPa temperature data are taken from the Reanalysis 1 (R1) data archive.

An important point of note here is that Tanzania's precipitation patterns in the southern and central parts do not coincide with those of its East African counterparts in southern Uganda and central to southwestern Kenya (Figure 2a–e), where rainfall distribution is bimodal, i.e., with

prolonged rains in MAM when the ITCZ moves northward slowly, and a brief rainy season in SON when the ITCZ moves southward. Distinct high precipitation centers occur in southern Uganda and central to southwestern Kenya just north of Tanzania in MAM and SON (Figure 2a–e). Eastern Kenya is also slightly wetter in MAM than the rest of the year (Figure 2a–e). For bimodal rainfall distribution in East Africa, the precipitation centers are stronger in MAM than SON (Figure 2a–e). As the ITCZ does not linger over southern and western to central Tanzania in the austral spring, SON rainfall is low, and a significant precipitation increase is not observed until December. This yields a more unimodal distribution influenced by position of the ITCZ over southern Tanzania where the rainfall period lasts approximately six months (Figure 2b–e). However, northern Tanzania has a bimodal rainfall distribution similar to Kenya and Uganda (Figure 2b–e), as the ITCZ crosses over the region twice a year. Low-level tropospheric temperatures in Tanzania reflect both precipitation regimes. The 850-hPa air temperature reaches its annual maximum in November before the end of the short rainy season, followed by a slight cooling in December, and peaks again in late February before the onset of the prolonged rainy season (Figure 1c). The 850-hPa air temperature (Figure 1c) reaches its annual minimum in July during the peak of the dry season; the 850-hPa level is about 1500 m above sea level and is therefore representative of the air temperature over the complex terrains.

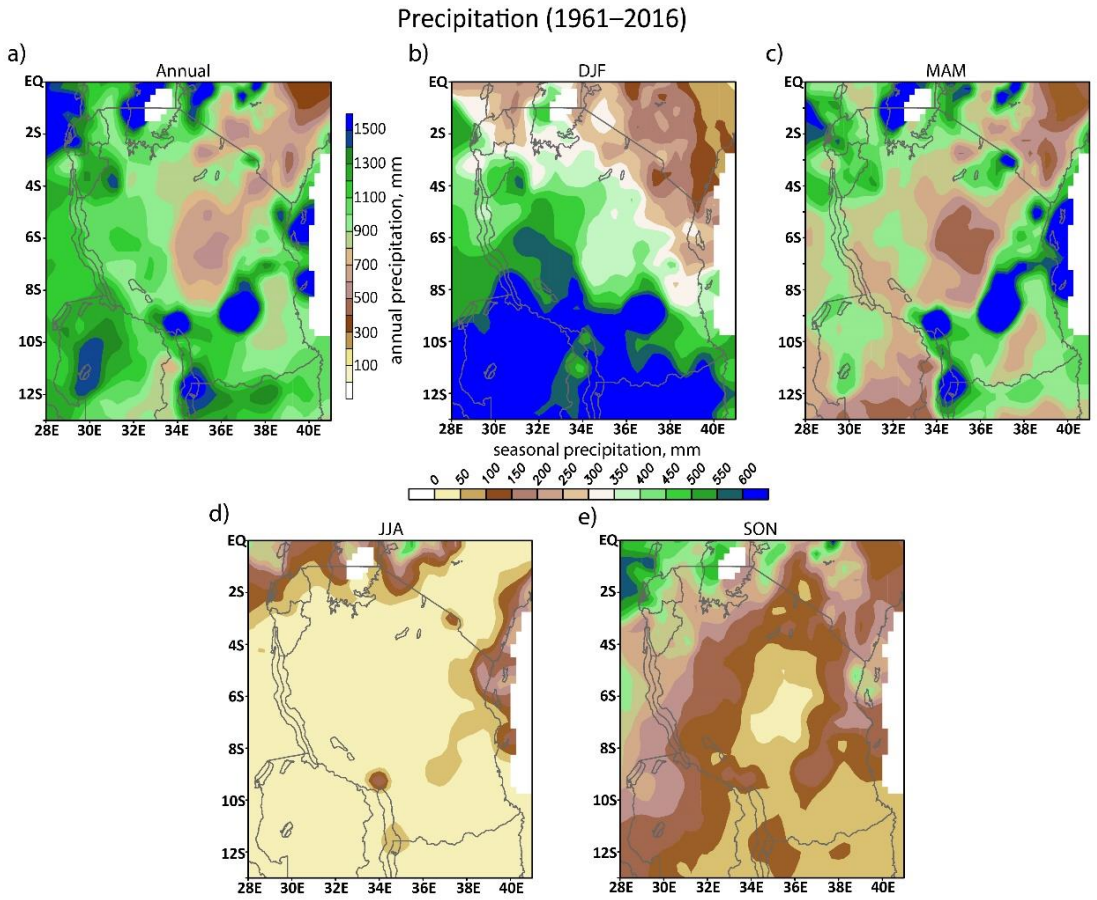

Figure 2. Annual and seasonal precipitation climatology calculated from 1961–2016 Global Precipitation Climatology Centre (GPCC) precipitation data. (**a**) Annual precipitation, (**b**) Dec–Feb summer precipitation, (**c**) Mar–May fall precipitation, (**d**) Jun–Aug winter precipitation, and (**e**) Sep–Nov spring precipitation. Precipitation is in mm.

Low-level atmospheric circulation and relative humidity patterns over Tanzania vary considerably throughout the year (Figure 3a–e). Due to Tanzania's close proximity to the equator, its climate is shaped by trade winds that are controlled by the position of the ITCZ [35]. The three major air streams that affect circulation patterns and distribution of moisture in Tanzania are the northeasterly trade winds, the southeasterly trade winds, and the westerly Congo air [36]. The trade winds are associated with a subsiding motion and are relatively dry while the Congo air is moist and unstable. In the austral summer, when the ITCZ is south of Tanzania, the northeasterly trade winds that are parallel to the Great Horn of Africa diverge along the coastal areas of Tanzania and converge with low-level moisture fluxes from the southern Congo Basin over Lake Tanganyika

(Figure 3b). In the austral winter, when the ITCZ is north of Tanzania, the southeasterly trade winds diverge into two different directions (Figure 3d), with one towards western Tanzania and the other northward along the Somali coast (Figure 3d). Coastal areas are drier where northeasterly and southeasterly trade winds are parallel to the coastline because friction between the coast and the water causes subsidence [37]. Coastal aridity is further enhanced by presence of the rift valley system that blocks the warm moist Congo air from reaching the Tanzania shorelines [36].

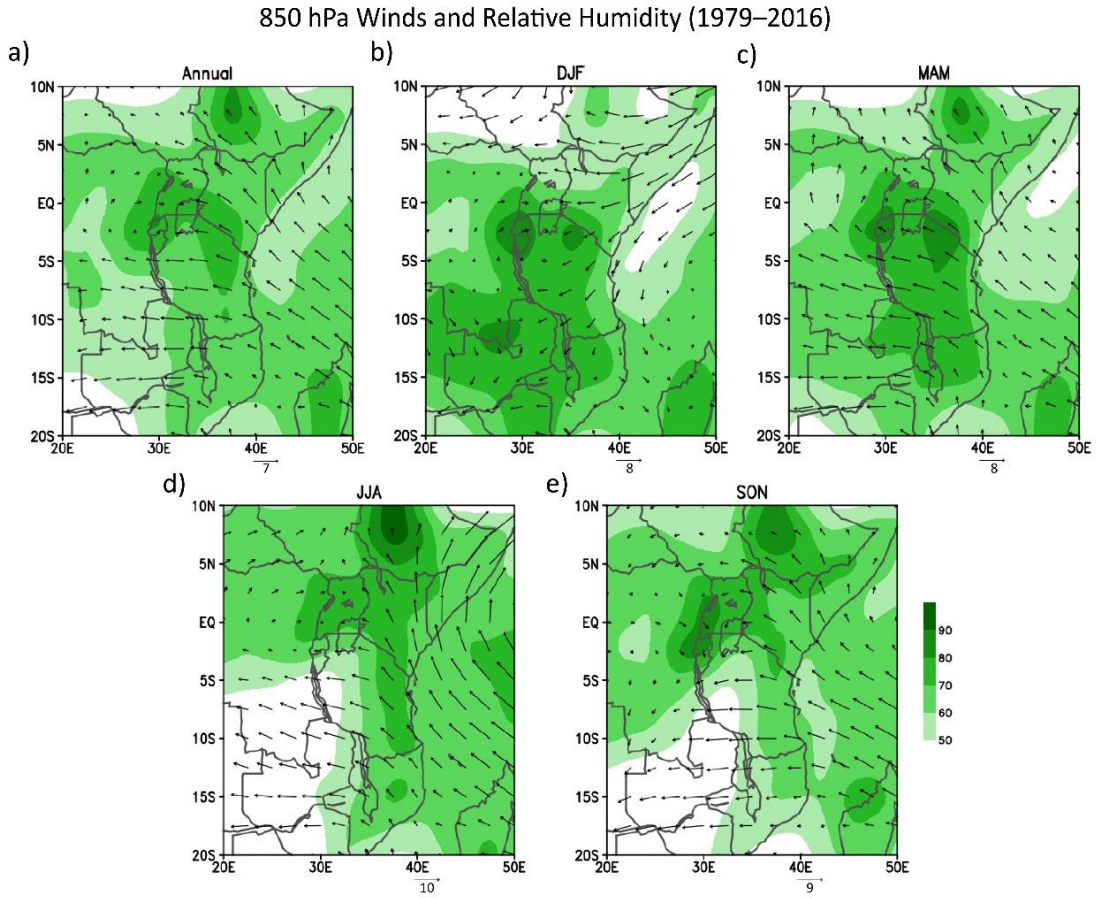

Figure 3. Annual and seasonal 850-hPa winds (vectors) and relative humidity (shaded) climatology calculated from 1979–2016 Reanalysis 1 (R1) data. (**a**) Annual patterns, (**b**) Dec–Feb summer patterns, (**c**) Mar–May fall patterns, (**d**) Jun–Aug winter patterns, and (**e**) Sep–Nov spring patterns. Winds are in m/s. Relative humidity is expressed as percent.

Tanzania's precipitation is also influenced by local circulation patterns along coastal areas and around large lakes [38]. Lake Victoria is reported to affect the regional distribution, diurnal cycles, and seasonal variation in precipitation in northern Tanzania [39,40]. Total precipitation for

Lake Victoria comes from nocturnal rains over the western lake surface and afternoon rains over the eastern lake surface [39]. Most of the rainfall is controlled by the nocturnal component of land-breeze circulation when the land surface becomes cooler than the lake surface [40–42]. The associated convergence and thermal instability produce mesoscale convective systems over the central and western lake surface, and lasts several hours [39]. Prevailing easterly winds ensure that the thunderstorm clusters associated with the convergence are centered over the western and central part of the lake during the mature stage [39]. As a result, most of the Lake Victoria's rainfall occurs over the western part of the lake (Figure 2a–e), and at night during storm activity. This circulation pattern occurs approximately 175 days a year [43] and generates 80% of the water source for the lake [5]. Although Lake Victoria's water levels are receding [5], future projections predict an increase in intense thunderstorms and extreme precipitation over the lake [44].

4.4.2. Trends

Trend analysis for rainfall accounts for the long-term change in precipitation, and provides information about precipitation patterns and variability [45]. An overall decreasing annual precipitation trend is observed in Tanzania from 1961 to 2016 (Figure 4a). This negative trend is strongest and expansive for the Southern Highlands in Lake Malawi, Ruvuma, and southern Iringa, and near coastal areas in Tanga, Dar-es-Salaam, Morogoro, and Pwani (Figure 1b and Figure 4a). Other strong negative trends are localized in Rukwa and Tabora in western Tanzania, and western Lake Victoria (Figure 1b and Figure 4a) where water levels dropped significantly in recent years [5,46]. In northeastern Tanzania, Arusha and Mara just east of Lake Victoria yield a moderately decreasing annual precipitation trend (Figure 4a). The rest of Tanzania experienced either a very slight increase or no significant change in precipitation (Figure 4a).

Seasonal precipitation trends in Tanzania reveal eminently decreasing precipitation in coastal areas throughout the year (Figure 4b–e). In DJF, the negative trend is strongest in the Southern Highlands and coastal areas, and the positive trend is strongest for central Tanzania in

Tabora, Singida, and northern Iringa (Figure 4b). DJF rainfall is also suppressed in western Tanzania, western Lake Victoria, and Mara (Figure 4b). A drying trend in MAM is evident from negative anomalies throughout the country, particularly in the Southern Highlands (Figure 4c). The MAM precipitation trend resembles the annual precipitation trend more closely than other seasons (Figure 4a-e), indicating that the overall drying trend in Tanzania is largely a result of extreme negative anomalies during the long rains season. MAM is the only season in which the most of precipitation in Tanzania exhibits a significant trend; this is consistent with previous studies on East Africa that show the greatest negative rainfall departures in MAM [1,7,8,15,47–52]. All other seasons either show a locally significant trend or do not reveal any significant change in the long run. In JJA, the negative trend is strongest near coastal areas, and a positive trend is apparent in central to northwestern Tanzania (Figure 4d). In SON, a general decreasing trend is observed throughout Tanzania with exception of the northwestern regions where precipitation increased i.e., wet areas became wetter and dry areas became drier (Figure 4e). Lake Victoria experienced an increasing trend during the short rains season (Figure 4e). Interestingly, although East African annual rainfall has declined in the past three decades, precipitation during the short rains season has increased [1,16].

4.4.3. Variability

The EOF analysis was used to study spatial and temporal patterns of seasonal precipitation from 1961 to 2016. The first four modes of EOF explain 55% of the variation of annual precipitation in Tanzania. The first mode of EOF (EOF1) of annual precipitation corresponds to the climatology (Figure 5a) and the second mode of EOF (EOF2) of annual precipitation closely resembles the annual precipitation trend (Figure 5b). EOF1 shows positive anomalies throughout Tanzania and explains 34% of the total variation (Figure 5a). EOF2 shows negative anomalies over southern Tanzania and explains 10% of the total variation (Figure 5b). The positive anomalies of EOF1 reflect the decreasing trend in PC1 (Figure 5a,e). The anomalies of EOF2 reflect the multi-decadal

increase in PC2 from 1961 to 1997, followed by a decrease from 1998 to 2016 (Figure 5b,f). EOF3 shows the decreasing precipitation with 7% variance over the eastern part of the country in coastal region (Figure 5c) while PC3 does not show any trend (Figure 5g). EOF4 also shows both increasing trend and precipitation with only 4% of the variance (Figure 5d), however PC4 shows the increasing trend (Figure 5h). Additionally, we also looked the seasonal precipitation EOF, focusing on summer rainfall (December to May); the distribution is similar to the annual precipitation (result not shown).

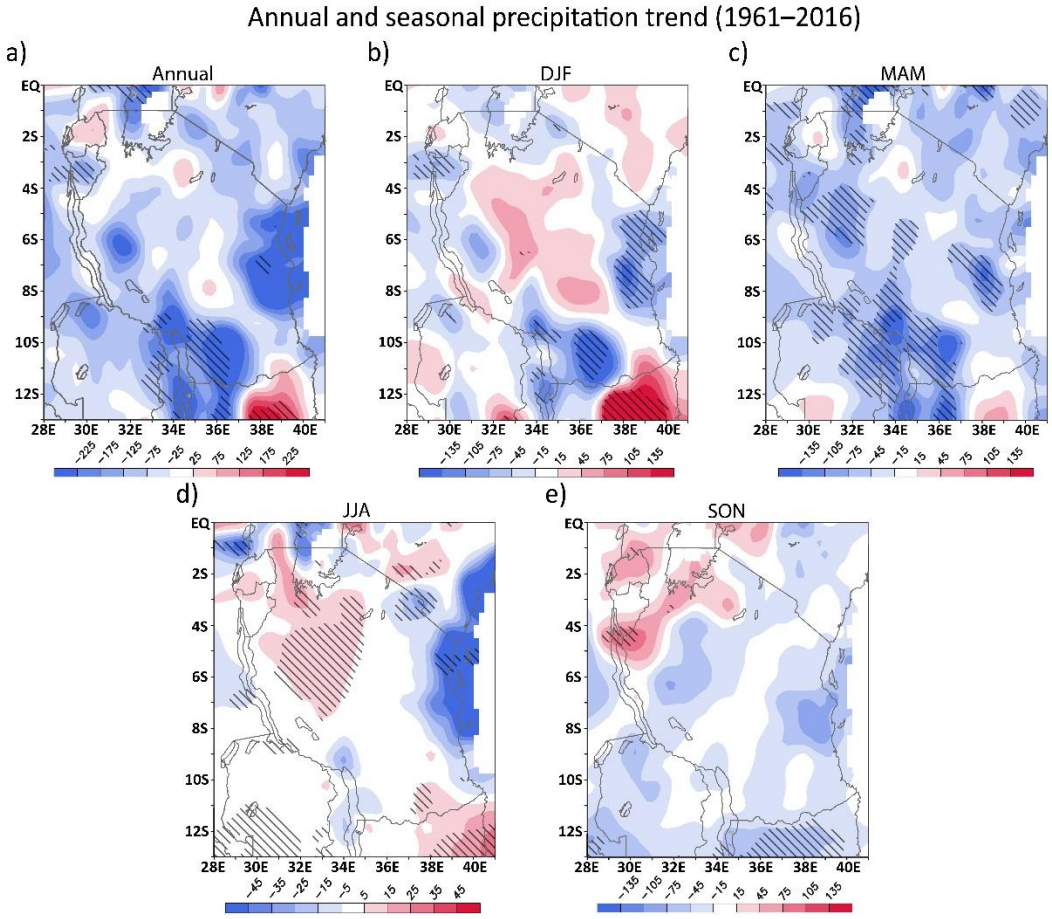

Figure 4. Annual precipitation trend (slope*total number of years) in Tanzania calculated from 1961–2016 Global Precipitation Climatology Centre (GPCC) observations. Precipitation trend are plotted during different season with (**a**) annual precipitation trend, (**b**) Dec–Feb precipitation trend, (**c**) Mar–May precipitation trend, (**d**) Jun–Aug precipitation trend, and (**e**) Sep–Nov precipitation trend. Hatched areas indicate significant values with confidence level > 90%. Precipitation is in mm.

Comparison of the principal components of precipitation time series with global SSTs over the study period 1961-2016 stresses the effects of ocean forcings on Tanzania's climate (Figure 6). We detrended both variables (PCs and SSTAs) first before constructing the correlation maps of Figure 6 to better depict the interannual variations. The first mode of precipitation is linked to SST variability over the eastern and western Indian Ocean in an opposite manner (Figure 6a), a pattern characteristic of the Indian Ocean Dipole (IOD). Pattern of PC1 correlation with SST shows correlations in the eastern Indian Ocean and western Pacific (Figure 6a), however the correlation is not significant after detrend. PC2 shows a positive yet insignificant correlation with the El Niño-Southern Oscillation (ENSO) pattern, similar to that found by Mazzarella et al. [53], albeit weaker (Figure 6b). PC3 is related to reduced precipitation over the east coast of Tanzania (Figure 5c,g) in association with increased SST in the Arabian Sea and the western Pacific Ocean (Figure 6c). This suggests that when SSTs in the western Pacific Ocean increase, precipitation in eastern Tanzania decreases while precipitation over western Tanzania increases. Finally, PC4 shows strong correlation with increased Indian Ocean and eastern Pacific temperature (Figure 6d). However, PC4 shows increasing trend (Figure 5h) with no significant precipitation change over Tanzania (Figure 5d), indicating that warmer ocean (Indian and Pacific Oceans) may not directly alter precipitation patterns in Tanzania.

Various modes of climate variability have been proposed as possible drivers of interannual and intraseasonal variability of East African rainfall. Some studies link the recent drying trend to changes in SSTs in the tropical Pacific basin [2,49,50]. Lyon and Vigaud [15] show that the decline in MAM rains in East Africa started in 1999 and link the timing of the abrupt shift to the Pacific Decadal Variability (PDV). Wainwright et al. [54] believe that the drying trend is caused by shortening of the MAM rainy season due to more rapid movement of the ITCZ rather than simply decreasing rainfall amounts. They attribute the faster migration of the ITCZ to an increasing pressure gradient caused by the warming SSTs to the north in the Arabian Sea in JJA, and to the south near Madagascar in DJF. Others argue that an increasing east-west SST gradient in the

western Pacific intensifies the Walker circulation over the Indian Ocean and enhances subsidence over East Africa [1,55,56], a finding that coincides with the SST correlation analysis with PC1 in Figure 6a. Other remote forcings have also been investigated as possible drivers of East African rainfall variability [57,58]. However, the two most dominant modes of climate variability proposed for East Africa are ENSO [12] and IOD [59,60], which appear to be the case for Tanzania as well.

Numerous studies show that ENSO affects rainfall variability over many parts of the world, including East Africa. Although maximum rainfall for East Africa occurs in MAM, interannual variability of East African rainfall is greater during the short rains period than the long rains period [36,61,62]. Rainfall distribution is also more spatially coherent throughout Tanzania in SON than MAM [36,63], particularly during the peak of the spring rainy season [64]. Spatial rainfall anomaly patterns in May differ from those in March and April, and spatial coherence is stronger for March than April [65]. These seasonal and intraseasonal contrasts are attributed to ENSO which is more intense in OND than MAM. East African rainfall anomalies in OND are positive during El Nino years and negative during La Nina years [14,66,67]. ENSO is either strongly positive or strongly negative in OND but shifts between positive and negative phases in MAM as it gets weaker towards the end of the event [68].

Adding to the above studies, the results in this chapter show that the Indian Ocean SST also exerts a marked influence on Tanzania's precipitation, especially on its long-term trend (Figure 6b). Although ENSO has some effect on climate variability in East Africa [12,69], this association is weak in Tanzania and demonstrates considerable spatial variability [60,67,70,71]. Atmospheric general circulation models (AGCM) indicate that Indian Ocean SSTs have a greater effect on the East African rainfall than SSTs in other oceans [72–75]. Various studies show that the interannual variability of short rains in East Africa is modulated by the IOD as it reaches its peak intensity in SON [76,77]. The increased rainfall during the short rains season is linked to positive IOD events when the western Indian Ocean is warmer than the eastern Indian Ocean [77,78]. This temperature contrast weakens the Walker circulation over the Indian Ocean and reduces subsidence over East

Africa [59]. Precipitation is further enhanced by subsequent lowering of mean sea-level pressures over the western Indian Ocean, which allows westerly moisture fluxes from the Congo Basin to converge with easterly moisture fluxes from the Indian Ocean [78].

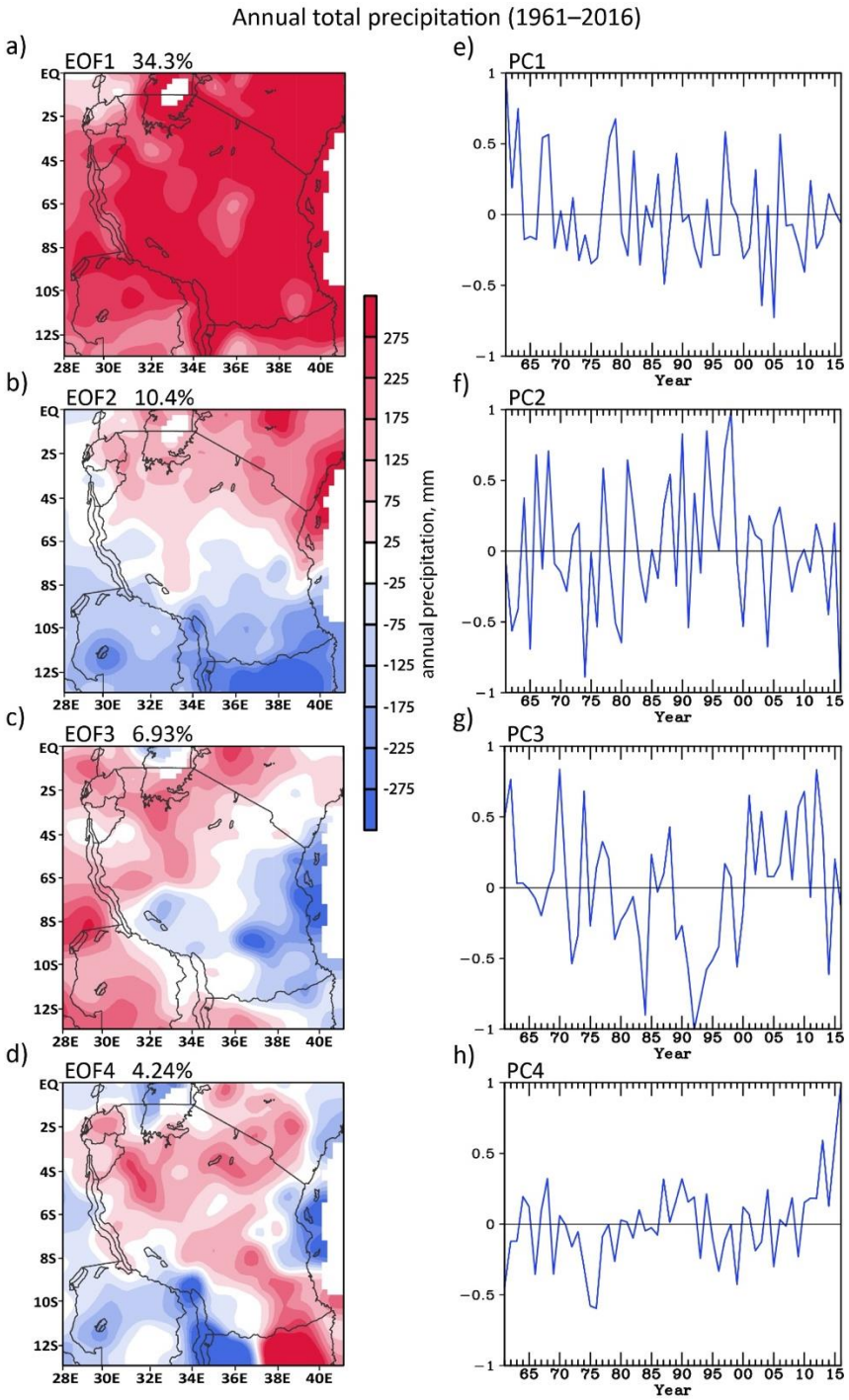

Figure 5. (**a**–**d**) First four modes of empirical orthogonal function (EOF) of annual precipitation over Tanzania and with their respective (**e**–**h**) principal components. Precipitation data are from Global Precipitation Climatology Centre (GPCC) for the period of 1961–2016. Precipitation is in mm.

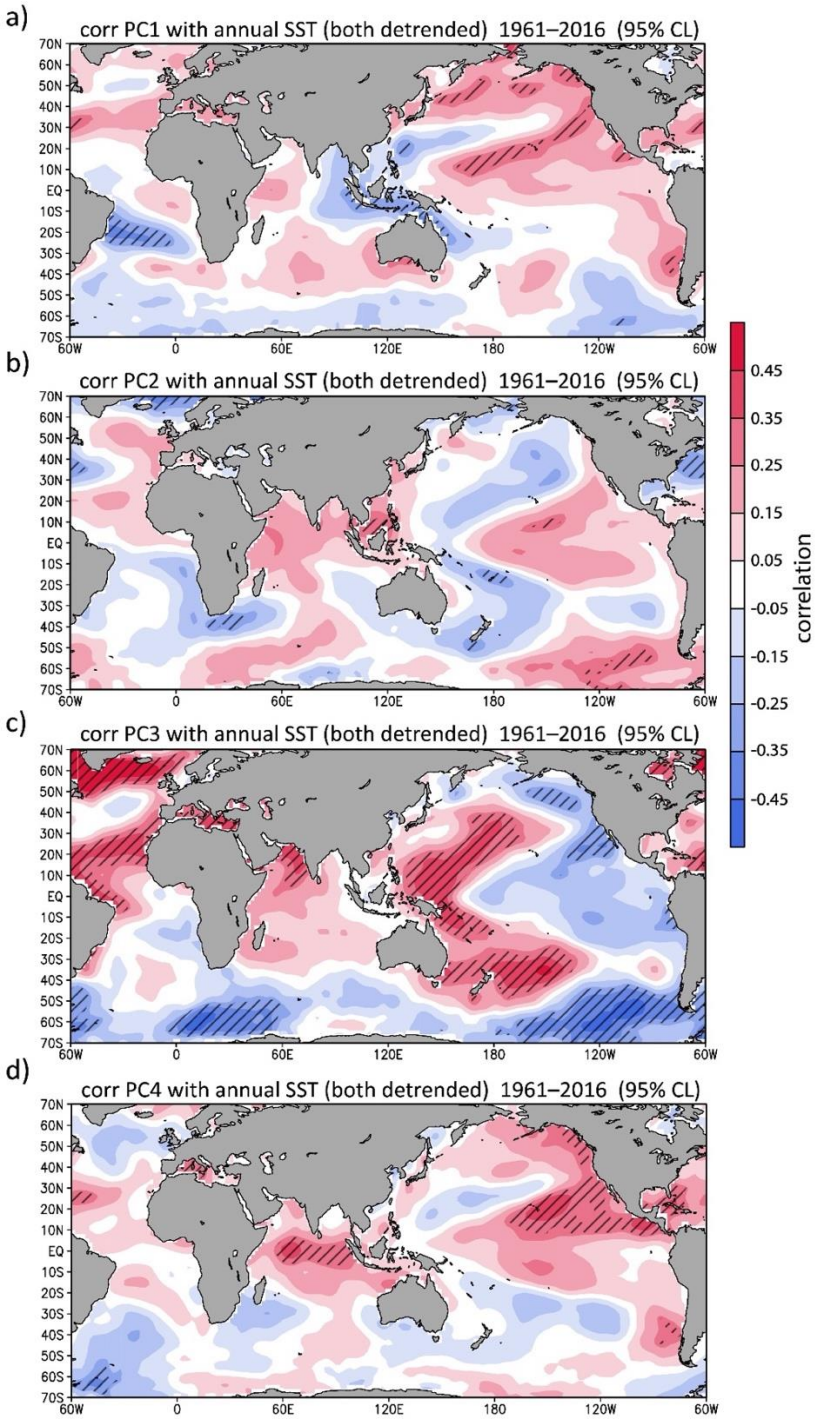

Figure 6. Temporal correlation of annual precipitation principal component (PC) to annual sea surface temperature (SST) for the 1961–2016 period. Both variables are detrended. (**a**) PC1 correlation with SST, (**b**) PC2 correlation with SST, (**c**) PC3

correlation with SST, and (**d**) PC4 correlation with SST. Hatched areas indicate significant values with confidence level > 95%.

4.4.4. Projected change

The historical precipitation trend for the entire domain of Tanzania shows a slightly increasing trend from 1860 to 2005 punctuated with short periods of decreasing rainfall (Figure 7). The projected precipitation trend for the same region shows a more significant increase in precipitation from 2005 to 2100 (Figure 7). This increasing trend is consistent with future projections from other studies that consider scenarios with maximum radiative forcings for rainfall projections in East Africa (e.g., [15]). With the global temperature rising, evaporation rates would increase and moisture is retained in the atmosphere over longer periods which can exacerbate drought [79]. Eventually, water in the saturated atmosphere condenses and produces heavy rainfall [80–82]. As the long-term response to anthropogenic warming from climate model projections is increasing rainfall for Tanzania, the recent decline in East African rainfall is likely a consequence of lower-frequency natural climate variability superimposed on anthropogenic global warming.

The observational data in this study vary from the climate model data in that they display opposite annual precipitation trends (Figure 8). GPCC data show a general decreasing trend while CMIP5 data show a general increasing trend (Figure 8). However, both datasets capture decadal variability and follow similar trends from 1980 to 2000 and to a lesser degree from 2004 to 2016 (Figure 8). Interactions between global warming and natural variability modes can affect regional precipitation trends [83]. Modes of variability are fluctuations in atmospheric and climate conditions that can occur at a range of time scales and exhibit different characteristics such as periodicity, gradual trends, sudden shifts, and positive vs. negative trends [84]. Instrumental records of climate variables include influences of both natural variability and anthropogenic forcings. Natural variability modes are reported to dampen the effects of anthropogenic warming by redistribution of heat in the climate system [85–88]. The results in this chapter indicate that the

natural variability signals in the precipitation trend for Tanzania likely result from superimposition of IOD events and ENSO phases combined. However, with intensification of global warming and the water cycle, the influence of natural variability on the long-term precipitation variation can be overtaken by anthropogenic forcings [89,90].

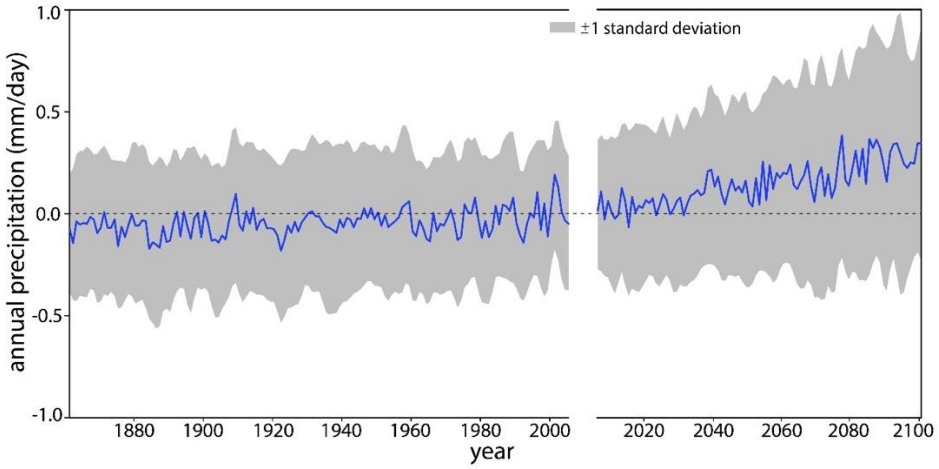

Figure 7. Annual average Coupled Model Intercomparison Project (CMIP) precipitation over Tanzania (2–12S, 30–40E) from CMIP5 simulation. Data from all 44 members are considered to calculate the average precipitation (blue line) and shaded area shows the ± 1 standard deviation calculated from all members. Anomalies in mm/day are calculated based on the average value from 1971–2000.

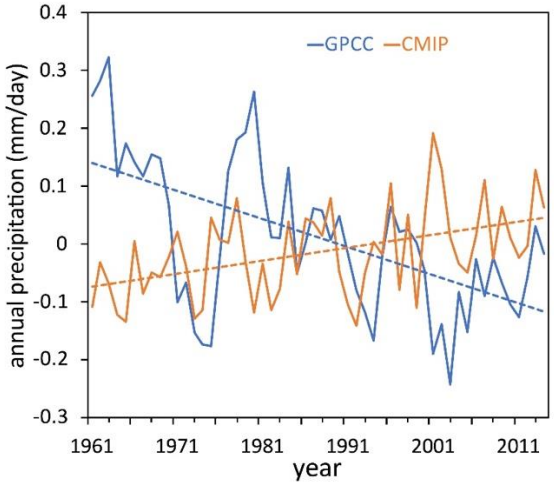

Figure 8. Annual precipitation over Tanzania for the 1961–2014 period from observations (orange line: Global Precipitation Climatology Centre (GPCC) 5-year running average) and from climate model (blue line: Coupled Model Intercomparison Project 5 (CMIP5) 44 ensembles average). Dashed lines show the trend of precipitation during that period. Both datasets show significant trend (95% confidence level) however

observations show decreasing precipitation trend while climate model show increasing trend. Both datasets capture the decadal variability and show better agreement for the later period (~ after 1980). Anomalies in mm/day are calculated based on the average value from 1971–2000.

The inconsistencies in the overall precipitation trend raise questions about the reliability of climate models for future projections. Although significant progress has been made to study extreme events, such events are characterized by the tail ends of probability distribution curves and involve higher-order statistics that are difficult to represent in climate models, especially at longer time scales [91]. Dominant sources of uncertainties in climate models depend on the variable of interest. The robustness of a prediction is indicated by the signal-to-noise ratio (S/N) which is higher for temperature than precipitation [92]. Parametric and structural uncertainties are also much larger for precipitation than temperature. Moreover, cloud and precipitation processes occur at scales too small for coarse resolution models to explicitly resolve [93–95]. Internal variability also affects the S/N for precipitation and is reported to account for most of the uncertainty in regional precipitation simulation [91,92]. Parametric and structural uncertainties resulting from the complexities of modeling precipitation can affect both the magnitude and direction of the projected change in precipitation [92]. These uncertainties are especially large in the tropics [91,96,97] where largest precipitation change is projected [98–104] and the S/N for precipitation is lowest [92], a case that is likely applicable to Tanzania. In short, biases and diverged internal variations in climate models could alternate the trend within the relatively short period (< 50 years).

4.5 Conclusions

As Tanzania becomes increasingly vulnerable to climate change, a scientific understanding of precipitation patterns across the country is critical to predict the evolution of its climate with ensuing global warming, and develop effective mitigation strategies against water-related natural hazards. In this study, we conducted a review while further examining the annual and seasonal climatology of Tanzania to understand past, present, and future precipitation trends and compared

them with findings from other studies. The main conclusions derived from the literature review and the new analyses in this chapter are as follows:

1. Precipitation patterns in Tanzania are highly variable in both space and time, largely due to topographical variations, coastal influences, and presence of lakes.
2. The average annual rainfall distribution is unimodal in southern and western to central Tanzania with one rainy season from November to May, and bimodal in northern and eastern Tanzania with two rainy seasons: the MAM long rains and the SON short rains.
3. A general decreasing precipitation trend is observed in Tanzania since 1960, with the greatest decline in the MAM long rains season.
4. A weak increasing precipitation trend for the SON short rains is observed in northwestern Tanzania around Lake Victoria, contradictory to the decreasing lake level.
5. The IOD exerts a greater influence on Tanzania's precipitation than other modes of climate variability including ENSO.
6. Future projections show an increase in Tanzania's rainfall in response to global warming; this trend contradicts the historical drying trend over East Africa.
7. Observational data and climate model data show opposite precipitation trends for Tanzania, reflecting the challenges faced by climate models in the representation of natural variability.

For reliable projections of future climate in Tanzania, historical climate change and forced variability must be consistently simulated by climate models used by the IPCC. Future work should include other means of precipitation measurement derived from long satellite sources, different trend analyses methods, and varying time intervals (e.g., monthly, annual, decadal) to account for possible uncertainties.

4.6 Supplementary Material

Tanzania has 7 stations (Figure S1) distributed across 885,800 km^2 of its land area [105] with less than 365 observations/year recorded by each station (Figure S2). The number of observations for precipitation since the 1980s has declined dramatically (Figure S2). Stations and land-based measurements in Tanzania are disproportionately located in the northeast (Figure S1), placing more confidence in results for this region than other areas of the country. The more inhomogeneous the network, the harder it is to detect extreme climate events across the field of interest [106 –108]. Interpolation would be least reliable in southern and western Tanzania where stations and observations are minimum (Figure S1), contrary to the uniform model grids. However, comparison of various precipitation datasets and their ensemble mean produce a statistically significant decreasing MAM precipitation trend for Tanzania that is consistent with the observed decrease in East African long rains in recent years (Figure S3). This decline is stronger for CMAP and GPCP precipitation data that include various satellite estimates and gauge data (Figure S3).

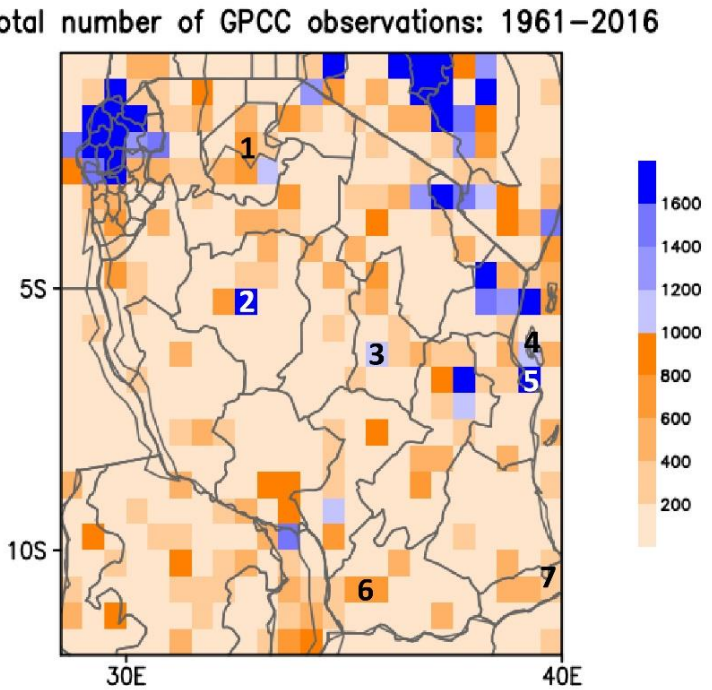

Figure S1. Map of Tanzania showing the number of stations and observations from 1961 to 2016.

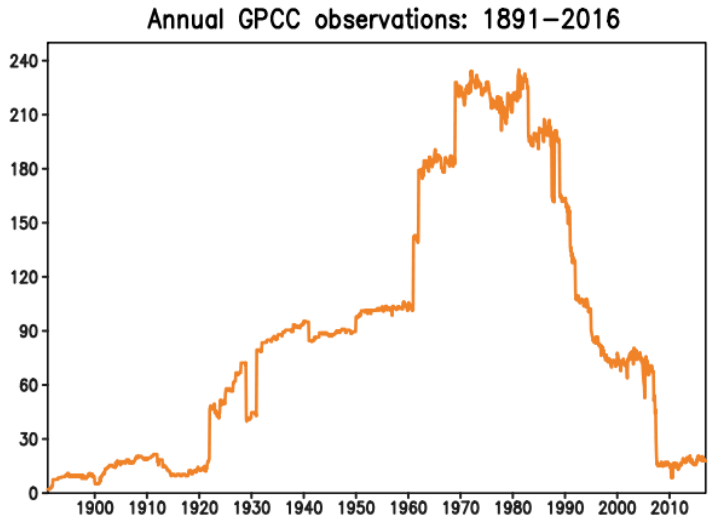

Figure S2. Graph showing the number of observations per year in Tanzania since 1891. A sharp decline in observations occurs after 1980.

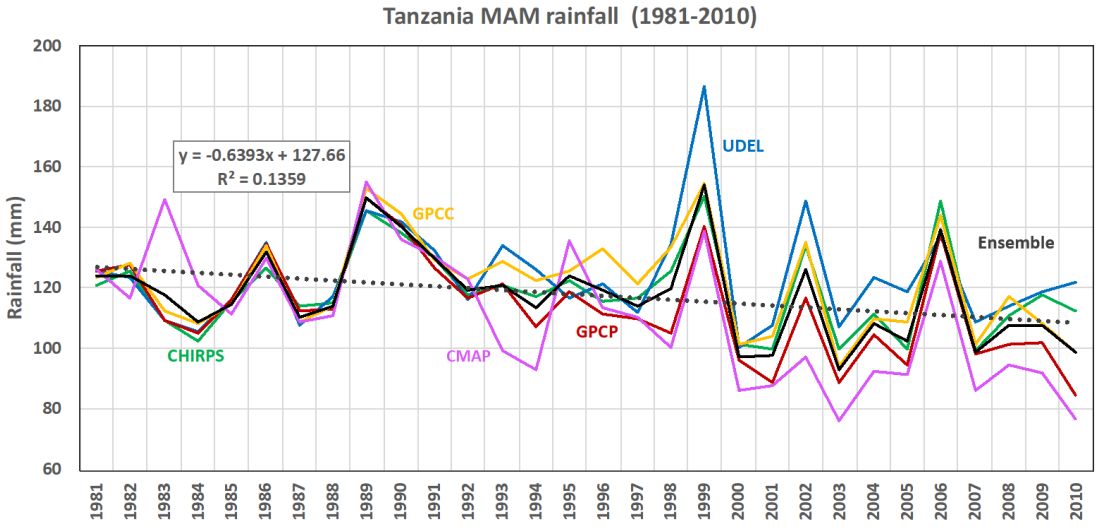

Figure S3. MAM precipitation series from different datasets and their ensemble mean averaged over Tanzania (2–12S, 30–40E). Trend formula was derived from the ensemble mean. Tanzania experiences maximum rainfall during the 'long rains' season in MAM. All datasets show a decreasing precipitation trend in recent decades. GPCP and CMAP data are obtained from satellite estimates and gauge data, and show a stronger declining trend.

REFERENCES

1. Liebmann, B.; Hoerling, M.P.; Funk, C.; Bladé, I.; Dole, R.M.; Allured, D.; Quan, X.; Pegion, P.; Eischeid, J.K. Understanding recent eastern Horn of Africa rainfall variability and change. *J. Clim.* **2014**, *27*, 8630–8645, doi:10.1175/JCLI-D-13-00714.1.

2. Lyon, B. Seasonal drought in the Greater Horn of Africa and its recent increase during the March-May long rains. *J. Clim.* **2014**, *27*, 7953–7975, doi:10.1175/JCLI-D-13-00459.1.

3. Hoell, A.; Hoerling, M.; Eischeid, J.K.; Quan, X.; Liebmann, B. Reconciling theories for human and natural attribution of recent East Africa drying. *J. Clim.* **2017**, *30*, 1939–1957, doi:10.1175/JCLI-D-16-0558.1.

4. Thompson, L.G. Climate change: The evidence and our options. *Behav. Anal.* **2010**, *33*, 153–170, doi:10.1007/BF03392211.

5. Awange, J.L.; Ogalo, L.; Bae, K.H.; Were, P.; Omondi, P.; Omute, P.; Omullo, M. Falling Lake Victoria water levels: Is climate a contributing factor? *Clim. Chang.* **2008**, *89*, 281–297, doi:10.1007/s10584-008-9409-x.

6. Dube, K.; Nhamo, G. Climate variability, change and potential impacts on tourism: Evidence from the Zambian side of the Victoria Falls. *Environ. Sci. Policy* **2018**, *84*, 113–123, doi:10.1016/j.envsci.2018.03.009.

7. Rowell, D.P.; Booth, B.B.; Nicholson, S.E.; Good, P. Reconciling Past and Future Rainfall Trends over East Africa. *J. Clim.* **2015**, *28*, 9768–9788, doi:10.1175/JCLI-D-15-0140.1.

8. Williams, A.P.; Funk, C. A westward extension of the warm pool leads to a westward extension of the Walker circulation, drying eastern Africa. *Clim. Dyn.* **2011**, *37*, 2417–2435, doi:10.1007/s00382-010-0984-y.

9. Shongwe, M.E.; van Oldenborgh, G.J.; van den Hurk, B. Projected changes in mean and extreme precipitation in Africa under global warming. Part II: East Africa. *J. Clim.* **2011**, *24*, 3718–3733, doi:10.1175/2010JCLI2883.1.

10. Mafuru, K.B.; Guirong, T. Assessing Prone Areas to Heavy Rainfall and the Impaction of the Upper Warm Temperature Anomaly during March–May Rainfall Season in Tanzania. *Adv. Meteor.* **2018**, *2018*, 17, doi:10.1155/2018/8353296.

11. Camberlin, P.; Boyard-Micheau, J.; Philippon, N.; Baron, C.; Leclerc, C.; Mwongera, C. Climatic gradients along the windward slopes of Mount Kenya and their implication for crop risks. Part 1: Climate variability. *Int. J. Climatol.* **2014**, *34*, 2136–2152, doi:10.1002/joc.3427.

12. Indeje, M.; Semazzi, F.H.; Ogallo, L.J. ENSO signals in East African rainfall seasons. *Int. J. Climatol.* **2000**, *20*, 19–46, doi:10.1002/(SICI)1097-0088(200001)20:1<19::AID-JOC449>3.0.CO;2-0.

13. Schreck, C.J., III.; Semazzi, F.H.M. Variability of the recent climate of eastern Africa. *Int. J. Climatol.* **2004**, *24*, 681–701, doi:10.1002/joc.1019.

14. Kijazi, A.; Reason, C. Relationships between intraseasonal rainfall variability of coastal Tanzania and ENSO. *Theor. Appl. Climatol.* **2005**, *82*, 153–176, doi:10.1007/s00704-005-0129-0.

15. Lyon, B.; Vigaud, N. Unraveling East Africa's Climate Paradox. In *Climate Extremes: Patterns and Mechanisms*, 1st ed.; Wang, S.Y., Yoon, J.H., Funk, C., Gillies, R., Eds.; John Wiley & Sons Inc.: New York, NY, USA, 2017; Volume 16, pp. 265–281, doi:10.1002/9781119068020.ch16.

16. Endris, H.S.; Lennard, C.; Hewitson, B.; Dosio, A.; Nikulin, G.; Artan, G.A. Future changes in rainfall associated with ENSO, IOD and changes in the mean state over Eastern Africa. *Clim. Dyn.* **2019**, *52*, 2029–2053, doi:10.1007/s00382-018-4239-7.

17. Schneider, U.; Becker, A.; Finger, P.; Meyer-Christoffer, A.; Rudolf, B.; Ziese, M. GPCC Full Data Reanalysis Version 6.0 at 0.5°: Monthly Land-Surface Precipitation from Rain-Gauges built on GTS-based and Historic Data. *GPCC Data Rep*. **2011**, *10*, doi:10.5676/DWD_GPCC/FD_M_V6_050.

18. Meyer-Christoffer, A.; Becker, A.; Finger, P.; Schneider, U.; Ziese, M. GPCC Climatology Version 2018 at 0.25°: Monthly Land-Surface Precipitation Climatology for Every Month and the Total Year from Rain-Gauges built on GTS-based and Historical Data. *GPCC Ger.* **2018**, doi:10.5676/DWD_GPCC/CLIM_M_V2018_025.

19. Rudolf, B.; Becker, A.; Schneider, U.; Meyer-Christoffer, A.; Ziese, M. New GPCC Full Data Reanalysis Version 5 Provides High-Quality Gridded Monthly Precipitation Data. *GPCC Status Rep.* **2011**, *21*, 1–7.

20. Amante, C.; Eakins, B.W. ETOPO1 1 Arc-Minute Global Relief Model: Procedures, Data Sources and Analysis. *NOAA Technical Memorandum NESDIS NGDC-24*; National Geophysical Data Center-NOAA: 2009, Boulder, Colorado, USA.

21. National Center for Atmospheric Research Staff (Ed). Last modified 22 July 2013. The Climate Data Guide: Empirical Orthogonal Function (EOF) Analysis and Rotated EOF Analysis. Available online: https://climatedataguide.ucar.edu/climate-data-tools-and-analysis/empirical-orthogonal-function-eof-analysis-and-rotated-eof-analysis (accessed on 15 December 2019).

22. Zhang, Z.; Moore, J.C. *Mathematical and Physical Fundamentals of Climate Change*, 1st ed.; Elsevier: Amsterdam, The Netherlands, 2015; pp. 161–197, doi:10.1016/B978-0-12-800066-3.00006-1.

23. Attuabea, D.; Oduro, F.; Ansah, R. Empirical orthogonal function (EOF) analysis of precipitation over Ghana. *Int. J. Stat. Adv. Theor. Appl.* **2017**, *1*, 121–141.

24. Philippon, N.; Doblas-Reyes, F.J.; Ruti, P.M. Skill, reproducibility and potential predictability of the West African monsoon in coupled GCMs. *Clim. Dyn.* **2010**, *35*, 53–74, doi:10.1007/s00382-010-0856-5.

25. Huang, B.; Thorne, P.W.; Banzon, V.F.; Boyer, T.; Chepurin, G.; Lawrimore, J.H.; Menne, M.J.; Smith, T.M.; Vose, R.S.; Zhang, H.M. NOAA Extended Reconstructed Sea Surface

Temperature (ERSST), Version 5. NOAA National Centers for Environmental Information 2017. *Inf. NNCfE* **2017**.

26. Kalnay, E.; Kanamitsu, M.; Kistler, R.; Collins, W.; Deaven, D.; Gandin, L.; Iredell, M.; Saha, S.; White, G.; Woollen, J.; et al. The NCEP/NCAR 40-Year Reanalysis Project. *Bull. Amer. Meteor. Soc.* **1996**, *77*, 437–472, doi:10.1175/1520-0477(1996)077<0437:TNYRP>2.0.CO;2.

27. Bengtsson, L.; Hodges, K.I. Can an ensemble climate simulation be used to separate climate change signals from internal unforced variability? *Clim. Dyn.* **2019**, *52*, 3553–3573, doi:10.1007/s00382-018-4343-8.

28. Eyring, V.; Bony, S.; Meehl, G.A.; Senior, C.A.; Stevens, B.; Stouffer, R.J.; Taylor, K.E. Overview of the Coupled Model Intercomparison Project Phase 6 (CMIP6) experimental design and organization. *Geosci. Model Dev.* **2016**, *9*, 1937–1958, doi:10.5194/gmd-9-1937-2016.

29. Meehl, G.; Boer, G.; Covey, C.; Latif, M.; Stouffer, R. The Coupled Model Intercomparison Project (CMIP). *Bull. Amer. Meteorol. Soc.* **2000**, *81*, 313–318.

30. Taylor, K.E.; Stouffer, R.J.; Meehl, G.A. An overview of CMIP5 and the experiment design. *Bull. Am. Meteor. Soc.* **2012**, *93*, 485–498, doi:10.1175/BAMS-D-11 00094.1.

31. Sillmann, J.; Kharin, V.V.; Zwiers, F.W.; Zhang, X.; Bronaugh, D. Climate extremes indices in the CMIP5 multi-model ensemble. Part 1: Model evaluation in the present climate. *J. Geophys. Res. Atmos.* **2013**, *118*, 1716–1733, doi:10.1002/jgrd.50203.

32. Sillmann, J.; Kharin, V.V.; Zwiers, F.W.; Zhang, X.; Bronaugh, D. Climate extremes indices in the CMIP5 multi-model ensemble. Part 2: Future climate projections. *J. Geophys. Res. Atmos.* **2013**, *118*, 2473–2493, doi:10.1002/jgrd.50188.

33. Moss, R.; Edmonds, J.; Hibbard, K.; Manning, M.; Rose, S.; Vuuren, D.; Carter, T.; Emori, S.; Kainuma, M.; Kram, T.; et al. The next generation of scenarios for climate change research and assessment. *Nature* **2010**. *463*, 747–756, doi:10.1038/nature08823.

34. Freychet, N.; Hsu, H.H.; Chou, C.; Wu, C.H. Asian summer monsoon in CMIP5 projections: A link between the change in extreme precipitation and monsoon dynamics. *J. Clim.* **2015**, *28*, 1477–1493, doi:10.1175/JCLI-D-14-00449.1.

35. Duane, W.J.; Pepin, N.C.; Losleben, M.L.; Hardy, D.R. General Characteristics of Temperature and Humidity Variability on Kilimanjaro, Tanzania. *Arct. Antarct. Alp. Res.* **2008**, *40*, 323–334, doi:10.1657/1523-0430(06-127)[DUANE]2.0.CO;2.

36. Nicholson, S.E. A review of climate dynamics and climate variability in eastern Africa. In *The Limnology, Climatology, and Paleoclimatology of the East African Lakes*; Johnson, T.C., Odada, E.O., Eds.; Gordon and Breach Publishers: Amsterdam, The Netherlands, 1996; pp. 25–56.

37. Bryson, R.; Kuhn, P. Stress—Differential Induced Divergence with Application to Littoral Precipitation. *Erdkunde* **1961**, *15*, 287–294.

38. Nicholson, S.E. Climate and climatic variability of rainfall over eastern Africa. *Rev. Geophys.* **2017**, *55*, 590–635, doi:10.1002/2016RG000544.

39. Flohn, H.; Fraedrich, K. Tagesperiodische zirkulation und niederschlagsverteilungam Victoria-See (Ostafrika) (the daily periodic circulation and distribution of rainfall over Lake Victoria, in German). *Meteorologische Rundschau* **1966**, *19*, 157–165.

40. Yin, X.; Nicholson, S.E.; Ba, M.B. On the diurnal cycle of cloudiness over Lake Victoria and its influence on evaporation from the lake. *Hydrolog. Sci. J.* **2000**, *45*, 407–424, doi:10.1080/02626660009492338.

41. Ba, M.B.; Nicholson, S.E. Analysis of Convective Activity and Its Relationship to the Rainfall over the Rift Valley Lakes of East Africa during 1983–90 Using the Meteosat Infrared Channel. *J. Appl. Meteor.* **1998**, *37*, 1250–1264, doi:10.1175/1520-0450(1998)037<1250:AOCAAI>2.0.CO;2.

42. Song, Y.; Semazzi, F.H.M.; Xie, L.; Ogallo, L.J. A coupled regional climate model for the Lake Victoria basin of East Africa. *Int. J. Climatol.* **2004**, *24*, 57–75, doi:10.1002/joc.983.

43. Flohn, H.; Burkhardt, T. Nile Runoff at Aswan and Lake Victoria: A Case of a Discontinuous Climate Time Series. *Z. Gletscherk. Glazialgeol.* **1985**, *21*, 125–130.

44. Thiery, W.; Davin, E.; Seneviratne, S.; Bedka, K.; Lhermitte, S.; van Lipzig, N.P.M. Hazardous thunderstorm intensification over Lake Victoria. *Nat. Commun.* **2016**, *7*, 12786, doi:10.1038/ncomms12786.

45. Khavse, R.; Deshmukh, R.; Manikandan, N.; Chaudhary, J.L.; Kaushik, D. Statistical Analysis of Temperature and Rain fall Trend in Raipur District of Chhattisgarh. *Curr. World Environ.* **2015**, *10*, 305–312, doi:10.12944/CWE.10.1.38.

46. Kull, D. Connections between Recent Water Level Drops in Lake Victoria, Dam Operations and Drought. 2006. Available online: http://www.irn.org/programs/nile/pdf/060208vic.pdf (accessed on 20 December 2019).

47. Verdin, J.; Funk, C.; Senay, G.; Choularton, R. Climate science and famine early warning. *Philos. Trans. R. Soc. Lond. B. Biol. Sci.* **2005**, *360*, 2155–2168, doi:10.1098/rstb.2005.1754.

48. Funk, C.C.; Dettinger, M.D.; Michaelsen, J.C.; Verdin, J.P.; Brown, M.E.; Barlow, M.; Hoell, A. Warming of the Indian Ocean threatens eastern and southern African food security but could be mitigated by agricultural development. *Proc. Natl. Acad. Sci. USA* **2008**, *105*, 11081–11086, doi:10.1073/pnas.0708196105.

49. Lyon, B.; Dewitt, D.G. A recent and abrupt decline in the East African long rains. *Geophys. Res. Lett.* **2012**, *39*, L02702, doi:10.1029/2011GL050337.

50. Yang, W.; Seager, R.; Cane, M.A.; Lyon, B. The East African long rains in observations and models. *J. Clim.* **2014**, *27*, 7185–7202, doi:10.1175/JCLI-D-13-00447.1.

51. Tierney, J.E.; Ummenhofer, C.C.; DeMenocal, P.B. Past and future rainfall in the horn of Africa. *Sci. Adv.* **2015**, *1*, e1500682, doi:10.1126/sciadv.1500682.

52. Vellinga, M.; Milton, S.F. Drivers of interannual variability of the East African “Long Rains”. *Q. J. R. Meteorol. Soc.* **2018**, *144*, 861–876, doi:10.1002/qj.3263.

53. Mazzarella, A.; Giuliacci, A.; Liritzis, I. On the 60-month cycle of multivariate ENSO index. *Theor. Appl. Climatol.* **2010**, *100*, 23–27, doi:10.1007/s00704-009-0159-0.

54. Wainwright, C.M.; Marsham, J.H.; Keane, R.J.; Rowell, D.P.; Finney, D.L.; Black, E.; Allan, R.P. ‘Eastern African Paradox’ rainfall decline due to shorter not less intense Long Rains. *npj Clim. Atmos. Sci.* **2019**, *2*, 9, doi:10.1038/s41612-019-0091-7.

55. Liebmann, B.; Bladé, I.; Funk, C.; Allured, D.; Quan, X.; Hoerling, M.; Hoell, A.; Peterson, P.; Thiaw, W.M. Climatology and Interannual Variability of Boreal Spring Wet Season Precipitation in the Eastern Horn of Africa and Implications for Its Recent Decline. *J. Clim.* **2017**, *30*, 3867–3886, doi:10.1175/JCLI-D-16-0452.1.

56. Funk, C.; Hoell, A.; Shukla, S.; Bladé, I.; Liebmann, B.; Roberts, J.B.; Robertson, F.R.; Husak, G. Predicting East African spring droughts using Pacific and Indian Ocean sea surface temperature indices. *Hydrol. Earth Syst. Sci.* **2014**, *18*, 4965–4978, doi:10.5194/hess-18-4965-2014.

57. Ogallo, L.J.; Okoola, R.E.; Wanjohi, D.N. Characteristics of Quasi-Biennial Oscillation over Kenya and their predictability potential for seasonal rainfall. MAUSAM. *Q. J. Meteorol. Hydrol. Geophys.* **1994**, *45*, 57–62.

58. Pohl, B.; Camberlin, P. Influence of the Madden–Julian Oscillation on East African rainfall. I: Intraseasonal variability and regional dependency. *Q. J. R. Meteorol. Soc.* **2006**, *132*, 2521–2539, doi:10.1256/qj.05.104.

59. Saji, N.H.; Goswami, B.N.; Vinayachandran, P.N.; Yamagata, T. A dipole mode in the tropical Indian Ocean. *Nature* **1999**, *401*, 360–363, doi:10.1038/43854.

60. Webster, P.J.; Moore, A.M.; Loschnigg, J.P.; Leben, R.R. Coupled ocean-atmosphere dynamics in the Indian Ocean during 1997–98. *Nature* **1999**, *401*, 356–360, doi:10.1038/43848.

61. Camberlin, P.; Wairoto, J. Intraseasonal wind anomalies related to wet and dry spells during the“long”and“short”rainy seasons in Kenya. *Theor. Appl. Climatol.* **1997**, *58*, 57–69, doi:10.1007/BF00867432.

62. Hastenrath, S.; Polzin, D.; Mutai, C. Circulation Mechanisms of Kenya Rainfall Anomalies. *J. Clim.* **2011**, *24*, 404–412, doi:10.1175/2010JCLI3599.1.

63. Moron, V.; Robertson, A.W.; Ward, M.N.; Camberlin, P. Spatial coherence of tropical rainfall at the regional scale. *J. Clim.* **2007**, *20*, 5244–5263, doi:10.1175/2007JCLI1623.1.

64. Camberlin, P.; Moron, V.; Okoola, R.E.; Philippon, N.; Gitau, W. Components of rainy seasons’ variability in equatorial East Africa: Onset, cessation, rainfall frequency and intensity. *Theor. Appl. Climatol.* **2009**, *98*, 237–249, doi:10.1007/s00704-009-0113-1.

65. Camberlin, P.; Philippon, N. The East African March–May Rainy Season: Associated Atmospheric Dynamics and Predictability over the 1968–97 Period. *J. Clim.* **2002**, *15*, 1002–1019, doi:10.1175/1520-0442(2002)015<1002:TEAMMR>2.0.CO;2.

66. Ogallo, L.J. Relationships between seasonal rainfall in East Africa and the Southern Oscillation. *J. Climatol.* **1988**, *8*, 31–43, doi:10.1002/joc.3370080104.

67. Reason, C.J.C.; Allan, R.J.; Lindesay, J.A.; Ansell, T.J. ENSO and climatic signals across the Indian Ocean basin in the global context: Part I. Interannual composite patterns. *Int. J. Climatol.* **2000**, *20*, 1285–1327, doi:10.1002/1097-0088(200009)20:11<1285::AID-JOC536>3.0.CO;2-R.

68. Nicholson, S.E.; Kim, J. The relationship of the El Niño–Southern Oscillation to African rainfall. *Int. J. Climatol.* **1997**, *17*, 117–135, doi:10.1002/(SICI)1097-0088(199702)17:2<117::AID-JOC84>3.0.CO;2-O.

69. Mahongo, S.B.; Francis, J. Analysis of rainfall variations and trends in Coastal Tanzania. Western Indian Ocean. *J. Mar. Sci.* **2002**, *11*, 121–133.

70. Hastenrath, S.; Nicklis, A.; Greischar, L. Atmospheric-hydrospheric mechanisms of climate anomalies in the western equatorial Indian Ocean. *J. Geophys. Res.* **1993**, *98*, 20219–20235, doi:10.1029/93JC02330.

71. Diro, G.T.; Grimes, D.I.F.; Black, E. Teleconnections between Ethiopian summer rainfall and sea surface temperature: Part I—Observation and modelling. *Clim. Dyn.* **2011**, *37*, 103–119, doi:10.1007/s00382-010-0837-8.

72. Goddard, L.; Graham, N.E. Importance of the Indian Ocean for simulating rainfall anomalies over eastern and southern Africa. *J. Geophys. Res. Atmos.* **1999**, *104*, 19099–19116, doi:10.1029/1999JD900326.

73. Latif, M.; Dommenget, D.; Dima, M.; Grötzner, A. The role of Indian Ocean sea surface temperature in forcing East African rainfall anomalies during December–January 1997/98. *J. Clim.* **1999**, *12*, 3497–3504, doi:10.1175/1520-0442(1999)012<3497:TROIOS>2.0.CO;2.

74. Bahaga, T.K.; Tsidu, M.; Kucharski, G.F.; Diro, G.T. Potential predictability of the sea-surface temperature forced equatorial East African short rains interannual variability in the 20th century. *Q. J. R. Meteorol. Soc.* **2015**, *141*, 16–26, doi:10.1002/qj.2338.

75. Endris, H.S.; Lennard, C.; Hewitson, B.; Dosio, A.; Nikulin, G.; Nikulin, G.; Panitz, H.J. Teleconnection responses in multi-GCM driven CORDEX RCMs over Eastern Africa. *Clim. Dyn.* **2016**, *46*, 2821–2846, doi:10.1007/s00382-015-2734-7.

76. Black, E.; Slingo, J.; Sperber, K.R. An Observational Study of the Relationship between Excessively Strong Short Rains in Coastal East Africa and Indian Ocean SST. *Mon. Weather Rev.* **2003**, *131*, 74–94, doi:10.1175/1520-0493(2003)131<0074:AOSOTR>2.0.CO;2.

77. Behera, S.K.; Luo, J.J.; Masson, S.; Delecluse, P.; Gualdi, S.; Navarra, A.; Yamagata, T. Paramount impact of the Indian Ocean dipole on the East African short rains: A CGCM study. *J. Clim.* **2005**, *18*, 4514–4530, doi:10.1175/JCLI3541.1.

78. Ummenhofer, C.C.; Gupta, A.S.; England, M.H.; Reason, C.J. Contributions of Indian Ocean Sea Surface Temperatures to Enhanced East African Rainfall. *J. Clim.* **2009**, *22*, 993–1013, doi:10.1175/2008JCLI2493.1.

79. Loaiciga, H.A.; Valdes, J.B.; Vogel, R.; Garvey, J.; Schwarz, H. Global warming and the hydrologic cycle. *J. Hydrol.* **1996**, *174*, 83–127, doi:10.1016/0022-1694(95)02753-X.

80. Arnell, N.W.; Liu, C.; Compagnucci, R.; da Cunha, L.; Hanaki, K.; Howe, C.; Mailu, G.; Shiklomanov, I.; Stakhiv, E. Hydrology and water resources. In *Climate Change 2001: Impacts, Adaptation and Vulnerability*, 1st ed.; McCarthy, J.J., Canziani, O.F., Leary, N.A., Dokken, D.J., White, K.S., Eds.; Cambridge University Press: Cambridge, UK, 2001; pp. 191–233.

81. Huntington, T.G. Evidence for intensification of the global water cycle: Review and synthesis. *J. Hydrol.* **2006**, *319*, 83–95, doi:10.1016/j.jhydrol.2005.07.003.

82. Souverijns, N.; Thiery, W.; Demuzere, M.; van Lipzig, N.P.M. Drivers of future changes in East African precipitation. *Environ. Res. Lett.* **2016**, *11*, 114011, doi:10.1088/1748-9326/11/11/114011.

83. Estrada, F.; Tol, R.S.; Botzen, W.J. Global economic impacts of climate variability and change during the 20th century. *PLoS ONE* **2017**, *12*, e0172201, doi:10.1371/journal.pone.0172201.

84. Terray, L.; Cassou, C. Modes of low-frequency climate variability and their relationships with land precipitation and surface temperature: Application to the Northern Hemisphere winter climate. *Stoch. Environ. Res. Risk A* **2000**, *14*, 339–369, doi:10.1007/s004770000054.

85. Meehl, G.A.; Arblaster, J.M.; Fasullo, J.T.; Hu, A.; Trenberth, K.E. Model-based evidence of deep-ocean heat uptake during surface-temperature hiatus periods. *Nat. Clim. Chang.* **2011**, *1*, 360–364, doi:10.1038/nclimate1229.

86. Meehl, G.A.; Hu, A.; Arblaster, J.M.; Fasullo, J.T.; Trenberth, K.E. Externally forced and internally generated decadal climate variability associated with the Interdecadal Pacific Oscillation. *J. Clim.* **2013**, *26*, 7298–7310, doi:10.1175/JCLI-D-12-00548.1.

87. Trenberth, K.E.; Fasullo, J.T. An apparent hiatus in global warming? *Earth's Future* **2013**, *1*, 19–32, doi:10.1002/2013EF000165.

88. Tollefson, J. The case of the missing heat. *Nature* **2014**, *505*, 276–278.

89. Schmidt, G.A.; Shindell, D.; Tsigaridis, K. Reconciling warming trends. *Nat. Geosci.* **2014**, *7*, 158–160, doi:10.1038/ngeo2105.

90. Watanabe, M.; Shiogama, H.; Tatebe, H.; Hayashi, M.; Ishii, M.; Kimoto, M. Contribution of natural decadal variability to global warming acceleration and hiatus. *Nat. Clim. Chang.* **2014**, *4*, 893–897, doi:10.1038/nclimate2355.

91. Flato, G.; Marotzke, J.; Abiodun, B.; Braconnot, P.; Chou, S.C.; Collins, W.; Cox, P.; Driouech, F.; Emori, S.; Eyring, V.; et al. Evaluation of Climate Models. In *Climate Change 2013: The Physical Science Basis. Contribution of Working Group I to the Fifth Assessment Report of the Intergovernmental Panel on Climate Change*, 1st ed.; Stocker, T.F., Qin, D.,

Plattner, G.K., Tignor, M., Allen, S.K., Boschung, J., Nauels, A., Xia, Y., Bex, V., Midgley, P.M., Eds.; Cambridge University Press: Cambridge, UK; New York, NY, USA, 2013; pp. 741–866.

92. Hawkins, E.; Sutton, R. The potential to narrow uncertainty in projections of regional precipitation change. *Clim. Dyn.* **2011**, *37*, 407–418, doi:10.1007/s00382-010-0810-6.

93. Johnson, J.S.; Cui, Z.; Lee, L.A.; Gosling, J.P.; Blyth, A.M.; Carslaw, K.S. Evaluating uncertainty in convective cloud microphysics using statistical emulation. *J. Adv. Model. Earth Syst.* **2015**, *7*, 162–187, doi:10.1002/2014MS000383.

94. Payne, M.R.; Barange, M.; Cheung, W.W.L.; MacKenzie, B.R.; Batchelder, H.P.; Cormon, X.; Eddy, T.D.; Fernandes, J.A.; Hollowed, A.B.; Jones, M.C.; et al. Uncertainties in projecting climate-change impacts in marine ecosystems. *ICES J. Mar. Sci.* **2016**, *73*, 1272–1282, doi:10.1093/icesjms/fsv231.

95. Hayhoe, K.; Edmonds, J.; Kopp, R.E.; LeGrande, A.N.; Sanderson, B.M.; Wehner, M.F.; Wuebbles, D.J. Climate models, scenarios, and projections. In *Climate Science Special Report: Fourth National Climate Assessment*, 1st ed.; Wuebbles, D.J., Fahey, D.W., Hibbard, K.A., Dokken, D.J., Stewart, B.C., Maycock, T.K., Eds.; U.S. Global Change Research Program: Washington, DC, USA, 2017; Volume I, pp. 133–160, doi:10.7930/J0WH2N54.

96. Kharin, V.V.; Zwiers, F.W.; Zhang, X.B.; Hegerl, G.C. Changes in temperature and precipitation extremes in the IPCC ensemble of global coupled model simulations. *J. Clim.* **2007**, *20*, 1419–1444, doi:10.1175/JCLI4066.1.

97. Kharin, V.V.; Zwiers, F.W.; Zhang, X.B.; Wehner, M. Changes in temperature and precipitation extremes in the CMIP5 ensemble. *Clim. Chang.* **2013**, *119*, 345–357, doi:10.1007/s10584-013-0705-8.

98. Chen, C.T.; Knutson, T. On the verification and comparison of extreme rainfall indices from climate models. *J. Clim.* **2008**, *21*, 1605–1621, doi:10.1175/2007JCLI1494.1.

99. Chou, C.; Neelin, J.D. Mechanisms of Global Warming Impacts on Regional Tropical Precipitation. *J. Clim.* **2004**, *17*, 2688–2701, doi:10.1175/15200442(2004)017<2688:MOGWIO>2.0.CO;2.

100. Giannini, A.; Biasutti, M.; Held, I.M.; Sobel, A.H. A global perspective on African climate. *Clim. Chang.* **2008**, *90*, 359–383, doi:10.1007/s10584-008-9396-y.

101. Allan, R.P.; Soden, B.J.; John, V.O.; Ingram, W.; Good, P. Current chances in tropical precipitation. *Environ. Res. Lett.* **2010**, *5*, 25205, doi:10.1088/1748-9326/5/2/025205.

102. Xie, S.; Deser, C.; Vecchi, G.A.; Ma, J.; Teng, H.; Wittenberg, A.T. Global Warming Pattern Formation: Sea Surface Temperature and Rainfall. *J. Clim.* **2010**, *23*, 966–986, doi:10.1175/2009JCLI3329.1.

103. Mizuta, R.; Yoshimura, H.; Murakami, H.; Matsueda, M.; Endo, H.; Ose, T.; Kamiguchi, K.; Hosaka, M.; Sugi, M.; Yukimoto, S.; et al. Climate simulations using MRI-AGCM3.2 with 20-km grid. *J. Meteorol. Soc. Jpn.* **2012**, *90A*, 233–258, doi:10.2151/jmsj.2012-A12.

104. James, R.; Washington, R. Changes in African temperature and precipitation associated with degrees of global warming. *Clim. Chang.* **2013**, *117*, 859–872, doi:10.1007/s10584-012-0581-7.

105. Tanzania National Bureau of Statistics, Tanzania in figures. 2018. Available online: https://www.nbs.go.tz/nbs/takwimu/references/Tanzania_in_Figures_2018.pdf (accessed on 20 January 2020).

106. Lovejoy, S.; Schertzer, D.; Ladoy, P. Fractal characterization of inhomogeneous geophysical measuring networks. *Nature* **1986**, *319*, 43–44. , doi:10.1038/319043a0

107. Guentchev, G.; Barsugli, J.J.; Eischeid, J. Homogeneity of Gridded Precipitation Datasets for the Colorado River Basin. *J. Appl. Meteor. Climatol.* **2010**, *49*, 2404–2415. , doi:10.1175/2010JAMC2484.1

108. Hofstra, N.; New, M.; McSweeney, C. The influence of interpolation and station network density on the distributions and trends of climate variables in gridded daily data. *Clim. Dyn.* **2010**, *35*, 841–858. , doi:10.1007/s00382-009-0698-1

CHAPTER 5

CONCLUSION

5.1 Summary

The dissertation explored (i) the dynamics underlying the 1-year lead WNP–ENSO relationship and its role in shaping ENSO in a warming world, (ii) the dynamics of the 3-year relationship and its contribution towards advancing ENSO prediction efforts at extended lead times, and (iii) Tanzania's precipitation climatology that falls within the range of ENSO teleconnection.

The second chapter examined the role of boreal winter air–sea interactions in the western North Pacific in promoting El Nino development the following winter. We applied a conditional probability approach using historical and SSP370 runs of CMIP6 and CESM2-LE to focus on the effects of future warming. ENSO diversity modulated by this relationship depends on the relative strength of zonal advective feedback and thermocline feedback, and the background state at the time of the event. The amplitude and frequency of El Niños is expected to increase under WNP influence with climate warming. The intensification of positive Pacific Meridional Mode (PMM) southwesterlies during the WNP–ENSO transition suggests a strengthened three-way link between WNP, PMM and ENSO under enhanced warming that may promote stronger and/or more frequent El Niños.

The third chapter investigated how a series of warm and cold SSTAs propagating from the western North Pacific to the central–eastern equatorial Pacific in 3 years may promote development of El Niños and La Niñas, respectively. During a warm (cold) WNP phase in the boreal winter, strengthening (weakening) of trade winds intensifies (weakens) the anticyclonic flow across the subtropical North Pacific. After formation, the SSTA propagates along the southeastern quadrant of the North Pacific Subtropical Gyre that slopes from the western North Pacific to the central–eastern equatorial Pacific. The slow, broad, shallow, and southward flow of the EBC facilitates

slow and steady propagation of the SSTA over long distances toward the tropics under the influence of surface winds and rotational effects. For the positive SSTA, most of the warm water of the SSTA is advected towards the Western Pacific Warm Pool by southwest deflection. Strengthened downwelling during the warm WNP phase intensifies divergence in the subtropical geostrophic layer and advects heat anomalies towards the Western Pacific Warm Pool through the subsurface. Progressive southeast movement of the SSTA downslope continues to increase the warm water volume in the western tropical Pacific and strengthen the E–W equatorial gradients of SST, SSH and MLD. This promotes westerly anomalies that advect the warm water volume from the western to eastern equatorial Pacific in the year leading up to an El Niño. As geostrophic gyres and anomalies associated with rotating stratified fluids are always either at or near geostrophic equilibrium, WNP SSTAs are very persistent and their propagation to the tropics can be used to extend ENSO prediction lead times up to 3 years in advance.

The fourth chapter investigated historical and projected precipitation in Tanzania using observational and climate model data and the extent of ENSO influence in Tanzania's precipitation climatology. Climatologically, maximum rainfall decline in Tanzania occurs during the long rainy season in the fall (March–May), however, an increasing precipitation trend is observed in northwestern Tanzania during the short rainy season in the spring (September–November). While ENSO exerts some influence on Tanzania's climatology, the analyses in this chapter suggest that the Indian Ocean Dipole (IOD) may have a greater effect on rainfall variability in Tanzania than ENSO.

5.2 Future directions

Several studies report adjacent warm and cold SSTA associated with different modes of climate variability in the Pacific, Atlantic and Indian Oceans, most of which form cross equatorial or mid-latitude symmetry (Czaja and Frankignoul 2002; Peng et al. 2003; Pan 2007; Park and Kug 2013; Newman et al. 2016; Chen et al. 2020; Johnson et al. 2020; Zhou et al. 2020; Yao et al. 2021;

Zhang and Du 2021; Sun et al. 2022). The dynamics discussed in this dissertation have broader applications that offer insight into some fundamental dynamics underlying the formation of "horseshoe" SSTA patterns and tripoles and their relationship with ocean gyres.

During a warm WNP phase, two well-defined "horseshoe" SSTA patterns are observed in the tropics and subtropics (Fig. 1). Diagnostic features of such patterns are mid-latitude symmetry at around 30°N and/or cross-equatorial symmetry. The strengthening of trade winds during the warm phase is accompanied by strengthening of westerlies. The relative strength of easterly vs. westerly wind stress anomalies affects the development of mid-latitude symmetry because it affects the intensity of the zonal SSTA gradient at 30°N. In the North Pacific, strengthened trade winds (westerlies) favor intensification of the anticyclonic subtropical gyre (cyclonic subpolar gyre). Strengthened trade winds intensify the positive (negative) curl in the western tropical (eastern subtropical) Pacific. This intensifies divergence along the equator (30°N) in the western (eastern) Pacific and develops the cross-equatorial (mid-latitude) symmetry if synchronous with strengthening of trade winds in the southern hemisphere as well. The magnitude of the trade wind anomalies is the key factor that affects the development of cross-equatorial symmetry because the intensity of divergence in the western equatorial Pacific affects the intensity of the E–W equatorial SSTA gradient. However, stronger westerly anomalies compared to trade wind anomalies induce stronger cyclonic flow and divergence in the subpolar regions compared to lower latitudes. The amplification of the subtropical gyre is restricted by strengthening of westerlies. The subtropical (eastern tropical) convergence zone is intensified but to a lesser degree and expands to the east (west), causing the zonal SSTA contrast at 30°N (0°) to become weaker. This would eventually break off the horseshoe pattern and form a tripole instead. The signs would simply be reversed for a cold WNP phase. Although this dissertation focused on WNP and ENSO dynamics, there exists a prevalence of comparable horseshoe SSTAs across literature associated with several modes of variability in different oceans displaying mid-latitude at 30°N or cross-equatorial symmetry (e.g.,

Czaja and Frankignoul 2002; Peng et al. 2018). While some of these patterns look similar, their differences and impacts are very significant. For instance, PDO patterns are nearly identical to ENSO patterns, with the exception that the maximum SSTAs occur in the tropics (subtropics) for ENSO (PDO) and interannual (decadal) time scales are inherent of ENSO (PDO; Deser et al. 2012). In chapter 3, "horseshoe" SSTA patterns during a WNP phase are connected to ocean gyre dynamics associated with strengthening of the trade winds and westerlies. But this finding raises the question as to whether even small shifts cause by variations between large scale tropical and subtropical winds may produce vastly different modes of climate variability with varying amplitudes and frequencies by changing the location of the maximum SSTA. SSTA patterns resulting from large-scale wind stress curl anomalies can be sustained over long periods after the atmospheric signal dissipates, particularly if the flow dynamics are geostrophic. The dynamics of Sverdrup transport and rotating stratified fluids in geostrophic systems can potentially help explain the formation, development, and persistence of various low frequency modes associated with different oceans.

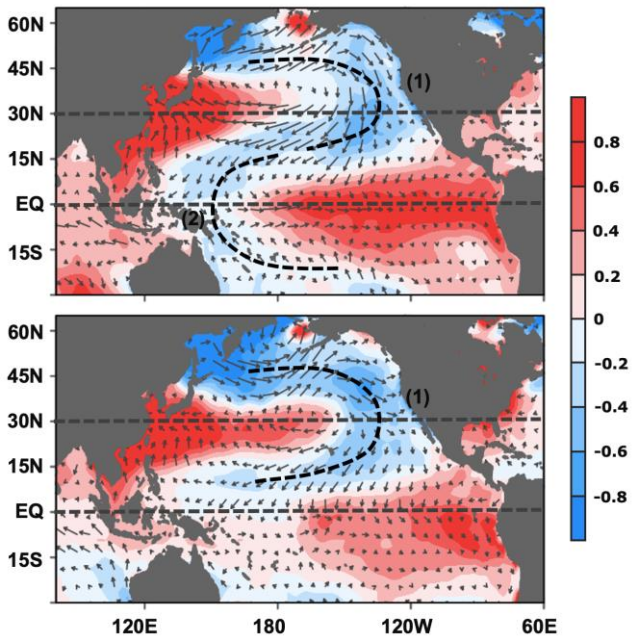

Fig 1. SST correlation with warm WNP SSTA over different time periods (a) 1950–1980 (b) 1990–2020. "Horseshoe" SSTA patterns (dashed black curves) with (1) mid-latitude and (2) cross-equatorial symmetry.

REFERENCES

Chen S, Wu R, Chen W (2020) Strengthened Connection between Springtime North Atlantic Oscillation and North Atlantic Tripole SST Pattern since the Late 1980s. J Clim 33:2007–2022. https://doi.org/10.1175/JCLI-D-19-0628.1

Czaja A, Frankignoul C (2002) Observed Impact of Atlantic SST Anomalies on the North Atlantic Oscillation. J Clim 15:606–623. https://doi.org/10.1175/1520-0442(2002)015<0606:OIOASA>2.0.CO;2

Deser C, Phillips AS, Tomas RA et al (2012) ENSO and Pacific Decadal Variability in the Community Climate System Model Version 4. J Clim 25:2622–2651. https://doi.org/10.1175/JCLI-D-11-00301.1

Johnson NC, Amaya DJ, Ding Q, Kosaka Y, Tokinaga H, Xie S-P (2020) Multidecadal modulations of key metrics of global climate change. Global and Planetary Change 188:103149. https://doi.org/10.1016/j.gloplacha.2020.103149

Newman M, Alexander MA, Ault TR et al (2016) The Pacific Decadal Oscillation, Revisited. J Clim 29:4399–4427. https://doi.org/10.1175/JCLI-D-15-0508.1

Pan L-L (2007) Synoptic eddy feedback and air–sea interaction in the North Atlantic region. Clim Dyn 29:647–659. https://doi.org/10.1007/s00382-007-0256-7

Park J-Y, Kug J-S (2014) Marine biological feedback associated with Indian Ocean Dipole in a coupled ocean/biogeochemical model. Clim Dyn 42:329–343. https://doi.org/10.1007/s00382-012-1640-5

Peng S, Robinson WA, Li S (2003) Mechanisms for the NAO Responses to the North Atlantic SST Tripole. J Clim 16:1987–2004. https://doi.org/10.1175/1520-0442(2003)016<1987:MFTNRT>2.0.CO;2

Sun H, Wu R, Wang Z (2022) Dependence of spring Eurasian surface air temperature anomalies on the amplitude and polarity of the North Atlantic tripole SST anomalies. Theor Appl Climatol 150:103–119. https://doi.org/10.1007/s00704-022-04149-7

Yao S-L, Zhou W, Jin F-F, Zheng F (2021) North Atlantic as a trigger for Pacific-wide decadal climate change. Geophys Res Lett 48:e2021GL094719. https://doi.org/10.1029/2021GL094719

Zhang Y, Du Y (2021) Extreme IOD induced tropical Indian Ocean warming in 2020. Geosci Lett 8:37. https://doi.org/10.1186/s40562-021-00207-6

Zhou X, Jiang D, Lang X (2020) Unstable relationship between the Pacific Decadal Oscillation and eastern China summer precipitation: Insights from the Medieval Climate Anomaly and Little Ice Age. The Holocene 30:799–809. https://doi.org/10.1177/0959683620902215

KRISHNA BORHARA
krishna.borhara@usu.edu
Utah State University • Department of Plants, Soils, and Climate
4820 Old Main Hill • Logan, UT 84322-4820

EDUCATION

BACHELOR OF ARTS IN GEOLOGY AND MATHEMATICS	OHIO WESLEYAN UNIVERSITY August 2009 – May 2013
MASTER OF SCIENCE IN GEOLOGY	BOWLING GREEN STATE UNIVERSITY August 2013 – May 2015
DOCTOR OF PHILPSOPHY IN GEOLOGY	UTAH STATE UNIVERSITY August 2016 – May 2019 Status: transferred
DOCTOR OF PHILPSOPHY IN CLIMATE SCIENCE	UTAH STATE UNIVERSITY July 2019 – May 2024

RESEARCH EXPERIENCE/SKILLS

Rock Thin Section Technician at Ohio Wesleyan University (August 2012 – May 2013)
- Student Assistantship Position (StAP)
- Make thin sections for research and teaching collection of the Geology department
- Assist students in making thin sections for their research
- Maintain laboratory equipment

Geology research assistant at Bowling Green State University (August 2015 – May 2016)
Cathodoluminescence Microscopy
Scanning Electron Microscopy (Electron Backscatter Diffraction, Energy Dispersive X-ray Spectroscopy) Transmission Electron Microscopy
Synchrotron radiation data acquisition and analyses
- Micro X-ray Fluorescence (μXRF) mapping
- X-ray Near Edge Structure (XANES) spectroscopy

Stable isotope sample preparation and data analyses (Carbon, Hydrogen, Oxygen)
Total-organic-carbon (TOC) sample preparation and data analyses
Microsoft Office
ArcGIS Geospatial Analysis
Environment for Visualizing Images (ENVI) in Remote Sensing

TEACHING EXPERIENCE

As Instructor at Utah State University
- Spring 2020 (PSC4810/6810: Climate and Climate Change):
  - *ONLINE; Undergraduate and Graduate sections; 67 students*

Summer 2020 (PSC4810/6810: Climate and Climate Change):
ONLINE; Undergraduate and Graduate sections; 20 students
Fall 2020 (PSC2000: The Atmosphere and Weather):
WEB BROADCAST; Undergraduate and Graduate sections; 64 students
Spring 2021 (PSC2000: The Atmosphere and Weather):
WEB BROADCAST; Undergraduate course; 29 students
Fall 2021 (PSC2000: The Atmosphere and Weather):
BLENDED FACE TO FACE; Undergraduate course; 28 students

As Teaching Assistant at Utah State University
Fall 2019 (PSC4810/6810: Climate and Climate Change):
ONLINE; Undergraduate and Graduate sections; 39 students
Spring 2020 (PSC3250: Aviation Weather):
FACE TO FACE; Undergraduate course; 59 students
Fall 2021 (PSC6123: Climate Data Analysis):
HYBRID FACE TO FACE; Graduate course; 8 students
Fall 2021 (PSC6125: Climate Modeling and Simulations):
FACE TO FACE; Graduate course; 5 students

As Teaching Assistant at Bowling Green State University (August 2013 – May 2015)
GEOL 1050: Life through time
GEOL 2150: Geologic History of Dinosaurs
GEOL 3020: Mineralogy

TEACHING INNOVATIONS
PSC2000: (1) Weather and Climate Data Downloads
(2) Use of Microsoft Excel in Assignments (to process weather and climate data, draw graphs, and visualize concepts covered in lecture)
(3) Applications of Skew T plots (to study how atmospheric conditions can be used to analyze thunderstorms characteristics)
(4) Weather Forecasting Exercises (to learn what weather forecasting involves and assess how forecast accuracy decrease with time)
(5) Weather Maps (to plot weather systems and obtain 3-D view of atmospheric features or processes)
(6) Group Report, Presentations, and Evaluations (to learn how to write a report, develop presentations skills, and work effectively in group settings)
(7) Textbook production (in progress)

OTHER
Utah Public Radio (UPR) Weather Forecaster (2020 – 2022)

AWARDS AND GRANTS
ROBERT E. SHANKLIN Distinguished Scholar Award in Geology (April 2013)

RICHARD D. HOARE Research Scholarship Award (April 2014)
Geological Society of America Research Grants (April 2014 and April 2017)
SIGMA GAMMA EPSILON (April 2013)
National Honor Society in the Earth Sciences, Chapter DELTA LAMBDA
Outstanding BGSU Geology Graduate Student Award (April 2015)
American Association of Petroleum Geologists Foundation Grants-in-Aid (March 2017)
IKE J. CRUMBLY Minorities in Energy Grant
USU Center for Women and Gender (Fall 2016 and Fall 2017)
Theodore Daniel Scholarship
Southern California Earthquake Center (SCEC) Grant (2017)
KIM R. ROBESON Memorial Award (April 2017)
The GDL Foundation (Structural Diagenesis) award (October 2017)
USU Graduate Student Travel Awards (Fall 2017 and Fall 2018)
USU Plant, Soils and Climate Graduate Student Teaching Award (Fall 2021)
USU Outstanding Graduate Student Teacher for the College of Agriculture and Applied Sciences (Fall 2021)
USU Ambassador Ardeshir Zahedi International Endowment Scholarship (Fall 2022)

PUBLICATIONS

Borhara, K., S.-Y. Wang, Deng. L., 2024: The 2–3 Year Propagation of SST Anomalies from the Western North Pacific and Its Impact on ENSO Predictions (*in review*).

Borhara, K., B. Fosu, and S.-Y. Wang, 2023: The role of the western North Pacific (WNP) as an El Niño–Southern Oscillation (ENSO) precursor in a warmer future climate. *Climate Dyn.*, https://doi.org/10.1007/s00382-023-06773-z

Borhara, K., Pokharel, B., Bean, B., Deng, L., Wang, S.-Y. S., 2020. On Tanzania's Precipitation Climatology, Variability, and Future Projection. *Climate 8*, 34. https://doi.org/10.3390/cli8020034

Borhara, K., and Onasch, C.M., 2020. Evidence for silica gel and its role in faulting in the Tuscarora Sandstone: Journal of Structural Geology 139, 104140. https://doi.org/10.1016/j.jsg.2020.104140

Pokharel, Binod, Kripa Akila Jagannathan, S.-Y. Simon Wang, Andrew Jones, Matthew D. LaPlante, Smitha Buddhavarapu, Krishna Borhara et al; 2024. " Can We Rely on Drought-ending "miracles" in the Colorado River Basin?." *JAWRA Journal of the American Water Resources Association* 00 (0): 1–12. https://doi.org/10.1111/1752-1688.13204

Binod Pokharel, Kripa Akila Jagannathan, Shih-Yu (Simon) Wang, et al. 2022: Drought-busting 'miracles' in the Colorado River Basin may become less frequent and less powerful under climate warming. ESS Open Archive, https://doi.org/10.1002/essoar.10511012.1

Xu, C., Zhao, Q., An, W., Wang, S.-Y.S., Tan, N., Sano, M., Nakatsuka, T., Borhara, K., Guo, Z. 2021. Tree-ring oxygen isotope across monsoon Asia: Common signal and local influence. Quaternary Science Reviews 269, 107156, ISSN 0277-3791, https://doi.org/10.1016/j.quascirev.2021.107156

Xu, C., Wang, SY.S., Borhara, K. et al (2023): Asian-Australian summer monsoons linkage to ENSO strengthened by global warming. *npj Clim Atmos Sci*., **6**, 8, https://doi.org/10.1038/s41612-023-00341-2

Huang, S.-H.; Lai, P.-Y.; Hwang, S.-Y.; Borhara, K.; Huang, W.-R.; Wang, S.-Y. Climate Variability Shifting Immigrated Rice Planthoppers in Taiwan. Climate 2022, 10, 71. https://doi.org/10.3390/cli10050071